8-2019

A transport study of high density helicon plasma discharges in the Prototype Material Plasma Exposure eXperiment

Nischal Kafle
University of Tennessee, nkafle@vols.utk.edu

A transport study of high density helicon plasma discharges in the Prototype Material Plasma Exposure eXperiment

A Dissertation Presented for the

Doctor of Philosophy

Degree

The University of Tennessee, Knoxville

Nischal Kafle

August 2019

To my wife, parents, and grandmothers

...

Always grateful for your
selfless affection and dedication

Acknowledgments

First of all, I would like to sincerely thank my advisors, Dr. David Donovan, and Dr. Ted Biewer for spending a countless number of hours advising me and helping me learn and grow over the years. I will be in debt to you both for providing valuable lessons to advance in my career.

I owe great thanks to Dr. Juan Caneses as a mentor and a colleague. I will always remember working together for many numbers of hours developing probes and diagnostics, and running and planning experiments. I cannot forget the times we spent discussing using duck-tapes to fix all our problems and hangout at pubs to detox ourselves. I would also like to thank my committee members Dr. Maik Lang and Dr. Zhili Zhang for spending their valuable time on my dissertation. Also, I would like to extend my gratitude to Dr. Larry Owen for working on experimental measurements and plasma modeling. It was a fruitful collaborative effort joining the experimental and computational elements for Proto-MPEX.

Thanks to other staff scientists Dr. John Caughman, Dr. Rick Goulding, Dr. Tim Bigelow, Dr. Elijah Martin, Dr. Cornwall Lau, and Dr. Juergen Rapp for helping me learn about vacuum systems, plasma physics and sharing their experiences. I would also like to thank my fellow graduate students, Josh Beers, Holly Ray, Dr. Pawel Piotrowicz, and Dr. Missy Showers for helping me on various experimental works and discussing ad hoc solutions for real time problems. I am grateful to have to you all as my colleagues and making this journey enjoyable.

I would also like extend my gratitude to the entire Proto-MPEX team, especially, Mark Watson, Jeff Bryan, Ian Campbell, Andy Fadnek, Mike Harper, Jason McDaniel and Mike Morrow for helping me from cutting pipes, working with electrical connections, running tons of electrical wires, figuring out logistics, and on getting the machine ready early in the morning, working late hours and even during the weekends. Furthermore, I would like to thank the Department of Energy for supporting this project.

I want to sincerely thank family, especially, my parents, Neeta and Navaraj Kafle for their love and support. Finally, I am genuinely grateful to the love of my life, Shikha, for her immense love and support. I know she have been continuously cheering and pushing me towards achieving this goal. Thank you for being by my side throughout this beautiful journey.

Abstract

The Prototype Material Plasma Exposure eXperiment (Proto-MPEX) at Oak Ridge National Laboratory is instrumental in demonstrating the plasma source capability for the steady-state MPEX facility to study plasma-material interactions (PMIs). Proto-MPEX has justified MPEX by examining the efficiency of the helicon source, and auxiliary electron Bernstein wave (EBW) heating and ion cyclotron heating (ICH). This thesis aims to address the particle transport from the source toward the target in Proto-MPEX. The governing transport phenomenon in Proto-MPEX is identified using the electron temperature and density, Mach number, and other derived quantities. Extensive diagnostics coverage along the axial length of the device provided various plasma parameters. The upgraded Thomson scattering system and Mach-Double Langmuir probe were used for the study.

A small variation in the axial temperature for both helicon-only and helicon with an auxiliary heating system indicates that Proto-MPEX operates in the sheath-limited regime. The presence of strong parallel convective heat along the axis, except near the source, was experimentally measured and predicted using a data-constrained B2.5 Eirene model. With EBW, the conductive heat flux increased around the launcher but was not found to be significant in comparison. With a small temperature gradient and highly conductive flux, Proto-MPEX plasma transport is suggested to be sheath-limited. Increasing collisionality and density at the target can induce conduction-limited regime in Proto-MPEX. During the efficiency study of the transport with EBW heating, a flat or downhill magnetic field from the heating location to the target was found to be preferential to deposit higher heat flux on to the target.

The presence of various plasma sources creates a complex magnetic field geometry in Proto-MPEX. Such field variations create magnetic mirrors, which manifests Gas-dynamic trap for low energy and adiabatic-kinetic trapping for high energy plasmas. Experimentally, a linear increase in trapped density was observed with the mirror ratio for the low temperature population. Temporal profiles from flow measurement with ICH show plasma slow-down and the possibility of flow reversal upstream of the ICH resonance location. Discussions on some of the implication for the MPEX user facility is also presented.

Table of Contents

1 Introduction **1**
- 1.1 Fusion plasma devices . . . 2
- 1.2 Material challenges for fusion reactors for ITER and the role of MPEX . . . 3
- 1.3 Organization of the dissertation . . . 6

2 Prototype Material Plasma Exposure eXperiment (Proto-MPEX) **8**
- 2.1 Introduction . . . 8
- 2.2 Transport in Proto-MPEX analogous to a toroidal device . . . 9
- 2.3 Description of Proto-MPEX device . . . 10
  - 2.3.1 Configuration A . . . 11
  - 2.3.2 Configuration B . . . 14
- 2.4 Power source in Proto-MPEX . . . 20
  - 2.4.1 Helicon plasma source . . . 20
  - 2.4.2 Auxiliary wave heating . . . 21
- 2.5 Dissertation goals . . . 25

3 Probe diagnostics in Proto-MPEX **26**
- 3.1 Single Langmuir probe . . . 27
  - 3.1.1 Plasma sheath . . . 27
  - 3.1.2 I-V characteristic simulation . . . 28
  - 3.1.3 Error quantification . . . 31
  - 3.1.4 Results and discussion . . . 32
- 3.2 Double Langmuir probe (DLP) . . . 36
  - 3.2.1 Electron temperature and density calculation . . . 39
- 3.3 Mach probe . . . 39
- 3.4 Summary . . . 42

4 Thomson Scattering in Proto-MPEX **43**
- 4.1 Introduction . . . 43
- 4.2 Thomson scattering diagnostics hardware . . . 44
  - 4.2.1 Second laser pass implementation . . . 46
- 4.3 Results from double-pass TS in deuterium plasma . . . 51

4.4 Near target measurements using Thomson scattering . . . 53
4.5 Summary . . . 55

5 Helicon plasma transport in Proto-MPEX and comparison with B2.5-Eirene modeling 57
5.1 Introduction . . . 57
5.2 B2.5-Eirene . . . 58
5.3 Experimental measurements . . . 59
5.4 Axial comparison between experiment and B2.5-Eirene modelling . . . 60
5.5 Summary . . . 63

6 Experimental investigation of plasma transport with auxiliary heating 67
6.1 Transport model as divertor SOL in Proto-MPEX . . . 68
6.1.1 Simple SOL heuristic model . . . 68
6.1.2 Cross-field diffusion . . . 72
6.2 Compressible nature of plasma . . . 74
6.3 Parallel heat transport . . . 76
6.4 Heat transport on Configuration A . . . 79
6.5 Axial plasma transport on Configuration B . . . 82
6.5.1 Axial plasma behavior on helicon and auxiliary heating . . . 82
6.5.2 Heat transport in Configuration B . . . 87
6.5.3 EBW flow measurement in overhill and downhill magnetic geometry . . . 90
6.6 Summary . . . 93

7 Experimental investigation of the effects of magnetic mirrors on plasma transport in Proto-MPEX 94
7.1 Introduction . . . 94
7.2 Background on magnetic mirrors trap . . . 95
7.3 Two plasma populations in Proto-MPEX . . . 96
7.4 Effect of collisions and transport regimes . . . 99
7.4.1 Plasma leak rate from a mirror trap in the Gas-dynamic regime . . . 100
7.5 Mirror effects on low temperature helicon plasma . . . 102
7.5.1 Experimental observation of Gas-dynamic transport . . . 103
7.5.2 Gas-dynamic model . . . 105
7.6 Magnetic mirror effect during ion cyclotron heating . . . 107
7.6.1 Influence of mirrors on the power deposition on the target with EBW . . . 110
7.7 Summary . . . 112

8 Conclusion and Future Work 113
8.1 Conclusion . . . 113
8.1.1 Mach-double Langmuir probe and Thomson scattering installation . . . 113
8.1.2 Convective heat transport dominant in Proto-MPEX . . . 114

8.1.3 Helicon with EBW auxiliary heating . . . 115
8.1.4 Magnetic mirrors choke the plasma in Proto-MPEX . . . 116
8.2 Implications for MPEX plasma transport . . . 116

Bibliography **118**

Appendices **127**

A Thomson Scattering calibrations **128**
A Spectrometer pixel number to wavelength calibration . . . 128
B Density calculation . . . 128

B Error Propagation **131**

C Additional probe information **132**
A Alternative method to calculate electron temperature from the IV characteristics from DLP . . . 132
B Mach Probe circuit diagram . . . 133

D Additional plots **135**
A Flow measurement with ICH . . . 135
B Double Langmuir probe radial profiles . . . 136
B.1 Downhill magnetic field . . . 136
B.2 Overhill magnetic field . . . 139

Vita **142**

List of Tables

2.1 Performance goals of MPEX 9
2.2 Coil current [kA] values used for generating B field as shown in Figure 2.2 14
2.3 Coil current [kA] values to generate B field favorable for EBW resonance heating 16

3.1 The error in kT_e in percent for typically observed values of ϕ_{RF} associated with a plasma having $kT_e = 5\ eV$ and $n_e = 1e17\ m^{-3}$. 32

6.1 Classical perpendicular cross-field diffusion in Configuration B in overhill and downhill magnetic fields. 73
6.2 Bohm perpendicular cross-field diffusion in Configuration B in overhill and downhill magnetic field. 73

List of Figures

1.1 Fusion reaction cross-sections 2
1.2 Cross sectional schematic of ITER fusion reactor, obtained from ITER.org. 4
1.3 2D poloidal cross-section of NSTX. 5

2.1 The plasma geometry from a 'straightened out SOL' in a divertor tokamak is similar to a linear plasma device. Two divertor plates are the target materials similar to those in linear plasma devices. The 'u' in the figure represents the upstream plasma parameters such as upstream T_{e_u}, n_{e_u}. 10
2.2 The figure shows a cross-sectional schematic of Proto-MPEX where the helicon antenna along with auxiliary heating sources, and critical diagnostics locations are located. The approximate length of the device from the dump end to the target end is about 3.6 m. The red contour represents the plasma diameter along the device. 11
2.3 a) The top figure shows the axial magnetic field strength along the device, and (b) shows the location of fueling puffers (G1-G3), baratrons (P1-P4), skimmers, quartz sleeve, helicon antenna, ICH(4-9 MHz) and 28 GHz launch location, target and dump plates. For fueling, G1 gas value is a mass flow controller, and G2 and G3 are piezo gas value. 12
2.4 **(a)** The magnets on time in Proto-MPEX is typically 6 s. The neutral gas puff signal using a piezo gas value is triggered $\sim$ 200 ms prior to the RF plasma. **(b)** Net power delivered from helicon rf source (black), ICH power (red) and 28GHz power (blue). About 90 kW of power is delivered from the helicon, and about 30 kW of power is delivered from ICH and 28 GHz. 13
2.5 The figure shows a cross-sectional schematic of Proto-MPEX showing unmodified helicon region represented in black and white, and modified region downstream from the 'central chamber' represented in yellow. A new ECH/EBW heating system installed between coils 8 and 9, and an external ICH antenna between coils 9 and 10. 15
2.6 **(a)** The figure shows the axial magnetic field strength. **(b)** shows the axial plasma profile and the location of fueling puffers (G1-G3), baratrons (P1-P4), skimmers, helicon antenna, ICH (6.5 MHz) and ECH (105 GHz), and EBW (28 GHz) launch location, target and dump plates for upgraded Proto-MPEX. 17

2.7 Modified target spool piece with additional 12 ports and labels for some allocated diagnostics . . . 18
2.8 Overhill and downhill magnetic field condition used during EBW experimental campaign in configuration B. The magnetic field at the helicon source remain unaffected. . . . 19
2.9 Location of resonance zone at specific magnetic field and radius, r. . . . 21
2.10 The dispersion relation for electromagnetic waves propagating parallel and perpendicular to the magnetic field in a cold plasma . . . 22
2.11 Schematic of O-X-B mode conversion for EBW heating in Proto-MPEX . . . 24
2.12 Infra-red camera image of the heat flux deposited int the target plate in Proto-MPEX. (**Left**) The heat flux on the target from helicon only discharge, and (**Right**) heat flux on the target with the addition of 28 GHz launch. . . . 25

3.1 Representation of plasma potential forming sheath near walls . . . 28
3.2 I-V characteristics of a typical single tip cylindrical Langmuir probe. . . . 30
3.3 I-V characteristics for ϕ_{RF} = 0 V (solid black), ϕ_{RF} = 10 V (dashed yellow), and the instantaneous I-V characteristics (red) fluctuating between ±10 V. . . . 31
3.4 Simulated and fitted I-V characteristics associated with a plasma having $kT_e = 5\ eV$ and $n_e = 1e17\ m^{-3}$ experiencing a sinusoidal RF plasma potential of (a) 5 V, (b) 10 V, and (c) 15 V. . . . 33
3.5 The error in kT_e as a function of kT_e for $\phi_{RF} = 15\ V$. These results are applicable to plasmas having an n_e in the range of (a) $1e17$ to (b) $1e19\ m^{-3}$. . . . 34
3.6 kT_e as a function of ϕ_{RF} for three different electron densities ($1e17\ m^{-3}$, $1e18\ m^{-3}$, $1e19\ m^{-3}$) plotted at (a) $\sigma_{kTe} = 10\%$, and (b) $\sigma_{kTe} = 50\%$, and fitted with a linear regression line. . . . 35
3.7 The error in kT_e as a function of kT_e for $\phi_{RF} = 15\ V$. These results are applicable to plasmas having an n_e in the range of $1e17$ to $1e19\ m^{-3}$. . . . 35
3.8 Temporal profile of (*left*) electron density and (*right*) electron temperature during a plasma discharge 300ms. . . . 37
3.9 IV characteristics from a symmetric DLP where i_0 is the maximum current collected by probe tip during the voltage sweep. . . . 37
3.10 Figure (a) shows a typical double probe head where the tip length is around 1 to 2 mm, (b) shows the custom pieces made to create proper ground connection, and (c) shows the linearly translation probe drive. . . . 38
3.11 Image of Mach/double Langmuir probes (M/DLP probe). Double tip with tip length of 2 mm and one side of a Mach probe tip length of 4 mm is seen. Both DLP and Mach probes tungsten wires had a diameter of 0.254 mm. . . . 40

3.12 The raw signal measured by the Mach probe tips is presented in the figure where (a) shows the signal collected for a plasma discharge, and (b) shows the magnified signal during the same discharge. The probe was gated at 5 to 10% to protect from tips from overheating and damaging. The plot in black shows current collected by the upstream facing tip, and the plot in red shows the current collected by the downstream facing tip. 41

4.1 Setup of an incoherent Thomson scattering experimental configuration in Proto-MPEX. The dark core represents highly ionized deuterium plasma typically observed in Proto-MPEX. The arrangement of the optical fiber bundle with respect to the plasma column is presented. The localized volume where the light scattering after the interaction with a free electron measured from the TS diagnostics system is represented by the white dots. 45
4.2 Quanta-Ray Pro 350 laser system used for Thomson Scattering in Proto-MPEX. Two oscillators are shown on the top of the image and amplifiers on the bottom (left) along with frequency doubling crystal (bottom right). 45
4.3 The figure shows the laser route through the Proto-MPEX vacuum chamber. The laser route existing near the target chamber, and the recently installed laser route from the 'central chamber' is shown. The red surface depicts the axial variation in the plasma diameter due to the changing magnetic field. The photographs at the bottom show the air breakdown occurring at the focal point at the geometric center of the (vented) vacuum chamber. 47
4.4 An optical schematic of the Thomson scattering diagnostic system from the diagnostics laboratory to Proto-MPEX (not to scale). In the figure, **BET**: beam expanding telescope, $\mathbf{M}_1$-$\mathbf{M}_6$: mirrors, **CO**: collection optics, $\mathbf{A}_1$-$\mathbf{A}_5$: aperture, and **BW**: Brewster window. 48
4.5 The conflat vacuum flange covered with Acktar Spectral Black (left), and the microwave reflecting surface anodized with black coating (right) to minimize light reflection. 51
4.6 A fit to the Thomson scattering data from a fiber at the target region is shown. In a) blue dots are the scattered photon counts, open circles are the excluded data around the 532 nm, and the red line is the Gaussian fit to the data. In b) black dots are the residual from fitted data, open circles are the excluded data, and the red line is the zero reference line. 52
4.7 TS Radial profiles of the electron temperature and density measured in (a) the central chamber, and (b) in the target region. 53
4.8 (a) An axially translating target system with respect to the target spool-piece. As shown a stainless steel target is attached to the bellows of the translating system. A thermocouple is attached to the back of the target surface. Bolts seen on the front side of the target surface was used to hold a target heater. (b) Front view of the target plate. 54

4.9 Figure shows T_e and n_e as a function of target position relative to the TS laser. z = 0 cm is the position of the TS laser, and the negative scale represents distance further way from the center of the TS laser position. A scan of the target position is taken 1 to 4 cm away from the target. 55

5.1 Contour plot of the assumed electron heating distribution [W/m^3] from the helicon wave. 59
5.2 A cross-sectional schematic of Proto-MPEX in Configuration A, showing the helicon antenna along with auxiliary heating sources, and critical diagnostics locations 60
5.3 The figure presents radial T_e (left) and n_e (right) profiles from the central chamber to near target measured using DLPs (Probes B-D) and Thomson scattering. The radial T_e profile is relatively flat at different axial locations, except at Probe B where T_e at the edge peaks to 10-12 eV. Probe B measured radial profile at the central chamber, and Probes C and D took the radial measurement 60 cm and 90 cm downstream from the central chamber, respectively. The Thomson scattering measured T_e and n_e ∼10 cm in front of the target plate. 61
5.4 Axial plasma pressure (p_e) profile along Proto-MPEX. Comparison between measured (red dots) and modeled plasma pressure (solid curve) from B2.5 Eirene is shown. Higher pressure is observed near the source than near the target. 61
5.5 (left) shows the axial T_e profiles and (right) shows the axial n_e profiles from experiment (red dots) and B2.5-Eirene model (solid curve). Plasma at the source has higher T_e which decreases downstream from the source 62
5.6 Axial Mach number along Proto-MPEX. Mach number compared between the experiment (red dots) and modeling (solid curves). Stagnation region observed near the source and increased Mach number near the targets at both ends. 64
5.7 Probe shadowing in the visible light emission observed by the fast-visible camera at M/D probe C location. 64
5.8 Radial Mach number at z = 0.45 m from Mach probe, M/D Probe A (red dots) is compared to B2.5-Eirene model (solid curves). From modeling, radial flow profile at z = 0.36 m (closer to the dump plate) is in better agreement with the experimental data. 65

6.1 Different regions of Proto-MPEX illustrated in relation to a divertor SOL. 69
6.2 Axial magnetic field profiles in Proto-MPEX in Configuration A. The variation in the field obtained from the B-field scan conducted for the compressible flow study. 75
6.3 Plasma (a) electron density (b) electron temperature, and Mach number as a function of B at the measurement location. 77
6.4 Ratio of I to nv as a function PS1 current taken downstream of the central chamber (at z = 2.7 in Figure 6.2) is plotted and normalized to the peak value. PS1 is used as a proxy to the change in magnetic field. 78

6.5 Axial heat fluxes from conductive and convective transport in Proto-MPEX Configuration A . . . 80
6.6 Thomson scattering radial Profile of n_e, T_e, and P_e with (red) and without (black) 28 GHz measured in (left) the central chamber, and (right) in the target region. The 28 GHz wave is launched at the central chamber, and blue line represents the cut off of the electron cyclotron wave propagation. . . . 81
6.7 Axial division of Proto-MPEX into different transport regions in Configuration B 82
6.8 Axial plasma parameters showing (a) axial electron temperature, (b) density, (c) static plasma pressure, and (d) Mach number for **helicon-only** discharges. The red and the back profiles represent two magnetic configuration applied downstream of the auxiliary heating section for electron heating. . . . 83
6.9 Axial plasma parameters showing (from top to bottom) axial electron temperature, density, static pressure, and Mach number for helicon (black) and with 28 GHz (red) discharges for the (a) Overhill condition and (b) Downhill condition. . . 85
6.10 Axial plasma parameters showing (a) axial electron temperature, (b) density, (c) static pressure, and (d) Mach number for overhill (red) and downhill (black) field conditions when **28 GHz EBW is applied** to the helicon plasma. . . . 86
6.11 On-axis $q_{d\|}$ transport for helicon-only and helicon with 28 GHz discharges for overhill and downhill magnetic field conditions is shown. The data points in the plot shows $q_{d\|}$ between the source and the central chamber, between the central chamber and the heating region, and between the heating and the target region. . 88
6.12 On-axis $q_{v\|}$ transport for helicon-only and helicon with 28 GHz discharges for overhill and downhill magnetic field conditions is shown. . . . 89
6.13 Downhill field normalized to the overhill field to investigate the transport efficiency between the two magnetic field geometries. . . . 91
6.14 On-axis axial (a) Mach number and (b) velocity profile is shown for the **downhill** condition. . . . 92
6.15 On-axis axial (a) Mach number and (b) velocity profile is shown for the **overhill** condition. . . . 92

7.1 Plot shows 90 degree scattering (left) collision frequency ($\nu_\perp$) and (right) mean free path ($\lambda_\perp$). Electron-electron (black) and electron-ion (red) interactions as a function of **electron energy** are plotted. . . . 97
7.2 Plot depicts 90 degree scattering (left) collision frequency ($\nu_\perp$) and (right) mean free path ($\lambda_\perp$). Here, ion-electron (black), and ion-ion (red) interactions as a function of **ion energy**. are plotted. . . . 98
7.3 90-degree scattering mean free path for particles “a" on background species “b" as a function of particle kinetic energy. Green area represents the range of mirror-to-mirror lengths in Proto-MPEX . . . 101
7.4 The axial magnetic field indicating the location where the B scan was occurring. Double Langmuir probes (DLPs) 1 and 2 measured n_e near the source and the target. 103

7.5 n_e as a function of mirror ratio (R) measured near the source location (red), and near the target region (blue). . . . 104
7.6 Neutral gas pressure (P_{D_2}) measured as a function of mirror ratio R near the target location. . . . 104
7.7 Neutral gas profile at the source location stays relatively the same during the mirror ratio scan. A subset of the number of shots is chosen here for representation. 106
7.8 Comparison between n_e at the source region obtained experimentally (black) and using the collisional confinement model (red) is shown as a function of the mirror ratio (R). . . . 107
7.9 ICH resonance region in Proto-MPEX for the ICH frequency of 6.5 MHz. The dashed line indicates the resonant B of 0.9 T for 6.5 MHz RF injection. . . . 108
7.10 Figure (a) shows the temporal current collected by the two Mach probe tips (upstream (black) and downstream (red)) before, after and during ICH power injection. Figure (b) shows the Mach number as a function of the ICH power. . . . 109
7.11 Flow measurement taken at the central chamber shows Mach Number, M, as a function of the mirror ratio, R during ICH (red), and during helicon (black). . . . 110
7.12 The figure shows measurement conducted using IR thermography, where the plot (a) total heat/energy received at the target as a function of the B. Total energy is normalized to the cross-sectional area of the flux tube. (b) shows the peak heat flux at the target again as a function of B. Measured peak heat flux value is irrespective of the flux tube expansion or compression. Black circles in (a) and (b) are for the helicon only discharges, and red circles are with the addition of EBW. The bottom figure (c) shows the scan of the axial magnetic geometry where B between 28 GHz launcher and the target. The data points where the overhill and downhill field conditions lie is also identified. . . . 111

8.1 Magnetic field profile in MPEX for second harmonic EBW heating (black), and ECH (Whistler) heating (red). . . . 117

A.1 Spectral lines from the neon lamp. . . . 129

C.1 The Mach probe driver circuit built for Proto-MPEX to provide DC power to the Mach probe tips and measure the saturation current. Commercial off the self components were used in the circuit. . . . 134

D.1 On-axis axial (a) Mach number and (b) velocity profile is shown for helicon with ICH operation. . . . 135
D.2 p_e, n_e, and T_e at spool 1.5 . . . 136
D.3 p_e, n_e, and T_e at spool 8.5 . . . 137
D.4 p_e, n_e, and T_e at spool 12.5 . . . 138
D.5 p_e, n_e, and T_e at spool 1.5 . . . 139
D.6 p_e, n_e, and T_e at spool 8.5 . . . 140

D.7 p_e, n_e, and T_e at spool 12.5 141

Chapter 1

Introduction

The standard of living in today's world has a strong correlation to the consumption of power. Various studies have shown that the economic growth of a nation will have a significant impact on CO_2 emission [1, 2]. With the world's population increasing at a rapid pace and poverty rates falling across the world, the demand for energy should be expected to rise consistently. To meet our rising demand for electricity we depend primarily on three natural resources 1) fossil fuels, 2) nuclear, and 3) renewable (solar, wind, geothermal, hydro-power) [3]. The majority of the developed nations are heavily dependent on fossil fuels for their base-load energy. Since the science behind the rise in earth's temperature due to anthropogenic emissions from fossil fuels leading to climate change has been well established, the goal of obtaining carbon-free energy resources becomes paramount [4].

Achieving base-load energy from renewable sources alone is still in the distant future. Nuclear fission, which for the short-term, could be an alternative to coal and natural gas has fundamental concerns of long-lived radio-isotopes and criticality safety. In light of such concerns, nuclear fusion is the best candidate for clean, safe and continual energy that would solve the energy problem for generations to come. The ambition to harness energy from nuclear fusion has been in the works for over half a century. In recent years, advancements in materials and technology, from computing to additive manufacturing, have been instrumental on making substantial progress towards generating energy from fusion power. Now we are closer to generating sustainable nuclear fusion energy than ever before. Some inertial confinement fusion (ICF) and magnetic confinement fusion (MFE) devices such as tokamaks, stellarators, reversed field pinches (RFP), spheromaks, and field reverse configurations (FRC) and other variations are currently being pursued to make fusion energy feasible.

The first-generation fusion reactors are currently pursuing deuterium-tritium (D-T) fusion, as shown in Eq. (1.1).

$$ {}^{2}_{1}\mathrm{D} + {}^{3}_{1}\mathrm{T} \longrightarrow {}^{4}_{2}\mathrm{He}\,(3.54\mathrm{MeV}) + {}^{1}_{0}\mathrm{n} + (14.1\mathrm{MeV}) \tag{1.1} $$

The preference for D-T fusion is because of the higher cross-section of the D-T fusion reaction at a lower temperature in comparison to other fusion reactions such as deuterium-deuterium (D-D) or deuterium-helium-3 (D-He3), such as in Eq. (1.2).

$$ {}^{2}_{1}\mathrm{D} + {}^{3}_{2}\mathrm{He} \longrightarrow {}^{4}_{2}\mathrm{He}\ (3.66\mathrm{MeV}) + {}^{1}_{1}\mathrm{p} + (14.6\mathrm{MeV}) \tag{1.2} $$

The cross section as a function of energy for different fusion reactions is shown in Figure 1.1 (Retrieved from [5]). Moreover, deuterium is abundantly present as it occurs as 0.0153 % of natural hydrogen [6]. Although natural tritium is extremely rare on earth because of its short half-life of 12 years, tritium can be bred using ^{6}Li blankets. However, the drawbacks of the D-T reaction are the use of radioactive tritium as a fuel and production of 14.1 MeV neutrons as a by-product. Such energetic neutrons cause radiation damage and make the structural components weaker and radioactive due to neutron activation. It will necessitate the use of shields that will increase the cost of the reactor.

The ultimate goal of fusion energy research should be to provide clean energy from fusion reactions that do not produce neutrons (aneutronic reactions) with high energy yield.

1.1 Fusion plasma devices

In the 1950s, after the fruition of the thermonuclear weapons program, nuclear fusion in general was established as an energy science research program. The challenge since then has been to create and confine the hot and dense plasma long enough for "ignition" to be possible. Fusion ignition occurs when the plasma maintains self-heating, thereby reducing the need for external heating. The initial concept of linear magnetic mirror fusion devices was replaced by toroidal

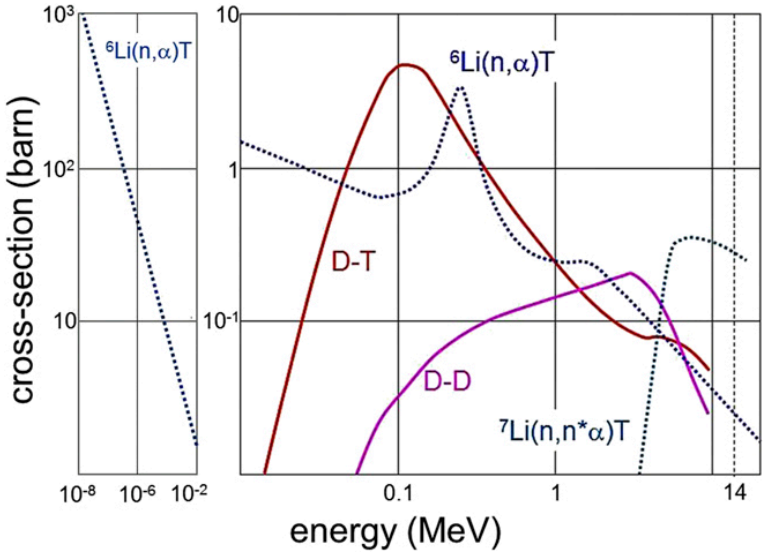

Figure 1.1: Fusion reaction cross-sections

confinement devices, which have issues with turbulence and instabilities. In the mid to late 1990s, significant advancements were made in fusion technology and control of the plasma so that D-T fusion at record high levels was achieved in two different tokamaks: 1) the Tokamak Fusion Test Reactor (TFTR) [7], and 2) the Joint European Torus (JET) [8]. Currently, there are several devices such as the DIII-D National Fusion Facility (DIII-D), the Experimental Advanced Superconducting Tokamak (EAST), and the Wendelstein 7-X (W7-X) stellarator that are operational around the world. The nuclear fusion community is working on exploring the next achievable goal of a burning fusion plasma with the International Thermonuclear Experimental Reactor (ITER) [9], as shown in Figure 1.2 (retrieved from Ref. [9]). ITER has been designed to achieve a Q >10. Q-value in fusion is a measure of the efficiency of a fusion reactor indicating the amount of fusion power produced relative to the amount of power injected to heat the plasma. According to ITER, the reactor is designed to: (1) Produce at least 500 MW fusion power output with 50 MW input (Q=10), (2) Integrate operation of technologies for future power plants, (3) Serve as test bed for tritium breeder blankets, and (4) Demonstrate controllable "burning" plasma fusion and its minimal impact to the environment.

The successful development of ITER together with the International Fusion Materials Irradiation Facility (IFMIF) [10] and the fusion power plant prototype DEMO [11] is essential for making a fusion power plant possible in the future. However, there is still a gap in understanding plasma behavior and techniques are needed to mitigate high heat fluxes during plasma disruptions. More importantly, high operating temperatures and large particle fluences experienced by the first wall materials in DEMO and future reactors are much greater than ITER will ever experience in its lifetime [12, 13]. Exposure to high ion fluxes ($> 10^{24} m^{-2} s^{-1}$) can lead to surface modification, re-deposition, and erosion [14].

1.2 Material challenges for fusion reactors for ITER and the role of MPEX

Operating temperature and radiation damage levels for newer generation fission reactors (such as VHTR, GFR, MSR) and fusion reactors are comparable with each other. For a typical Gen-II LWR, any structural material would suffer about one displacement per atom (dpa), but new fission and fusion reactor designs would realize ≥100 dpa. Three details need attention while designing radiation-resistant materials: (1) utilization of matrix phases with inherent radiation tolerance, (2) selecting materials with immobile vacancies, and (3) engineering materials with high sink densities for point defect recombination [15]. Materials research for fusion faces more significant challenges as materials need to operate at a higher temperature, radiation damage, and in an intense production of transmutant elements (H and He); thus making the fabrication of such materials more difficult [16]. Furthermore, in contrast with conventional LWRs where the use of stainless steel as reactor pressure vessel material is ubiquitous, SS-316 could not be used in high irradiation fusion reactor environments due to increased swelling, cavity formation and loss

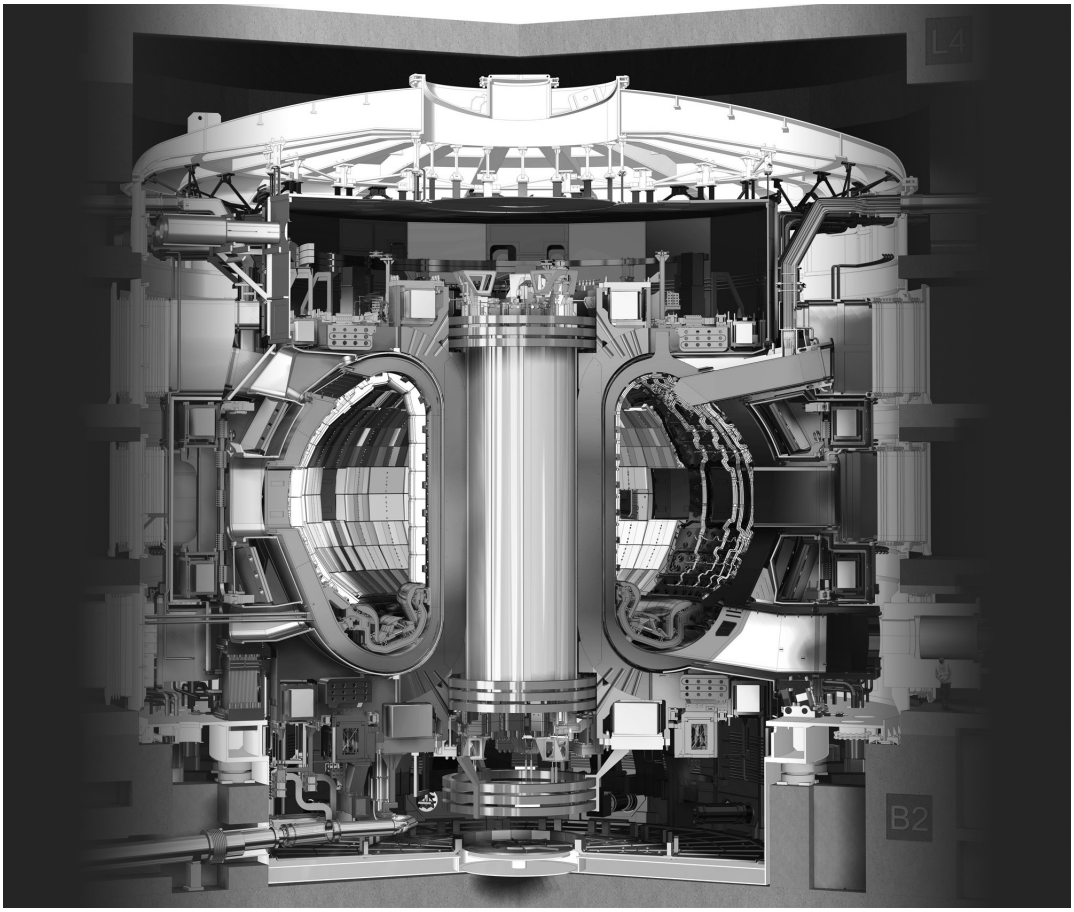

Figure 1.2: Cross sectional schematic of ITER fusion reactor, obtained from ITER.org.

of ductility. Metals such as Mo (BCC) (in stainless steel) are ductile at operating temperature but become brittle when cooled down to room temperature. A primary cause of increased swelling due to cavity formation is by the production of gases such as hydrogen and helium. Fission neutrons have peak energy of 1 MeV, whereas fusion neutrons have 14 MeV; these fast neutrons produce knock-on displacements in materials which create interstitials and vacancies. The cross-sections for (n,α) and (n, p) increase rapidly with increases in neutron energy. The cross-sections for proton and helium production in n-Fe interaction increase by two or three orders of magnitude for D-T fusion neutrons, when compared to fast fission neutrons [6].

For the reasons above, new materials must be capable of withstanding the harsh conditions of a fusion plasma environment, and research is needed to test and characterize their performance – thus making the study of fusion plasma material interactions (PMI) an integral part of fusion energy research [17]. Various PMI studies across the world are being conducted in linear plasma devices, which is a simple and relatively inexpensive alternative to larger toroidal devices [18]. Linear devices will enable research to understand plasma behavior, high heat flux mitigation, and design new materials for plasma-facing components (PFCs). Moreover, they are built to study unique features of PMI and can also simulate the edge plasma region of a tokamak where the open field lines end at the material surface. This edge plasma region in a toroidal device is called a "scrape-off layer" (SOL) and the material surface where the open field lines meet the wall is called a "divertor." Figure 1.3 (retrieved from [19]) shows a 2D poloidal cross-section of the National Spherical Tokamak Experiment (NSTX).

There are several linear plasma devices [20] that are operating in various regimes of parameter space with variations in the magnetic field (B), length (L), electron density (n_e), and electron and ion temperatures (T_e and T_i). Limitations, however, exist with the linear

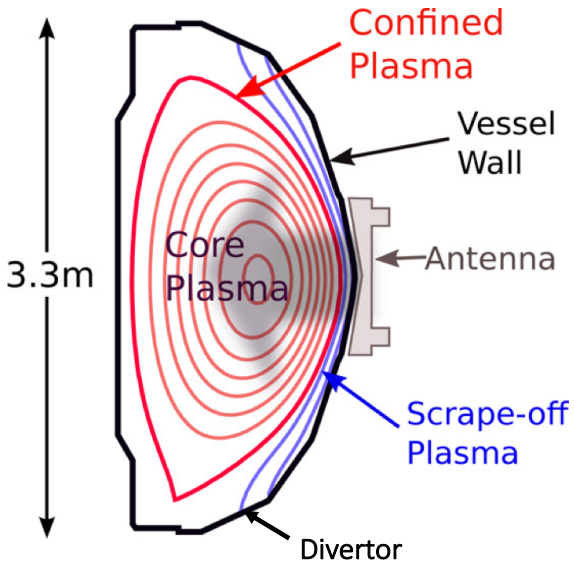

Figure 1.3: 2D poloidal cross-section of NSTX.

plasma devices as they represent a simplified divertor geometry. Besides, the size of the device limits the magnetic field connection length; hence, linear devices cannot simulate complex three-dimensional scenarios typically observed in toroidal devices. Linear devices are therefore considered as a necessary extension to simplify experiments and isolate effects of interest, primarily for PMI studies. One such device is currently at a conceptual stage at Oak Ridge National Laboratory (ORNL). A linear plasma device is being designed to be a linear divertor simulator called the Material Plasma Exposure eXperiment (MPEX). To develop the plasma source concept for MPEX a prototype test-bed, called the Prototype Material Plasma Exposure eXperiment (Proto-MPEX) [21] is currently operational at ORNL, which is used primarily to optimize helicon plasma source and its auxiliary plasma heating sources [22, 23, 24].

Proto-MPEX is different compared to other linear devices with respect to axial magnetic fields present along the device. Most linear devices have a uniform magnetic field from the source to the material target plates. The helicon plasma source needs low B_0 of ∼0.05 T and magnetic wells to operate for the available power of 100 kW; electron heating requires ∼0.5 T, and the target field should be ∼1 T as per the requirements of MPEX. Presence of such crests and troughs in the magnetic field creates magnetic mirrors, which cause a unique challenge in transporting plasma from the source to the material target. This thesis studies the transport phenomenon in Proto-MPEX in the presence of such magnetic ripples. Chapter 2 will discuss the operational goals for MPEX for material research and various aspects of Proto-MPEX.

1.3 Organization of the dissertation

The layout of the thesis can be broken down into three topic areas: description of the prototype linear plasma device at Oak Ridge National Laboratory, the development, and utilization of probes and laser-aided diagnostics for measuring the plasma properties, and plasma transport studies in the linear plasma device. The dissertation outline is as follows:

1. **Chapter 2** describes MPEX goals and components of Proto-MPEX, along with its helicon plasma source and ion and electron heating mechanisms with ion cyclotron heating (ICH) and electron cyclotron heating (ECH). The chapter will also provide the goals of the thesis.

2. **Chapters 3** and **4** focuses on the plasma diagnostics tools, and their measurement techniques and challenges. The primary probe-based plasma diagnostics needed for this work are Langmuir probes and Mach probes, which are discussed in chapter 3. The chapter also will identify the limitations of perturbative probe measurement techniques. Chapter 4 will discuss the implementation of Thomson scattering diagnostics in Proto-MPEX, measurements, and its limitations and challenges.

3. **Chapter 5** contains a discussion of the axial plasma transport on helicon-only discharges. The data-constrained B2.5-Eirene modeling is compared with the experiments results, which was an important benchmarking opportunity for the model in a linear plasma device.

The model was initially developed for the toroidal devices to study the plasma behavior in the SOL of toroidal devices.

4. **Chapter 6** presents the transport model of Proto-MPEX as compared to the scrape-off-layer transport in a toroidal device. This chapter also presents the operating conditions to identify the transport regime in Proto-MPEX. The chapter presents a discussion on the axial transport with auxiliary heating systems and the study of plasma flow behaviors and compares the underlying theoretical model with the experimental results.

5. **Chapter 7** focuses on the effects of magnetic mirrors during helicon plasma discharges with and without auxiliary heating. This chapter presents existing theoretical understanding of trapping for collisional plasma and non-collisional kinetic plasma and analyzes the experiments distinguishing each of the trapping mechanisms.

6. **Chapter 8** presents the summary of the thesis and possible future work that can be conducted to advance the transport research in this device and implications for MPEX.

Chapter 2

Prototype Material Plasma Exposure eXperiment (Proto-MPEX)

2.1 Introduction

Plasma facing components (PFCs) in fusion reactors will face harsh heat and particle fluxes that will cause surface erosion, re-deposition, and surface modification. Understanding the material morphology in fusion reactors is critical for the extended operation during power production. Material Plasma eXposure Experiment (MPEX) at Oak Ridge National Laboratory (ORNL) is envisioned to be a steady-state PMI device for PFCs exposed to high particle and heat fluxes. The goal of MPEX is to produce plasma conditions with high heat $\left(\geq 10\frac{\mathrm{MW}}{\mathrm{m}^2}\right)$ and particle $\left(\geq 10^{24}\frac{1}{\mathrm{m}^2-\mathrm{s}}\right)$ fluxes, which are observed during edge-localized mode (ELM) transients for rigorous testing of surface materials. The overall performance goals of MPEX are listed below in Table 2.1 [25].

At the initial stage, demonstration of a plasma source that is capable of producing such high heat and particles fluxes is critical before any material testing. Therefore, the focus of the prototype device, the Prototype Material Plasma Exposure eXperiment (Proto-MPEX) at ORNL, has been on developing the source concept for the MPEX device. One of the primary objectives has been to produce high electron and ion temperatures and densities near the target material. Continued effort on the source development and delivery of high heat and particle fluxes to the target is being performed. Moreover, along with the development process, some of the goals for MPEX have been achieved.

This chapter will provide some analogies between a linear plasma device and a toroidal device. This chapter will help to provide some context when describing the plasma conditions and experimental observations obtained from Proto-MPEX. Furthermore, the chapter will discuss

Table 2.1: Performance goals of MPEX

Parameters	Goals
n_e source	$6 \times 10^{19}\ m^{-3}$
n_e target	$10^{21}\ m^{-3}$
T_e source	25 eV
T_i source	25 eV
T_e target	15 eV
T_i target	up to 20 eV
$\Gamma_{\|\|}$ target	$\geq 10^{24}\ m^{-3}s^{-1}$
B target	1–2 T
Plasma diameter	3–10 cm
Target tilt	5°
$P_{\|\|}$	up to 40 MW/m^{-2}
$P_{\perp}$	10 MW/m^{-2}
Total ion fluence	up to $10^{31}\ m^{-2}$

various plasma source and heating components of Proto-MPEX. Lastly, the operating scenarios of Proto-MPEX that are optimized to produce the desired conditions are presented.

2.2 Transport in Proto-MPEX analogous to a toroidal device

As discussed by Stangeby in Ref. [26], the similarity between a tokamak and a linear divertor simulator arise when we consider the scrape-off layer of a tokamak plasma and straighten it out along the magnetic field lines, as shown in Figure 2.1 (retrieved from [26]). The parallel gradients are assumed to be small away from the target region, so the position of an upstream point ('u') could be subjective. Parallels between this 'linear' picture of a divertor SOL and Proto-MPEX can be drawn by dividing Proto-MPEX into three regions along the axis, as shown in Figure 2.1. The three similarities are: (1) the upstream 'u' is the source region, (2) the region between the source and the target is like transport in the main SOL, and (3) the region near the target plate is similar to transport in the divertor SOL.

However, plasma parameters in the upstream region in a tokamak is an order of magnitude higher than in a linear device. Thus, making it easier to distinguish the gradient between the upstream and downstream conditions in a tokamak. A challenge with the linear device will be to correctly interpret a much smaller parallel gradient in plasma parameters and identify various regimes that could be present near the target such as the detached regime [27, 28, 29], sheath-limited regime, convection dominated regime, or conduction limited regime [26].

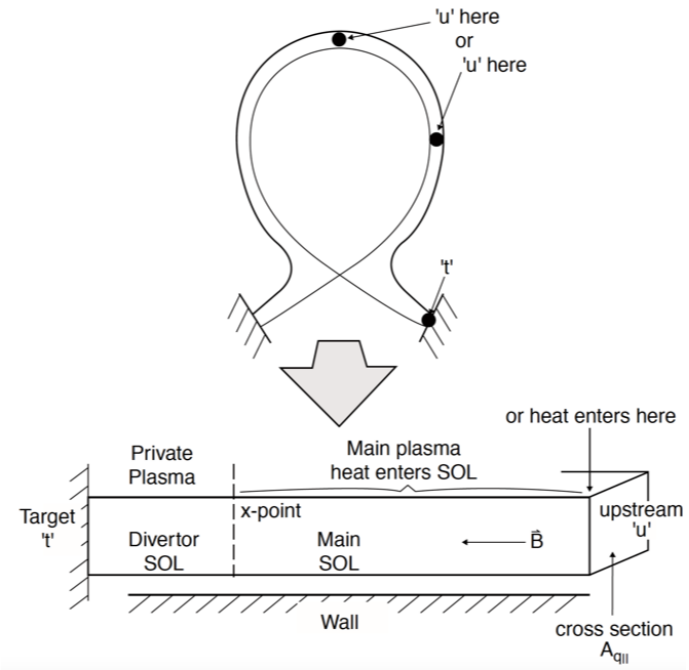

Figure 2.1: The plasma geometry from a 'straightened out SOL' in a divertor tokamak is similar to a linear plasma device. Two divertor plates are the target materials similar to those in linear plasma devices. The 'u' in the figure represents the upstream plasma parameters such as upstream T_{e_u}, n_{e_u}.

2.3 Description of Proto-MPEX device

Proto-MPEX utilizes a high-density helicon radio-frequency (RF) plasma generator for its primary plasma production. The plasma source has been optimized at Proto-MPEX to deposit high heat, and particle fluxes to the target for PMI study [30]. Experiments in the high-density plasma ($> 3 \times 10^{19}\ m^{-3}$) discharges are normally conducted with net helicon power of $\sim$ 90-105 kW. Plasma heat and particles are transported towards the target plates that are placed 90° to the magnetic field (B) lines. The plasma produced by the helicon source travels in either direction of the antenna. Plasma traveling upstream of the helicon is terminated at the dump plate. The particles terminated at the dump plate could potentially recycle as a neutral source into the helicon region or get pumped out by the turbopump located behind the 'dump end' of the device. There are two additional turbo-pumps at the 'central chamber' ($\sim$1m downstream from the helicon antenna), and one downstream of the target spool. The initial focus of Proto-MPEX had been to optimize the helicon source to produce highly ionized plasma, and create a large neutral pressure differential [31] between the helicon source and auxiliary heating sources. Differential neutral pressure was created using skimmer plates, baffles, and turbo pumps at different axial locations.

After the helicon source optimization, in the next phase of the R&D, 28 GHz electron heating had been one of the priorities for the project. Electron heating with 28 GHz was successfully

demonstrated; however, the heating was local and confined in the B-field well at the central chamber. The aim of significant reconfiguration of Proto-MPEX geometry downstream of the central chamber has been to increase the transport of the heated particles. The upgrade to Proto-MPEX in the summer of 2018 was directed to improve the heating efficiency of ECH/EBW, and ICH. ICH antenna was reconfigured to move from being internal to external (MPEX-like) antenna. Both configurations are used to conduct experiments pertinent to this work. Subsequent subsections describe the initial (or pre-upgrade) Proto-MPEX geometry (**Configuration A**), and the reconfigured geometry (**Configuration B**).

2.3.1 Configuration A

Proto-MPEX–Configuration A has the helicon antenna about 1.2 m downstream from the dump plate, a 28 GHz ECH/EBW waveguide located at the central chamber, and the internal ICH antenna placed inside the vacuum vessel between coils 8 and 9. The schematic in Figure 2.2 shows the locations of the helicon source and secondary heating source (ECH/EBW and ICH) in Proto-MPEX for Configuration A. Twelve magnet coils produce the magnetic field along the axial length of 3.6 m from the dump plate to the target plate. A large ballast tank existed behind the target end as a vacuum dump. Two main power supplies (power supply 1, PS1, and power supply 2, PS2) set the global magnetic field, and another two set the local field around the helicon antenna (TransRex 1, TR1, and TransRex 2, TR2). Due to the variation in the magnetic field strength, spatial differences in the plasma diameter exists in Proto-MPEX (as represented by the plasma diameter in red in Figure 2.2). A flux tube mapping is required to directly compare the plasma parameters between measurements at different axial locations. The vacuum chamber

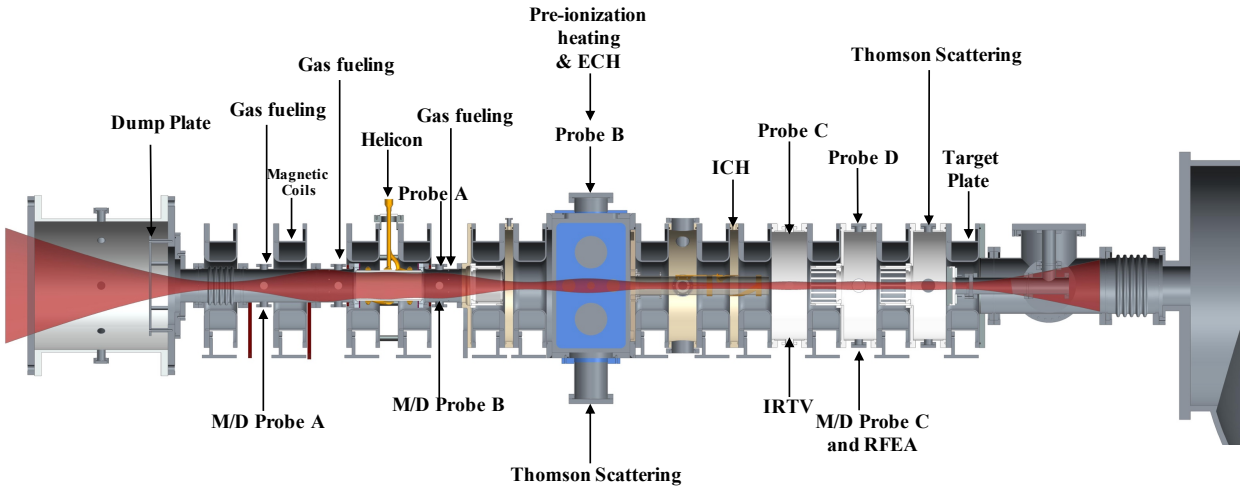

Figure 2.2: The figure shows a cross-sectional schematic of Proto-MPEX where the helicon antenna along with auxiliary heating sources, and critical diagnostics locations are located. The approximate length of the device from the dump end to the target end is about 3.6 m. The red contour represents the plasma diameter along the device.

in between of the magnets is called spools or spool pieces. For example, the vacuum chamber between magnets 1 and 2 is called spool 1.5. Text in the following chapters will occasionally use spool numbers to refer to a particular axial location.

Figure 2.3a shows on-axis magnetic field strength along the length of Proto-MPEX, and Figure 2.3b shows the location of fueling puffers (G1-G3), baratrons (P1-P4), skimmers, quartz sleeve, helicon antenna, ICH (4-9 MHz) and EBW (28 GHz) launch location, target and dump plates (retrieved from Ref. [31]). The Proto-MPEX in this configuration has three regions: 1) the source region, 2) the heating region, and 3) the target region. The central chamber, represented by the green dotted rectangle in Figure 2.3b, remains a unique axial location in Proto-MPEX where a large magnetic well exists due to two higher B-fields, provides separation between helicon and transport region.

For a typical discharge of the helicon plasma in Proto-MPEX, a relatively low magnetic field (B) is typically at 0.07 T in the helicon source region, and a peak field of 1 to 1.5 T is present downstream of the central chamber. Deuterium gas (D_2) is puffed at upstream from the helicon source at spool 2.5 in two stages, as shown in Figure 2.4a using a piezo value. Piezo fueling used in Proto-MPEX provides precise neutral fueling into the system, and it also decreased the residual gas reaching downstream heating sections. A high volume of gas is initially puffed 300 ms before the helicon RF pulse at a rate of 2.4 standard liters per minute (SLM) and is reduced to 1.7 SLM 250

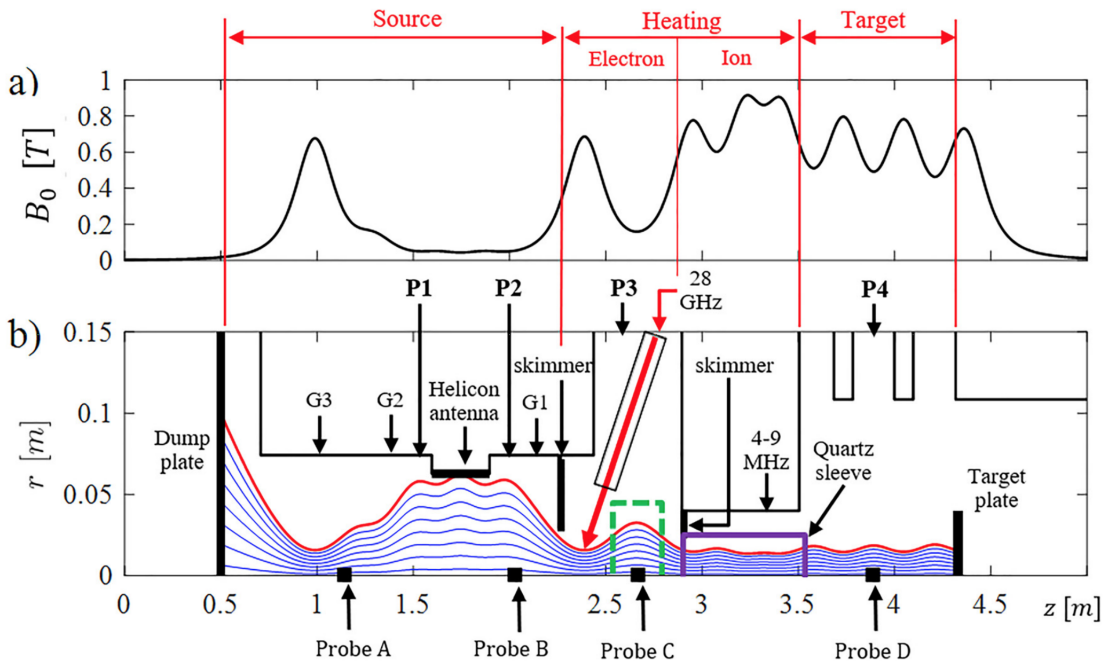

Figure 2.3: a) The top figure shows the axial magnetic field strength along the device, and (b) shows the location of fueling puffers (G1-G3), baratrons (P1-P4), skimmers, quartz sleeve, helicon antenna, ICH(4-9 MHz) and 28 GHz launch location, target and dump plates. For fueling, G1 gas value is a mass flow controller, and G2 and G3 are piezo gas value.

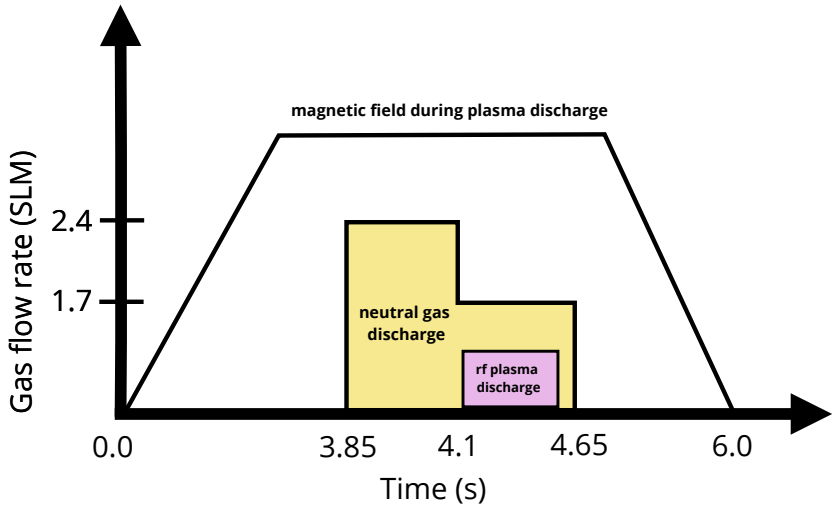

(a) Gas discharge scheme

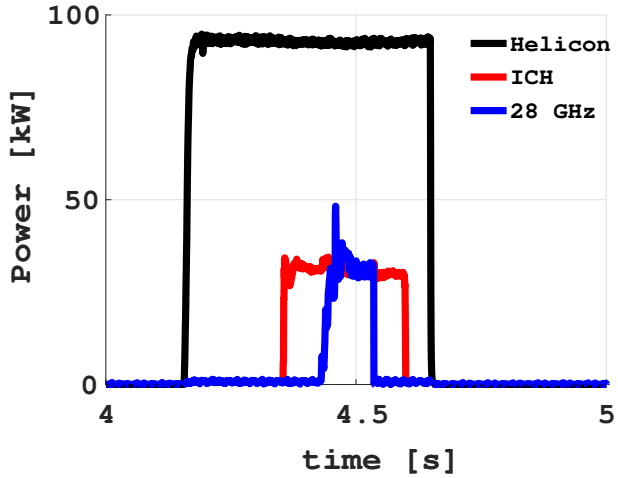

(b) Net delivered power from each of the helicon source and the auxiliary heating components.

Figure 2.4: (a) The magnets on time in Proto-MPEX is typically 6 s. The neutral gas puff signal using a piezo gas value is triggered $\sim$ 200 ms prior to the RF plasma. **(b)** Net power delivered from helicon rf source (black), ICH power (red) and 28GHz power (blue). About 90 kW of power is delivered from the helicon, and about 30 kW of power is delivered from ICH and 28 GHz.

ms after the initial puff until the end of the helicon RF pulse. Typically, the net delivered helicon RF power is 105 kW for 150-500 ms. Figure 2.4a also shows a ramp-up of the magnetic field at t = 0, a flat-top from t = 2 s to 5 s, and then the magnetic field ramped down after the discharge. The complete sequence lasts around 6 s after initiation. Table 2.2 shows the amperage on each coil, where the global field has 5900 A, and local field has 260 A to generate an axial magnetic field shown in Figure 2.2. Operational parameters mentioned here are used to obtain results presented in chapter 5 for helicon only discharges.

This is not the main thrust of this thesis, but a motivation for this work comes from power balance analyses from experiments which showed about 1-5% of the power exiting the source region is reaching the target. Understanding the physics of plasma transport has become critical in designing the components of MPEX. Understanding the plasma transport from the source to the endplates (dump and target) includes knowledge of plasma loss from various mechanisms such as radiative, recombination, and ionization losses [32], however, this is not the main thrust of this work. Other works have shown that the nominal helicon power provided to the helicon-antenna is about 100 kW, of which about 20% gets reflected, and about 2-3% is lost as a resistive loss at the copper helicon antenna; $\approx$ 78kW of net power delivering is available to produce plasma [33]. The majority of the net helicon power delivered in Proto-MPEX is lost in the helicon region during atomic and molecular dissociation of the diatomic deuterium. A rigorous analysis of the power accounting has been conducted previously along Proto-MPEX; however, the magnetic field configuration has been transformed since then. The new magnetic field in Configuration B needs new power accounting analyses for helicon-only and helicon with auxiliary heating plasmas.

2.3.2 Configuration B

Due to the presence of the magnetic mirror (will be discussed in Chapter 7) and its influence on the transport of the heated electrons towards the target, in 2018, Proto-MPEX has been reconfigured downstream of the central chamber to improve the delivery of heated particles. As shown in Figure 2.5, in the new Configuration B, the ECH/EBW heating source location has been moved downstream of the central chamber, and an external ICH antenna has been installed to mimic MPEX design. An additional magnet was added near the target to keep the length of the device approximately the same. Moreover, in addition to PS1 and PS2, power supply 3 (PS3) was added to provide independent control of the magnetic field in the source region, heating region, and

Table 2.2: Coil current [kA] values used for generating B field as shown in Figure 2.2

Coils	1	2	3	4	5	6	7	8	9	10	11	12
I [kA]	5.9	0	0.26	0.26	0	5.9	5.9	5.9	5.9	5.9	5.9	5.9
PS	PS2	TR1	TR2	TR2	-	PS2	PS1	PS1	PS1	PS1	PS1	PS1

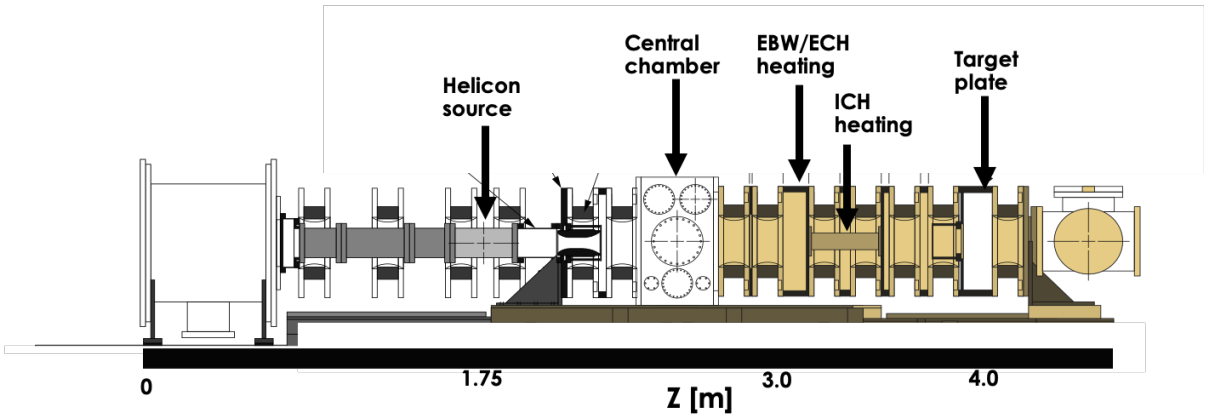

Figure 2.5: The figure shows a cross-sectional schematic of Proto-MPEX showing unmodified helicon region represented in black and white, and modified region downstream from the 'central chamber' represented in yellow. A new ECH/EBW heating system installed between coils 8 and 9, and an external ICH antenna between coils 9 and 10.

the target region. The power supplies, however, were rearranged where TransRex 2 was used to supply current to Coils 1 and 6, PS3 was used to for coils 3 and 4, TransRex 1 was was used for coil 2, PS1 for coils 7 and 8, and PS2 for coils 9 through 13.

Some of the smaller spool pieces replaced larger ones present in Configuration A, which made the device length shorter. Figure 2.6a shows the on-axis magnetic field map, and Figure 2.6b shows the plasma radius with gas fueling locations, skimmers, heating and target location for upgraded Proto-MPEX configuration. The gas fueling locations (G1-G3) have been kept the same, with location G2 used for most of the experiments presented in this work. Fast pressure gauges (also called baratrons) P1-P4 measured neutral pressure along the device. One of baratrons from the source region was moved to the new EBW heating section. The target spool dimension was kept the same, but the number of diagnostics port was increased from four to sixteen to increase the diagnostics coverage in the target region. Figure 2.7 shows the modified target spool with allocated diagnostics in each ports. The labels with red circle represent existing ports, and new ports in green (without 2-inch offset) and blue (with 2-inch offset) circles.

Overhill and downhill magnetic field conditions

In Configuration B, there are two magnetic field conditions implemented to study the transport plasma from the heating section to the target in the presence of EBW and ICH. The two magnetic field conditions are called the **overhill** and the **downhill**. Figure 2.8 demonstrated the two B-field conditions, where B is varied from 0.5 T and 0.9 T. When the field at the heating location is lower than the field downstream of the launcher, it is called the overhill condition, which lies in between the heating and target regions. In contrary, the downhill condition is achieved when the field at the heating region is higher than the field downstream of the launcher. Switching between two field conditions creates a small variation in the magnetic field in the heating section. The B-field upstream in the source region remains constant. Table 2.3 shows the current in each coil and the associated power supplies to obtain the overhill magnetic field condition.

Overhill and downhill conditions are achieved by changing the current in power supply 2 (PS2) from 3.5 kA to 1.85 kA; during this, all other power supplies are kept constant. Figure 2.8 shows the two magnetic field conditions where the magnetic field downstream from the 28/105 GHz launcher varied from 0.5 T to 0.9 T. These magnetic configurations are used in Ch. 6 to compare the axial transport behavior with and without 28 GHz EBW heating.

Table 2.3: Coil current [kA] values to generate B field favorable for EBW resonance heating

Coils	1	2	3	4	5	6	7	8	9	10	11	12	13
I [kA]	3.5	0.54	0.18	0.18	0	3.5	2.2	2.2	3.5	3.5	3.5	3.5	3.5
PS	TR2	TR1	PS3	PS3	-	TR2	PS1	PS1	PS2	PS2	PS2	PS2	PS2

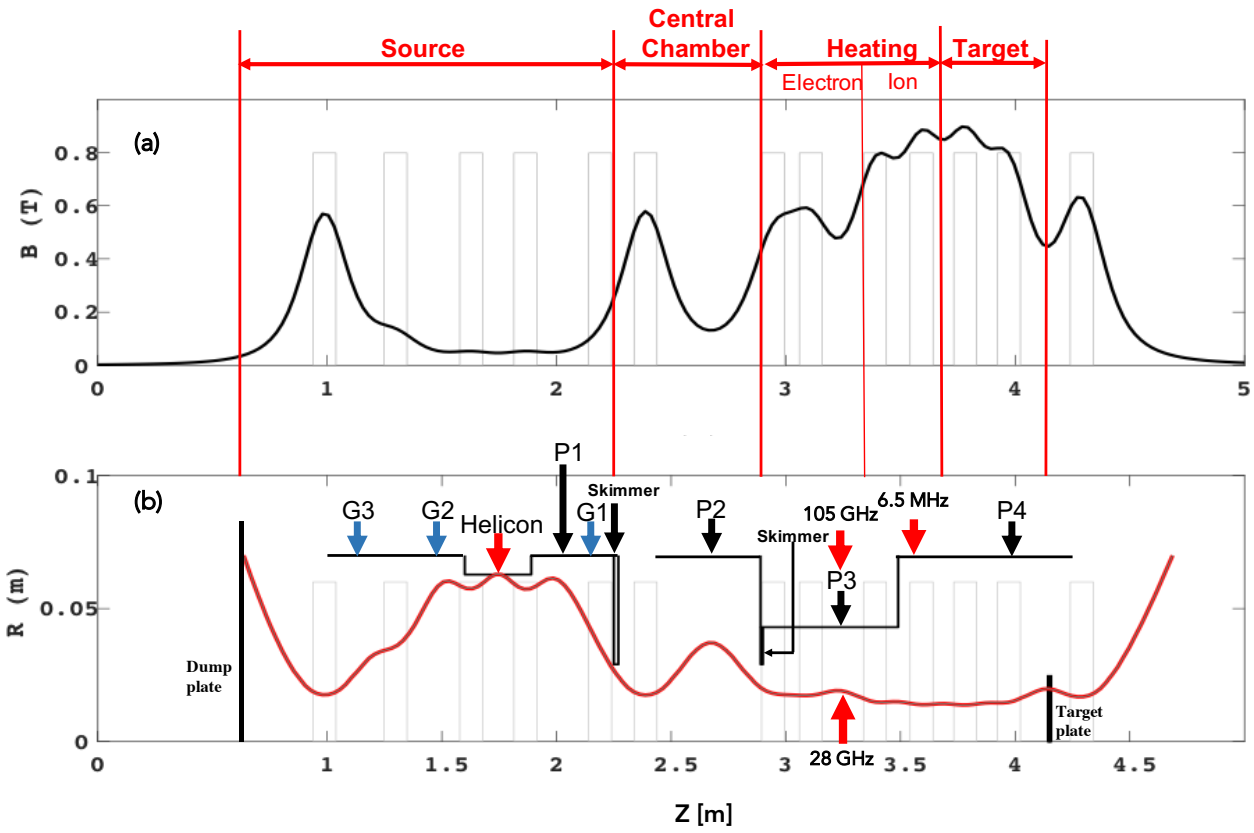

Figure 2.6: **(a)** The figure shows the axial magnetic field strength. **(b)** shows the axial plasma profile and the location of fueling puffers (G1-G3), baratrons (P1-P4), skimmers, helicon antenna, ICH (6.5 MHz) and ECH (105 GHz), and EBW (28 GHz) launch location, target and dump plates for upgraded Proto-MPEX.

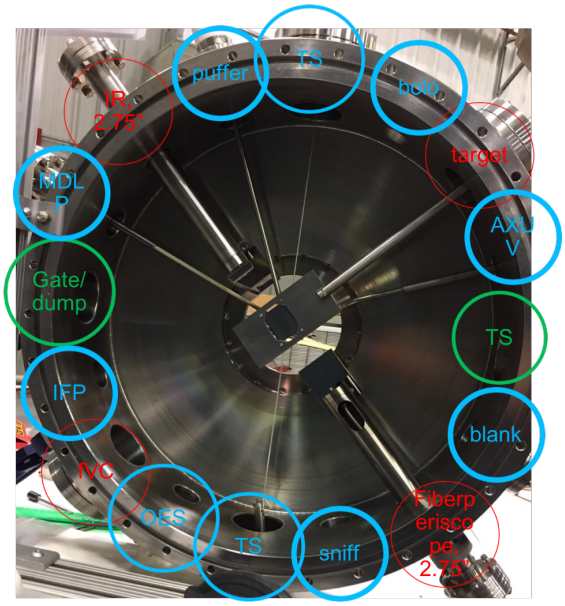

Figure 2.7: Modified target spool piece with additional 12 ports and labels for some allocated diagnostics

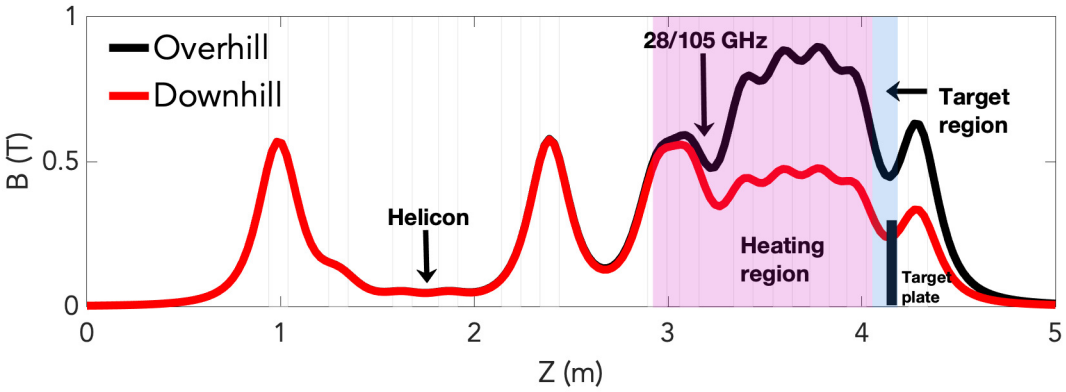

Figure 2.8: Overhill and downhill magnetic field condition used during EBW experimental campaign in configuration B. The magnetic field at the helicon source remain unaffected.

2.4 Power source in Proto-MPEX

As mentioned earlier, a helicon RF antenna is the primary power source for plasma production in Proto-MPEX. The development of the helicon system in Proto-MPEX has made substantial progress, and has produced high electron density plasmas ($\sim 1.2\times10^{20}$ m^{-3}). The density achieved is Proto-MPEX is one of the highest n_e ever produced in linear helicon plasma devices. Additional ion and electrons heating is applied using ion cyclotron heating (ICH) and electron cyclotron heating (ECH) or electron Bernstein wave (EBW) heating. The remainder of this section discusses each power source in further detail.

2.4.1 Helicon plasma source

The first instance of helicon wave plasmas was presented by Lehane and Thoneman [34]. Helicon waves satisfy the whistler wave dispersion relation in the frequency range bounded by the ion and electron cyclotron frequency and plasma frequency, $\Omega_i \ll \omega < \Omega_e \ll \omega_{pe}$ [35, 36]. The helicon wave is given by Eq. (2.1),

$$\omega \simeq \frac{|\Omega_e|}{\omega_{pe}^2} c^2 k_{\parallel}^2 \tag{2.1}$$

where $\Omega_{i,e}$ are the ion and electron cyclotron frequencies, ω_{pe} is the plasma frequency and $k_{\parallel}$ is the parallel wavenumber, ($\mathrm{k}_{\parallel} = \frac{2\pi}{\lambda}\hat{\mathrm{k}}, \lambda$ is the wavelength) in the direction of the wave propagation, and ω is the angular frequency.

Helicon devices typically produce electron densities in the order of 10^{18} m^{-3}, but experiments have shown n_e increased an order of magnitude with the presence of peak magnetic field downstream from the helicon source [37]. It has been experimentally shown that in order to effectively couple power into the helicon-mode (and thereby increase the density in the target region), the mirror ratio in Proto-MPEX must be set to greater than five [38]. Mathematically, mirror ratio is defined as the ratio between the maximum B-field to the minimum B-field $\left(\mathrm{R_m} = \frac{\mathrm{B_{max}}}{\mathrm{B_{min}}}\right)$. Details of mirrors and their effects are discussed in Sec. 7.2. The helicon waves in Proto-MPEX has successfully produced high electron density discharges in the range of $3-10\times10^{19}$ m^{-3}. Proto-MPEX has made significant progress in understanding the transition from Trivelpiece-Gould (TG) wave absorption at the outer radius of the plasma column to helicon wave absorption in the core by exciting the helicon mode. During the helicon mode, uniform plasma with a flat T_e and centrally peaked n_e profiles have been experimentally observed [25, 37, 39]. As discussed in Refs. [37, 40], Eq. (2.2) shows the relationship between the electron

density and the wavenumber,

$$n_e = T\frac{k_{\parallel}}{\omega}\frac{B}{e\mu_0}, \tag{2.2}$$

where T is the radial wavenumber. The relationship shows an increase in n_e as a function of the magnetic field ($|B|$) in the helicon region. However, the available power restricts the increase in n_e with the magnetic field strength. Increase in the helicon power could allow Proto-MPEX to operate at higher electron densities.

2.4.2 Auxiliary wave heating

The underlining idea for wave heating is to transmit RF generator waves frequency into the plasma, which is very close or equal to the cyclotron frequency of the ion or electron ($\Omega_{i,e}$). As an illustration, in Figure 2.9, ICH antenna excites plasma with a frequency (ω) near the edge of the core plasma. The plasma wave transported towards the center of the plasma gets absorbed ideally near the resonance ($\omega = \Omega$). The kinetic energy transferred with the plasma wave motion through collision will result in heating of the plasma. Depending on the RF generator frequency, the resonance region varies along the radius (r) [6].

Figure 2.10 (retrieved from Ref. [6]) shows the dispersion relation for various waveform propagating parallel and perpendicular to B-field in a cold plasma. The electric field of each wave varies sinusoidally with space and time which is given by,

$$E = E_0 e^{i(kx-\omega t)} \tag{2.3}$$

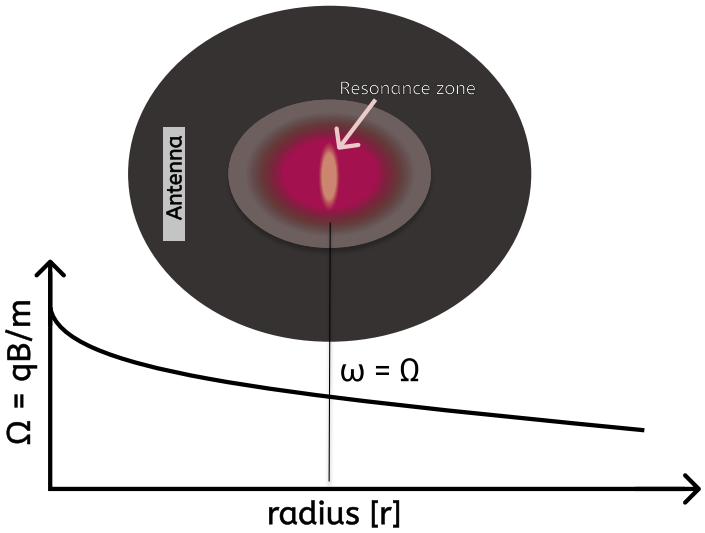

Figure 2.9: Location of resonance zone at specific magnetic field and radius, r.

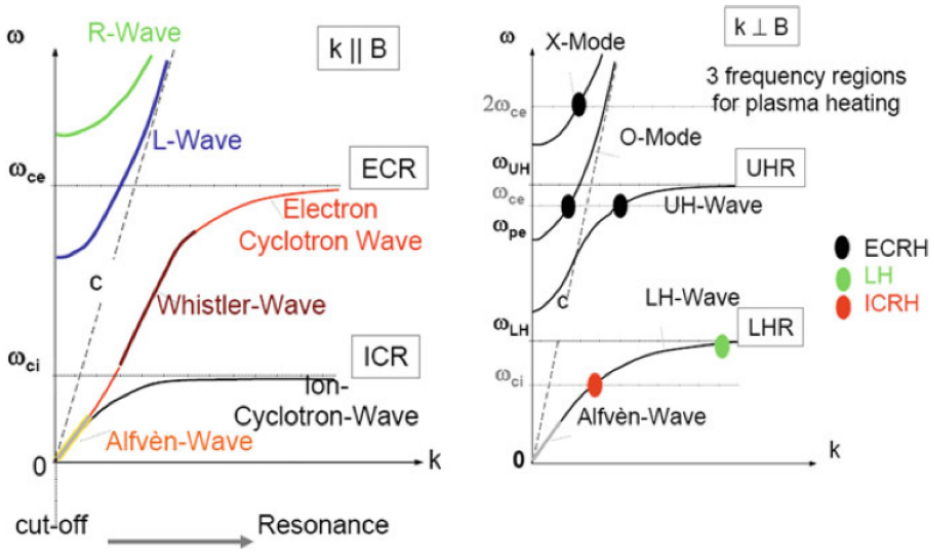

Figure 2.10: The dispersion relation for electromagnetic waves propagating parallel and perpendicular to the magnetic field in a cold plasma

where the total electric field is the sum of all the individual electric fields. Taking the derivative with respect to t of the real portion for a constant point we have

$$\frac{d}{dt}(kx-\omega t)=0;\ \ \frac{dx}{dt}=\frac{\omega}{k}=v_\phi \tag{2.4}$$

where v_ϕ is the phase velocity which tells about the speed the wavefield travels at that can be above the speed of light. While on the other hand, the group velocity is $\frac{\partial\omega}{\partial k}=v_g$ which only tells how fast the amplitude is changing, or the velocity with the energy of the wave is traveling. Figure 2.10 also shows the three frequency regions where the plasma can be heated adequately. Plasma resonance heating also occurs at higher harmonics (i.e. $\omega=2\Omega$), but above second harmonics the absorption might become less effective. Places where $k\rightarrow\infty$ or index of refraction ($n=\frac{ck}{\omega}$) goes to infinity resonance occurs, and this is where absorption of the wave takes place. In the opposite case where n goes to zero cutoffs occurs and the wave cannot propagate [41].

Ion heating

Ion cyclotron resonance heating is beneficial because it transfers energy directly and mainly to the ions, which maximizes efficiency. Power is delivered to the plasma using an antenna. A rotating electric field produced from the antenna interacts with the gyration motion of the ions. Ions see a constant field in its rotating frame, and the field increases the gyro (tangential) motion of the ions and increases ion energy. Collisions between resonate ions and other ions thermalize the energized ions. RF current oscillates back and forth in the strap antenna inducing

electromagnetic waves that propagate towards the plasma. ICH antennas ideally would launch only fast magnetosonic waves. The dispersion relation of magnetosonic wave (which occurs for $k \perp B$) is shown below in Eq. (2.5),

$$\frac{\omega^2}{k^2} = c^2 \frac{v_s^2 + v_A^2}{c^2 + v_A^2} \tag{2.5}$$

where v_s is the speed of ion acoustic wave, and v_A is the speed of the Alfven wave. However, when the antenna's current strap is not aligned it excites both fast and slow waves. Fast and slow waves are defined about the wave normal surface. The wave normal surface is the locus of the phase velocity vector. As the name implies, slow waves trace the wave normal surface with smaller phase velocity magnitude and fast waves trace with larger phase velocity [42].

In tokamaks, one can launch the slow waves can more easily from the low field side due to the difficulty in locating the antenna on the inner wall. Moreover, the required left-hand wave polarization is strongly screened by the plasma in the case of single species heating, so that heating is usually done through minority heating of a species that is only a small percent of the total; therefore for a D plasma H or ^{3}He can be used as minority species. However, as an advantage, in linear plasma devices, slow waves are launched from the high field side, which is not the case for tokamak devices, and fast waves are launched from the low field side and tunnel through an evanescent layer to the cutoff layer where propagation begins. Unlike tokamaks, ICH in linear devices does not require the lighter minority species; however, ICH would still be useful in heating single or multiple species. In the 60s and 70s, linear devices such as the Tara Tandem Mirrors first studied ICH in fusion devices. However, once mirror devices were defunded no significant research with ICH system has been done in linear devices. NASA, in collaboration with the University of Houston, and Ad Astra is doing most recent work with ICH. The collaboration is studying a space propulsion rocket engine in its Variable Specific Impulse Magnetoplasma Rocket (VASIMR) device by converting plasma energy into momentum.

Proto-MPEX has installed 6-9 MHz RF antenna for ion cyclotron resonance heating. Several source and heating system configurations in Proto-MPEX can be seen in the schematic presented in Figure 2.2. The ICH antenna is installed between the 28 GHz system and the target. A baffle has been installed in the ICH antenna area to reduce the neutral density, which otherwise could absorb heated ion energy due to collisions or also introduce cold ions into the plasma due to charge exchange reactions. One of the vital diagnostics for directly measuring the effectiveness of the ICH system is a retarding field energy analyzer. Setting fluctuating bias on the potential grid of the retarding field energy analyzer can tell the ion energy distribution. The use of the optical spectroscopy measures plasma ion temperature using Ar-II lines. Other diagnostics tools such as Langmuir probes can be used to measure plasma potential. Microwave interferometry and Thomson scattering can be useful tools to measure plasma density.

Electron heating

In recent studies, two forms of electron heating considered in Proto-MPEX are Electron Bernstein Wave (EBW) heating, and Electron Cyclotron Heating (ECH). As oppose to antennas, electron resonance wave heating is injected into the plasma using waveguides. ECH excite both ordinary (O) and extraordinary (X) mode waves. Both of these waves have $k \perp B_0$, but for the O wave, magnetic field is parallel to the electric field (i.e., $E \| B_0$), and for the X wave $E \perp B_0$ [41]. Another caveat for the O and X modes is the presence of a cutoff in high densities plasmas [6]. For 28 GHz heating the density cutoff in Proto-MPEX is around $1e19m^{-3}$ for the O-mode cutoff. Due to this reason, O-X-B EBW is used, which can heat at Doppler-shifted cyclotron resonances at any densities above the cutoff, as shown in Figure 2.11 (Credit: Cornwall Lau from Oak Ridge National Laboratory).

Experimental evidence has shown resonant heating at the edge of the plasma column, and continuous deposition of power to the core using EBW has been the most efficient method of heating the plasma in Proto-MPEX. The preferred resonance heating condition has been with the 28 GHz gyrotron at 0.5 T second harmonic fields. General Ray Tracing code for 3D plasmas (GENRAY-C) is used to predict the 28 GHz wave launch location, angle into the vacuum vessel with most suitable coupling efficiency. The O-mode is launched from the gyrotron typically at 40-50 kW power, which mode converts to X-mode at the O-mode cutoff which again mode converts to EBW at the upper hybrid layer [43, 44, 45, 22].

Electron heating in Proto-MPEX has been launched at two different locations. Experimental evidence of electron heating in Proto-MPEX has been observed at both launch locations [46]. Proto-MPEX reconfiguration was required, however, to improve the power delivery to the target. Sec. 2.3 will discuss Proto-MPEX configurations and launch location of the plasma source and auxiliary heating. Figure 2.12 is a sample image from the infra-red camera of the target plate showing the heat flux with the helicon only plasma discharge and with the addition of ECH heating. The heat flux is observed to have increased near the 28 GHz launch location. Proto-MPEX is currently implementing second harmonic 104.9 GHz ECH heating. At 104.9 GHz, plasma

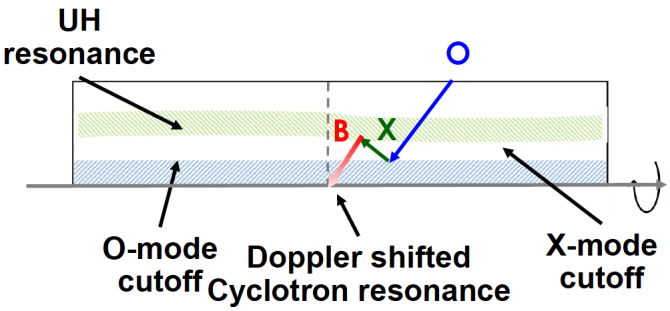

Figure 2.11: Schematic of O-X-B mode conversion for EBW heating in Proto-MPEX

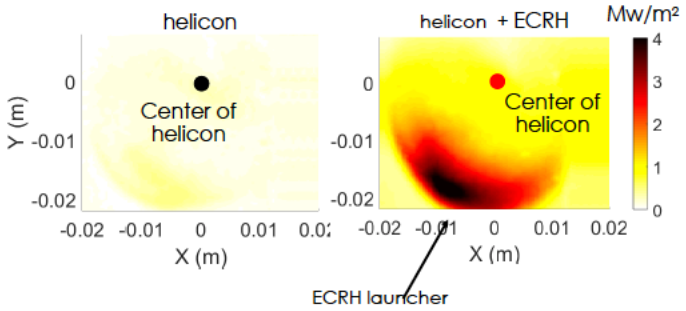

Figure 2.12: Infra-red camera image of the heat flux deposited int the target plate in Proto-MPEX. (**Left**) The heat flux on the target from helicon only discharge, and (**Right**) heat flux on the target with the addition of 28 GHz launch.

densities $> 10^{20}$ m^{-3} with B∼1.8 T is required at the heating location to be above the O-mode cutoff.

2.5 Dissertation goals

The overarching goal of the dissertation is to understand and quantify the plasma transport from the source to the target region for helicon and helicon with 28 GHz plasmas in Proto-MPEX. The axial plasma transport analysis is done using the electron temperature and electron density along the device from different diagnostics methods. The dissertation aims to the study of axial heat transport by identifying the dominating method of heat transport (conductive or convective) and the axial flow pattern. The heat transport study is useful to categorize plasma into two dominant transport regimes: sheath-limited regime and conduction-limited regime. The governing heat transport phenomenon will enable us to ascertain a particle transport regime present in Proto-MPEX. Proto-MPEX has several magnetic mirrors which is required for the proper operation of its power sources. The dissertation will study the effects of magnetic mirrors for desired operating scenarios. Moreover, this work will also investigate and analyzing plasma behavior in the presence of magnetic mirrors for different heating scenarios.

Chapter 3

Probe diagnostics in Proto-MPEX

An extensive suite of diagnostics is available for plasma characterization in Proto-MPEX. The diagnostics available for Proto-MPEX include (but are not limited to):

1. Baratrons (Neutral pressure)
2. Filterscopes (Light emission from plasma)
3. IRTV (Target temperature)
4. Fast Visible Camera (Plasma dynamics)
5. McPherson Spectrometer (Spectroscopic measurement of T_i)
6. Retarding Field Energy analyzer (Ion energy distribution)
7. Thermocouples (Wall temperatures)
8. Mach Probes (Mach numbers)
9. Thomson scattering (electron temperature and density)
10. Soft x-ray diodes (energetic particles presence)

In this work Thomson scattering (TS), double Langmuir probes (DLP), and Mach probes (MP) are central to providing electron temperature (T_e), electron density (n_e) and Mach number (M). This chapter presents descriptions of various probe diagnostics and analyses of the error quantification of a single tip Langmuir probe along with a description of double Langmuir probe and Mach probe.

3.1 Single Langmuir probe

Langmuir probes are inexpensive and straightforward tools used for measurements of basic plasma parameters such as the electron temperature (kT_e), plasma density (n_e), floating potential (ϕ_f), and plasma potential (ϕ_p), especially, in the low temperature regime. However, trade-offs associated with its relatively simple design arise when the current-voltage (I-V) characteristic from a single tip uncompensated Langmuir probe becomes distorted in radio frequency (*RF*) plasma discharges leading to inaccurate electron temperature and density measurements [47, 48]. Many active and passive compensation techniques have been developed to minimize the RF effect on Langmuir probes traces [49, 50, 51, 52, 53]. Work done by Oksuz [54] shows that the electron temperature from an uncompensated Langmuir probe can be obtained from a moderate oscillation when the electron currents are fitted to the linear part of logarithmic ion saturation current; however, quantification of the error on the extracted electron temperature and density has not been conducted.

The purpose of this work is to quantify the error in kT_e obtained from an uncompensated single tip cylindrical Langmuir probe experiencing a sinusoidal RF plasma potential (ϕ_{RF}). This work will attempt to quantify the ϕ_{RF} limit at which a single tip cylindrical Langmuir probe can be utilized without a significant error induction on the measured kT_e. Above this limit, the use of compensation or a double tip Langmuir probe [55, 56] is required. Proper RF compensation for single tip Langmuir probes can be delicate, and the electronics required to drive a double tip Langmuir probe are nontrivial; therefore, knowledge of this limit is essential.

3.1.1 Plasma sheath

Presence of a plasma sheath is an essential physical phenomenon in plasma physics. The plasma sheath is formed in surfaces where plasma-wall interaction takes place. Langmuir probes are solid surfaces inserted into the plasma; therefore, understanding the concept of plasma sheath is beneficial. To understand the plasma sheath, we need to consider a plasma in a vacuum vessel with a finite size. The plasma is considered to be quasi-neutral in the bulk region; however, the electrons have larger thermal velocities compared to the ions, so they are lost faster to the walls, creating a net positive charge in the sheath concerning the wall. Debye shielding keeps the plasma potential (ϕ) near the wall, which consists of several Debye lengths (λ_D) confining the potential variation as shown in Figure 3.1 (image obtained from Ref. [41]).

The concept of Debye shielding is illustrated below. In the sheath region, an electric field (E) is created given by Eq. (3.1),

$$E = -\nabla\phi \tag{3.1}$$

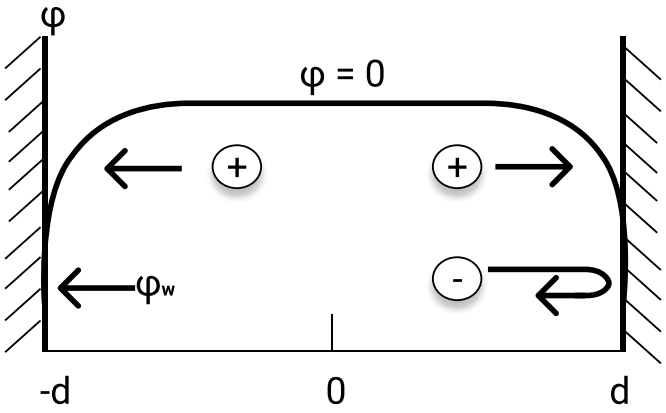

Figure 3.1: Representation of plasma potential forming sheath near walls

The electron have the tendency to go to the regions of small potential which is given by Boltzmann's relations in Eq. (3.2),

$$n_e(x) = n_0 e^{\frac{e\phi}{kT_e}} \tag{3.2}$$

where n_0 is the equilibrium plasma density. For simplicity, the ion temperature (T_i) and electron temperature are considered to be the same. Using Poisson's equation (Eq. 3.3) for singly ionized ions,

$$\nabla \dot{E} = \frac{q}{\epsilon_0} = \frac{e(n_i - n_e)}{\epsilon_0} \tag{3.3}$$

where ϵ_0 is the permittivity of free space. Using Eq.(3.1) - Eq.(3.3) we get,

$$\nabla^2 \phi = (2e^2 n_0)/(\epsilon_0 T_e)\phi \tag{3.4}$$

The quantity $\left(\frac{e^2 n_0}{\epsilon_0 T_e}\right)$ has the dimension of $[m^{-2}]$. Therefore, Debye length is defined in Eq. (3.5) as,

$$\lambda_D = \sqrt{\frac{\epsilon_0 T_e}{e^2 n_0}} \tag{3.5}$$

The potential drop exits within a few Debye lengths, but it is screened out from the rest of the plasma.

3.1.2 I-V characteristic simulation

The Langmuir probe I-V characteristic was simulated using empirical functions fitted to the simulation results of Laframboise obtained for an infinite length cylindrical tip [57]. The I-V

characteristic is a nonlinear function of the probe bias voltage (V) and is given by Eq. (3.6)

$$i_p = \begin{cases} i_e - i_i, & \text{for } V < \phi_p \\ i_e, & \text{for } V \geq \phi_p \end{cases} \tag{3.6}$$

where i_i and i_e are the ion and electron currents, respectively, drawn to the probe. We assume that $\frac{T_i}{T_e} \ll 1$ and therefore $i_i = 0$ when the probe is biased with a voltage greater than the plasma potential. The electron current is given by Eq. (3.7),

$$i_e = \begin{cases} en_e A\left(\dfrac{kT_e}{2\pi m_e}\right)^{0.5} \exp\left(-\dfrac{e(\phi_p - V)}{kT_e}\right), & \text{for } V < \phi_p \\ en_e A\left(\dfrac{kT_e}{2\pi m_e}\right)^{0.5} \left[1 + \chi_e \dfrac{e(V-\phi_p)}{kT_e}\right]^{\eta_e}, & \text{for } V \geq \phi_p \end{cases} \tag{3.7}$$

and the ion current is given by Eq. (3.8)

$$i_i = en_e A\left(\frac{kT_e}{2\pi m_i}\right)^{0.5} \chi_i \left[-\frac{e(\phi_p - V)}{kT_e}\right]^{\eta_i} \tag{3.8}$$

where A is the probe tip surface area, m_e is the electron mass, and m_i is the ion mass. The parameters χ_e, χ_i, η_e, and η_i are empirical functions of the ratio (X) of the probe tip radius (r_p) to the plasma Debye length (λ_D), $X = r_p/L_D$, used to fit the simulation results of Laframboise. The functional form can be found in Ref. [58]. For the I-V characteristics calculated in this work, r_p = 0.125 mm and l_p = 2.0 mm. We did not consider finite probe length effects and X was always greater than 3.5.

Figure 3.2 presents typical I-V characteristic categories into three regions: electron saturation, the transition region, and ion saturation. The transition region is also known as the electron retardation region. In electron saturation, the probe bias voltage is above plasma potential and only collects the electron species because $T_i/T_e \ll 1$. In the transition region, the probe begins to collect both ion and electron species as the probe bias voltage starts to become more negative with respect to the plasma potential (ϕ_p). As the probe bias voltage approaches the floating potential (ϕ_f) the current associated with the electron and ion species are equal; hence, no net current is drawn by the probe. In the ion saturation region, the probe repels a majority of the electrons. The I-V characteristics are simulated such that only $\phi_p - \phi_f$ is absolute; thus, ϕ_f can be assigned an arbitrary value and was set to 0 V for this study.

The plasma potential was modeled as the static value with the addition of an RF sinusoidal component having a magnitude ϕ_{RF}, $\phi_p \rightarrow \phi_p + \phi_{RF} sin(\omega t)$. The static plasma potential is calculated when $\phi_{RF} = 0$ by setting the probe bias voltage equal to the floating potential and solving $i_e = i_i$ for ϕ_p numerically. The instantaneous I-V characteristics are calculated over a highly discretized time mesh spanning a single RF period. The RF effected I-V characteristic is computed by taking the time average numerically; thus, ω is arbitrary within the quasi-static

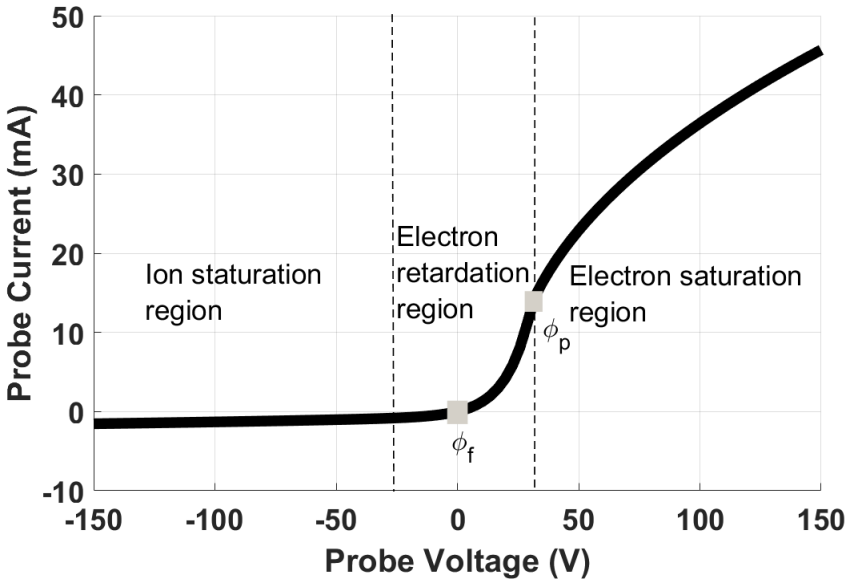

Figure 3.2: I-V characteristics of a typical single tip cylindrical Langmuir probe.

approximation. Figure 3.3 depicts a range of instantaneous I-V traces (red) associated with the discretized time mesh when $\phi_{RF} = 10$ V. The average current from all I-V characteristics yields the RF effected I-V characteristic. The ions and electrons are assumed to respond instantaneously to the difference between the probe bias voltage and the plasma potential; because the Debye length is quite small. The upper limit on the ion transient time as it falls through the sheath is $\sim$ 10 ns, which indicates that the quasi-static approximation is accurate for the typical RF operating frequency of 13.56 MHz.

3.1.3 Error quantification

Fitting the RF effected I-V characteristic to the empirical functions representing the simulation results of Laframboise determines the error induced on T_e [57]. The fitting algorithm implements a brute force method in which the entire space associated with the fit variables is discretized evenly within each dimension. The algorithm methodology is as follows: the fit quality associated with each point in the discretized space is calculated, the point in which the minima occurs is selected. The boundaries associated with space are then reduced to those adjacent to the selected point. During the iterative process, one discretizes the new space, calculates the fit quality at each point, and chooses the minimum value. The iteration takes place, typically three times or until the desired precision in the fit variables is achieved. The parameter space for this study is the electron temperature and density. The error in kT_e is defined as: $\sigma_{kTe} = \frac{kT_e^{FIT} - kT_e}{kT_e}$ and is presented as a percentage.

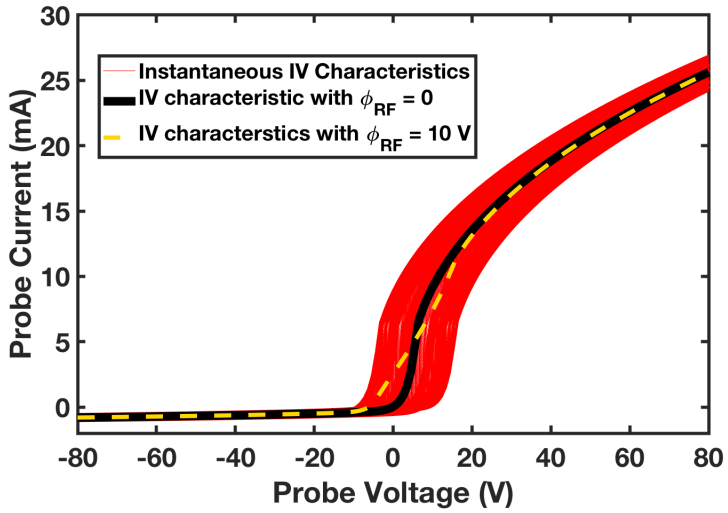

Figure 3.3: I-V characteristics for ϕ_{RF} = 0 V (solid black), ϕ_{RF} = 10 V (dashed yellow), and the instantaneous I-V characteristics (red) fluctuating between ±10 V.

3.1.4 Results and discussion

To portray the effect of a sinusoidal RF plasma potential on the I-V characteristic, a simulation was conducted with kT_e = 5 eV and n_e = 1e17 m^{-3}. Figure 3.4 presents the I-V characteristic evolution for ϕ_{RF} = 5 V, 10 V, and 15 V. The probe bias voltage spanned -100 V to 100 V, allowing coverage of all three (ion, electron saturation and transition) regions of the I-V characteristics. A nonlinear increase in σ_{kT_e} was observed with increasing ϕ_{RF},. Table 3.1 lists σ_{kT_e} (%) for the three ϕ_{RF}.

As depicted in Figures 3.3 and 3.4, the ion saturation region remains unaffected because of its nearly constant response to the bias voltage. This occurs when $X \gg 3.5$ (large probe limit $\rightarrow \eta_i \approx 0$). A negligible effect in the electron saturation region occurs due to a sufficiently linear response to the bias voltage. However, the transition region is sufficiently nonlinear; thus, the averaging effect of ϕ_{RF} significantly affects its shape. The calculations show that as the magnitude of the RF plasma potential increases, the slope of the transition region of the I-V characteristics decreases, and the floating potential shifts negatively. This distortion always results in an overestimation of kT_e when ϕ_{RF} is sinusoidal.

Figure 3.5 presents contour plots of σ_{kTe} (%) in the logarithmic scale, as function of kT_e and ϕ_{RF} for n_e = 1e17 and 1e19 m^{-3}. A linear dependency between kT_e and ϕ_{RF} is observed for a given value of σ_{kT_e}. This relationship is highlighted, for example, by the contour lines having a value of 1 and 2, which represent an error in kT_e of 10 and 100%, respectively. A fit to this linear dependence provides a quantifiable relationship between ϕ_{RF} and kT_e. Figure 3.6 presents kT_e as a function of ϕ_{RF} for two cases: σ_{kT_e} = 10% and 50%. The fitted linear trend of Figure 3.6a and 3.6b depicts that $\phi_{RF} \approx kT_e$, for $\sigma_{kT_e} \approx 10\%$ and $\phi_{RF} \approx 3 \cdot kT_e$, for $\sigma_{kT_e} \approx 50\%$, respectively. This result has two implications: first, if $kT_e \gtrsim \phi_{RF}$ then RF compensation would typically not be needed as a 10% error in kT_e is in general an acceptable value for Langmuir probe measurements. Second, low temperature plasmas are highly susceptible to RF plasma potentials, for example, a $kT_e = 5$ eV plasma having $\phi_{RF} = 15\ V$ will yield an approximately 7.5 eV — estimated from error equation shown in Figure 3.6b — if measured from an uncompensated Langmuir probe. To illustrate these points, Figure 3.7 presents σ_{kT_e} as a function of kT_e for ϕ_{RF} = 15 V. Initially when $kT_e \ll \phi_{RF}$, the error in kT_e is substantial; however, the error decreases nonlinearly with increasing kT_e to acceptable values as ϕ_{RF} is approached.

Table 3.1: The error in kT_e in percent for typically observed values of ϕ_{RF} associated with a plasma having $kT_e = 5\ eV$ and $n_e = 1e17\ m^{-3}$.

ϕ_{RF} (V)	σ_{kT_e} (%)
5	9.8
10	32.4
15	62.8

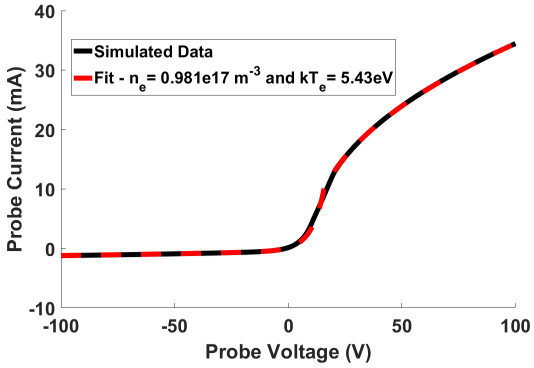

(a) $\phi_{RF} = 5\ V$

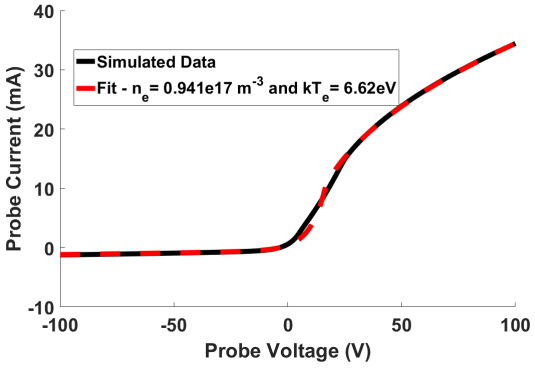

(b) $\phi_{RF} = 10\ V$

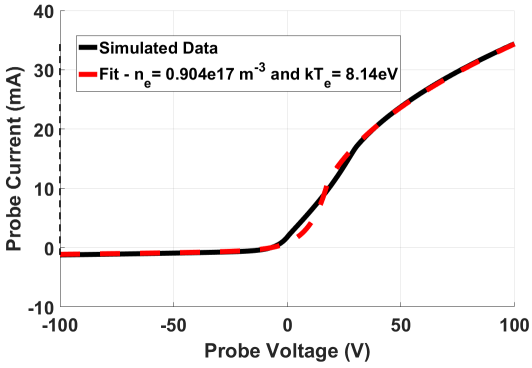

(c) $\phi_{RF} = 15\ V$

Figure 3.4: Simulated and fitted I-V characteristics associated with a plasma having $kT_e = 5\ eV$ and $n_e = 1e17\ m^{-3}$ experiencing a sinusoidal RF plasma potential of (a) 5 V, (b) 10 V, and (c) 15 V.

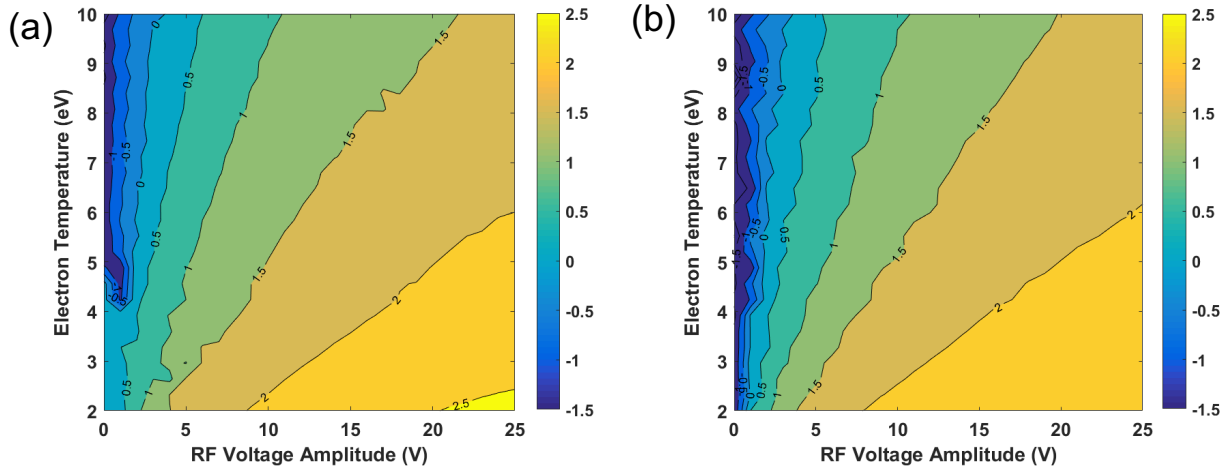

Figure 3.5: The error in kT_e as a function of kT_e for $\phi_{RF} = 15\ V$. These results are applicable to plasmas having an n_e in the range of (a) $1e17$ to (b) $1e19\ m^{-3}$.

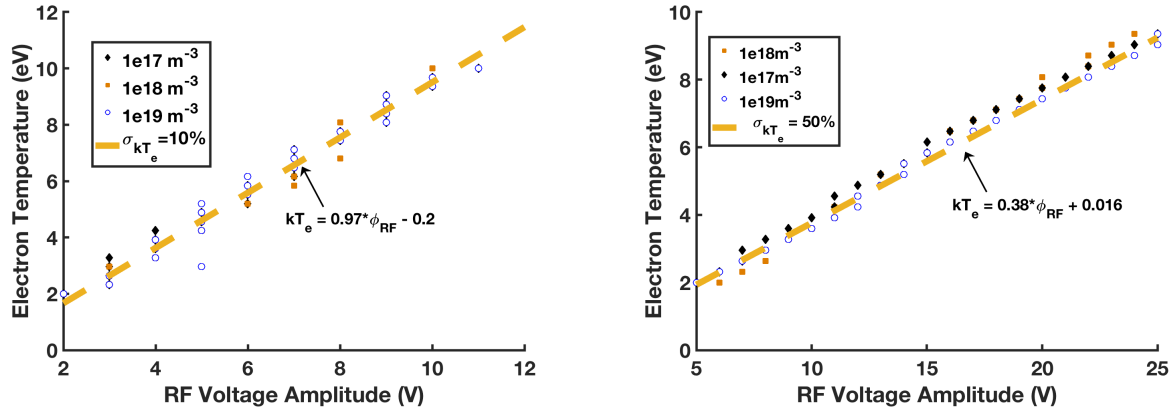

(a) $\sigma_{kT_e} = 10\%$ **(b)** $\sigma_{kT_e} = 50\%$

Figure 3.6: kT_e as a function of ϕ_{RF} for three different electron densities ($1e17\ m^{-3}$, $1e18\ m^{-3}$, $1e19\ m^{-3}$) plotted at (a) $\sigma_{kTe} = 10\%$, and (b) $\sigma_{kTe} = 50\%$, and fitted with a linear regression line.

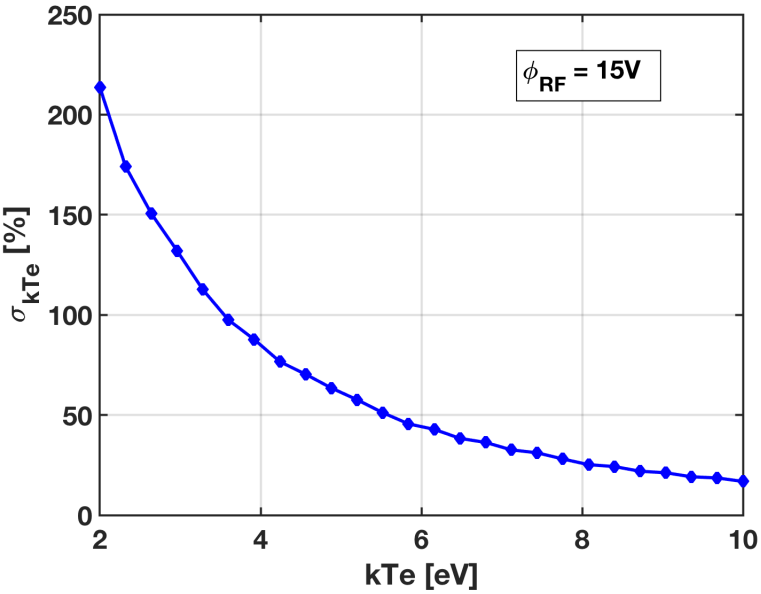

Figure 3.7: The error in kT_e as a function of kT_e for $\phi_{RF} = 15\ V$. These results are applicable to plasmas having an n_e in the range of $1e17$ to $1e19\ m^{-3}$.

Proper RF compensation for single tip Langmuir probes can be difficult, and the electronics required to drive a double tip Langmuir probe are nontrivial; therefore, knowledge of this limit is meaningful. An oscillating RF plasma potential has less effect on a Langmuir probe if the measurement is near the floating potential [59, 60]. DLPs measures T_e near the floating potential; therefore, are measuring the tail of the electron energy distribution function (EEDF) of the Maxwell-Boltzmann distributed plasma [60]. DLP also has in built intrinsic RF compensation because the two tips are referenced against each other. The use of a double Langmuir probe (DLP) has been a useful tool to measure the T_e and n_e in Proto-MPEX.

3.2 Double Langmuir probe (DLP)

Double Langmuir Probes (DLPs) are one of the most utilized diagnostics in Proto-MPEX. The previous section discussed the complication and measurement errors from an uncompensated single-tip Langmuir probe. The DLP provides intrinsic RF compensation, and are easier to implement that RF-compensated single-tip probes. With a typical sweep voltage of $\pm 50V$, and a sweep frequency of 200 Hz, DLP probes produce a discernable temporal profile for a given plasma discharge. Figure 3.8 shows a sample of electron density (left) and electron temperature (right) as a function of discharge time obtained in Proto-MPEX. The density and temperature evolution are distinguishable during the discharge, which is usually difficult to obtain from other diagnostics such as Thomson scattering system. For Maxwell-Boltzmann EEDF, electron temperature from cylindrical DLPs are weakly affected by RF rectification, but the electron density scales linearly with RF self-bias potential. The product of the ion saturation current and the slope of the I-V characteristics tends to stay the same; therefore, T_e is weakly affected [60]. Figure 3.9 depicts a typical I-V Characteristics from a DLP, where i_0 is the current collected by each probe tip during the voltage sweep. Fitting the slope of the I-V trace at V = 0 provides T_e. 3.2.1 provides the mathematical formulation in the T_e and n_e calculations from a DLP.

Figure 3.10a shows an image of a DLP probe head in Proto-MPEX. A two-bore Al_2O_3 ceramic tube isolates two inner tungsten conductors from short-circuiting against each other. A 316 or 304 graded stainless steel placed close to the probe head works as an RF electrostatic shield, as depicted in the image. A single bore ceramic tube provides an outer covering for the probe to avoid direct contact between the plasma and any metal surfaces other than the probe tips. The probe tip length is usually within 2 mm to minimize the current collection and reduce self-emission and even melting. A proper ground is required for the electrostatic shield for the probe to operate as desired. A ground is created using a custom-made standoff, as shown in Figure 3.10b which are in proper contact with the conical flange of the probe drives. Probe drives (Figure 3.10c) are machine grounded to maintain the same potential as Proto-MPEX vacuum vessel.

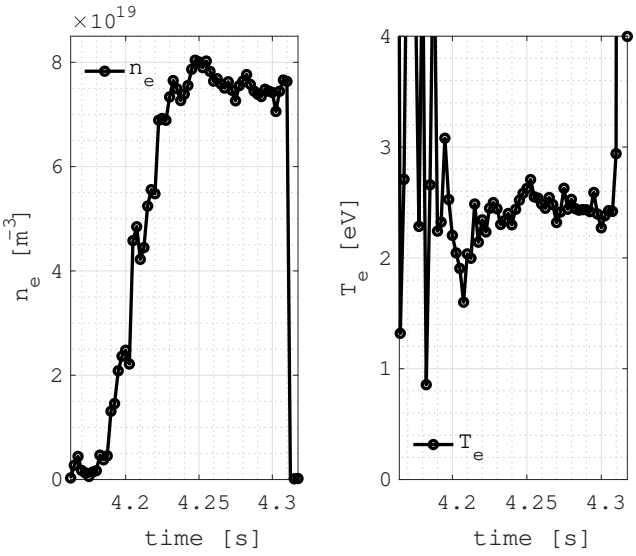

Figure 3.8: Temporal profile of (*left*) electron density and (*right*) electron temperature during a plasma discharge 300ms.

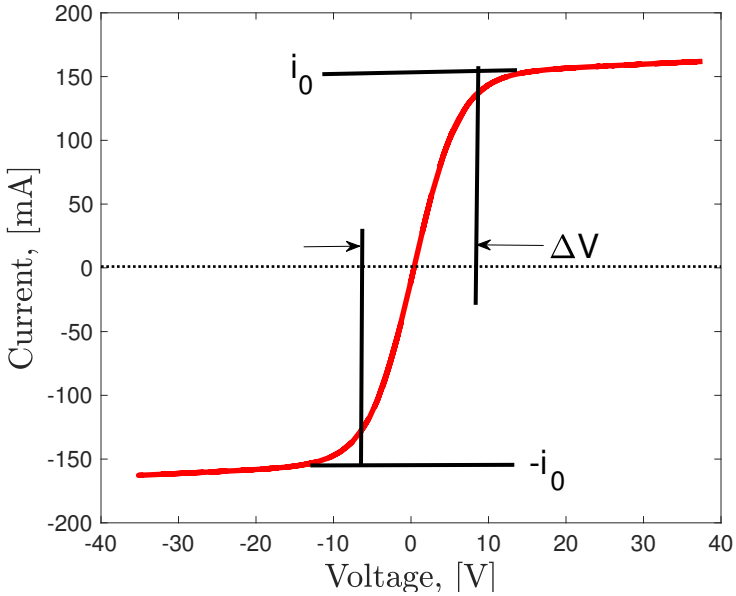

Figure 3.9: IV characteristics from a symmetric DLP where i_0 is the maximum current collected by probe tip during the voltage sweep.

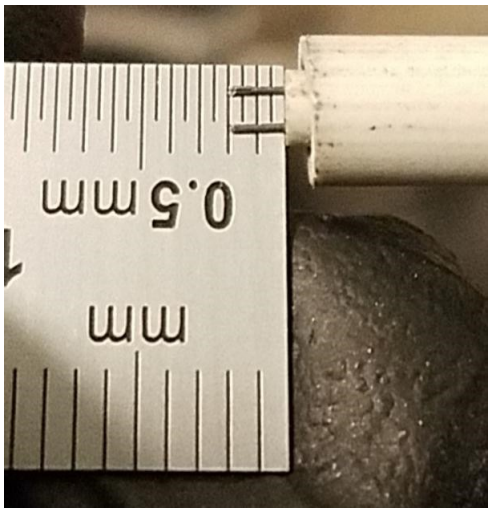

(a) Probe head

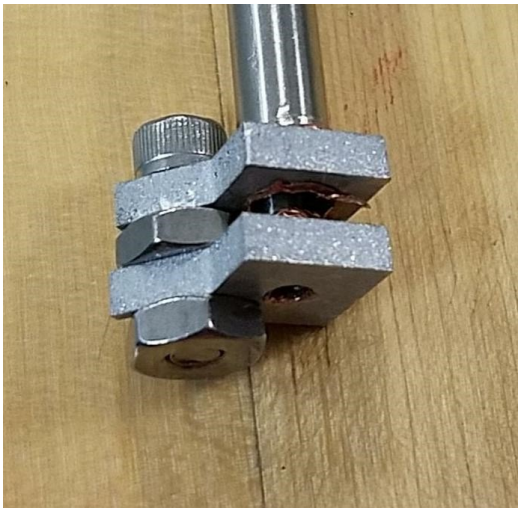

(b) Ground connection

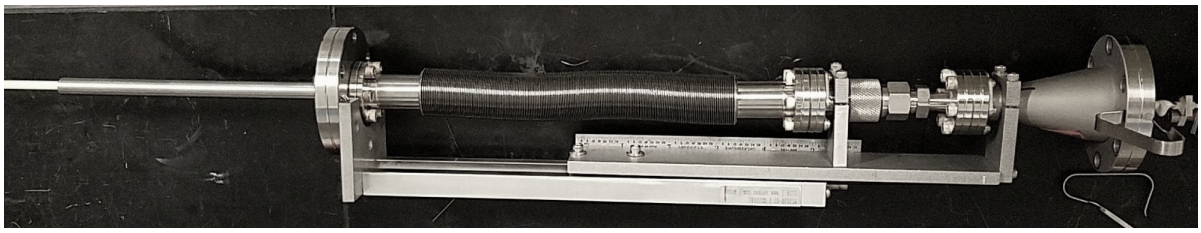

(c) probe drive

Figure 3.10: Figure (a) shows a typical double probe head where the tip length is around 1 to 2 mm, (b) shows the custom pieces made to create proper ground connection, and (c) shows the linearly translation probe drive.

3.2.1 Electron temperature and density calculation

DLP is different from SLP because in a DLP probe tip works as a reference to one another such that the probe is floating. When a voltage, V, is applied to the probe tips, the tips are electrically isolated. The double probe has two conditions to satisfy:

i) $i_1 + i_2 = 0$

ii) $V = V_1 - V_2$

The probe characteristics from each probe tip is calculated using Eqs. (3.9-3.10)

$$i_1 = i_0(e^{e(V_1 - V_f)/kT_e} - 1) \tag{3.9}$$

$$i_2 = i_0(e^{e(V_2 - V_f)/kT_e} - 1) \tag{3.10}$$

where v_f is the floating potential (The plasma potential and the floating potential cannot be calculated from a double Langmuir probe). Solving for the V_1 and substituting for i_1 we get a hyperbolic tangent equation, as shown in Eq. (3.12),

$$e^{eV_1/kT_e} = \frac{2e^{eV_f/kT_e}}{-eV/kT_e} \tag{3.11}$$

$$i_1 = i_0 \tanh(eV/(2kT_e)) \tag{3.12}$$

Once T_e is obtained from the slope of the IV characteristics $kT_e/e = i_0/(2di_1/dV)$, n_e is evaluated using Eq. (3.13)

$$\mathrm{n_e} = \frac{\mathrm{i_0}}{\left(\mathrm{eA(Z_i kT_e/m_i)^{1/2}}\right)}, \tag{3.13}$$

where Z_i is the atomic number of the ion, A is the area of the probe tip. Area of probe tip 1 and probe tip 2 can differ; however if they are the same then, $A = \pi r_p^2 + 2\pi r_p l_p$.

3.3 Mach probe

Mach probes (MPs) are one-directional electrical probes to measure plasma flow. The ratio of upstream and downstream ion saturation currents is used to measure the Mach number (M) using Eq. (3.14),

$$\frac{J_u}{J_d} = e^{kM}, \tag{3.14}$$

where J_u is the upstream ion current, J_d is the downstream ion current, and k is the calibration factor for various probes. In a directional flow, the ratio of the ion saturation currents becomes greater than one making the flow greater than the sound speed. Some of the different types of Mach probes are as follows:

- A rotating Mach probe used to measure the polar distribution of ion saturation currents,
- A Gundestrup probe which is made up of several collectors installed in the circumference of a cylindrical insulator,
- Perpendicular Mach probe, which has two tips perpendicular to each other so that it can also measure the parallel plasma flow, and
- Visco-Mach probe is used to measure parallel and normal shear viscosity [61].

The currently implemented design in Proto-MPEX has a four-bore ceramic, in which two bores are used as one-directional Mach probe, while the remaining two bores are used as double probes, as shown in Figure 3.11. Four separate conducting tips are inserted into the ceramic with an insulating ceramic between them. Simultaneous measurement of M, T_e, and n_e are therefore possible for a given location.

Circuit design to drive the Mach probes tips is shown in Figure C.1 (Appendix C). Voltage is applied to both tips simultaneously; however, longer tips are vulnerable to damage if operated for the duration of the discharge. In order to minimize the current being drawn by Tip 1 and Tip 1 a relay switch gates the probe with 5-10% duty cycle. The BNC connection from the probe has the same machine ground as Proto-MPEX. Figure 3.12 exemplifies the gated raw signal obtained from the two Mach probes tips. The Figure 3.12a shows the signal collected during the entire discharge. The upstream facing tip signal is represented by black, and the downstream facing

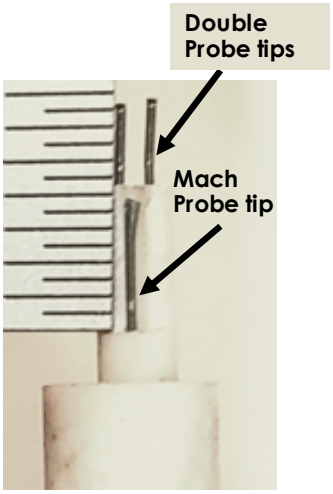

Figure 3.11: Image of Mach/double Langmuir probes (M/DLP probe). Double tip with tip length of 2 mm and one side of a Mach probe tip length of 4 mm is seen. Both DLP and Mach probes tungsten wires had a diameter of 0.254 mm.

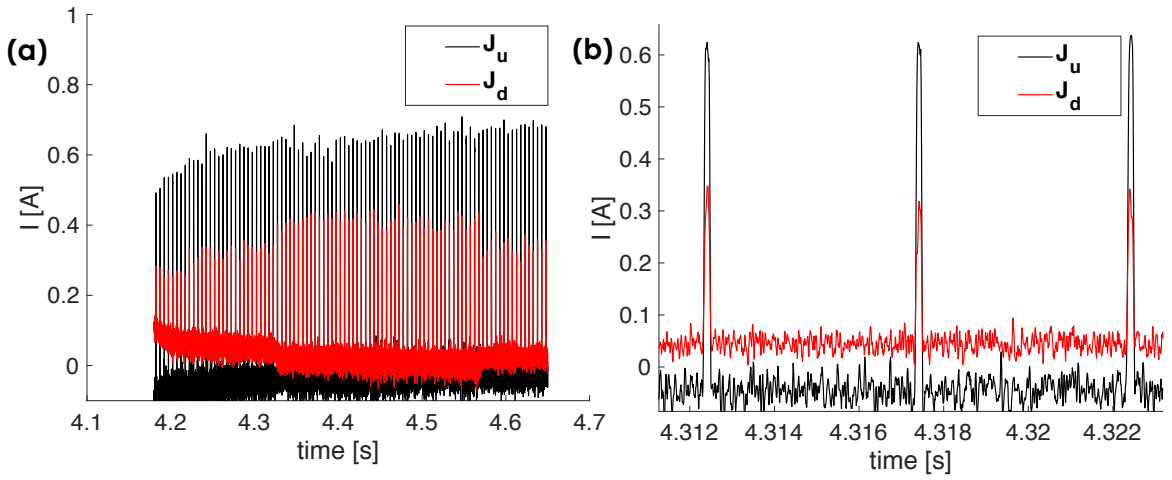

Figure 3.12: The raw signal measured by the Mach probe tips is presented in the figure where (a) shows the signal collected for a plasma discharge, and (b) shows the magnified signal during the same discharge. The probe was gated at 5 to 10% to protect from tips from overheating and damaging. The plot in black shows current collected by the upstream facing tip, and the plot in red shows the current collected by the downstream facing tip.

tip is represented by red. In this case, since the flow is directed from the source towards the target, the upstream tip is receiving higher current signal. The Figure 3.12b shows is a magnified representation of the gated signal, showing that the probe is on only for the gated duration. The probes are gated at 5 to 10% duty cycle to protect the tip from overheating and melting.

Using the Mach number, M, and T_e, the axial flow velocity (u_z) (obtained using Eq. (3.15)), and the particle flux (Γ) can be obtained.

$$u_z = M \cdot c_s \tag{3.15}$$

$$c_s = \sqrt{\frac{kT_e + kT_i}{m_i}} \approx \sqrt{\frac{2kT_e}{m_i}} \tag{3.16}$$

where m_i is the ion mass, and c_s is the plasma sound speed. Generally, electron and ion temperature are assumed to be the same, which is supported by spectroscopic data with Ar puffing, i.e. $T_e = T_i$. The particle flux is given by Eq. (3.17),

$$\Gamma = n_e u_z \tag{3.17}$$

A one-dimensional continuity equation, in Eq. (3.18), can be used to understand the axial particle transport from different flux surfaces along the device.

$$\frac{\partial n}{\partial t} + \nabla \bullet (nu) = G \tag{3.18}$$

where G is the particle generation rate.

Results from Mach/Double probes showing axial plasma flow in Proto-MPEX are some of the critical measurements used extensively in later chapters of this dissertation.

A Mach-Double probe can also be useful to identify a change in the flow pattern for helicon only and helicon with auxiliary heating discharges. The flow pattern from a radial scan from the M/DLP can also provide information on radial flow reversal or presence of any shear flow; such study is not central to the work presented but could be explored in the future.

3.4 Summary

This chapter discussed the physics behind a single Langmuir probe and its limitations while working in an RF environment. A method to quantify the error in kT_e due to a sinusoidal RF plasma potential is proposed. The findings presented here show that low temperature plasmas are highly susceptible to erroneous measurements of kT_e from an uncompensated Langmuir probe if the plasma potential has an RF component. It was found that the following relationships can be used to estimate the sinusoidal RF plasma potential magnitude (V) that will yield a 10 and 50% error in kT_e (eV), $\phi_{RF} = kT_e$, and $\phi_{RF} = 3 \cdot kT_e$ respectively. Additionally, our analysis shows that the robustness of an uncompensated Langmuir probe increases nonlinearly with increasing kT_e for a fixed ϕ_{RF}. Double Langmuir probes have been the workhorse diagnostics for plasma start-ups and some of the initial explorations in Proto-MPEX. The text discussed the physics behind measuring electron temperature and density from DLP. Double probes, however, are still perturbative, which alters the plasma downstream from the measurement location, and they are also susceptible to high heat fluxes. There have been several instances where the probe was obliterated while injecting power from the auxiliary heating systems.

Next chapter will discuss Thomson scattering, a non-perturbative, diagnostic. The motivation for the double-pass Thomson scattering laser system arose to replace perturbative diagnostics such as Langmuir probes with a robust and non-invasive diagnostic system at multiple axial locations. Langmuir probes can suffer physical damage in the presence of high localized heat fluxes from auxiliary heating, and since they also depend on simplifying assumptions in a magnetic field, they can be difficult to interpret when attempting to measure electron temperatures and densities from ECH/EBW and ICH.

Chapter 4

Thomson Scattering in Proto-MPEX

Reproduced from N. Kafle, T. M. Biewer, and D. C. Donovan,"Dual-pass upgrade to the Thomson scattering diagnostic on the Prototype-Material Plasma Exposure eXperiment (Proto-MPEX)," Rev. Sci. Instrum., vol. 89, no. 10, p. 10C107, 2018, with the permission of AIP Publishing.

N. Kafle contribution to the paper is with designing and implementing most of the hardware upgrade of the Thomson scattering system, setting up collection optics, operating Thomson scattering laser diagnostics, data collection and analysis, and writing the paper. **T.M. Biewer** oversees the development of the Thomson scattering diagnostics, and also significantly contributed to the design and implementation of hardware upgrade and data collection. **D.C. Donovan** contribution includes help with the designing of the Thomson scattering upgrade and guidance on data collection and analysis.

4.1 Introduction

Thomson scattering (TS) [62, 63, 64, 65, 66], which is non-perturbative, is one the primary diagnostics that uses an active spectroscopic technique to measure the fundamental plasma parameters such as electron temperature and density with high spatial resolution. The physics behind Thomson scattering diagnostics has been well established and allows for the electron velocity distribution to be inferred from the Doppler shift in the elastic scattering of electromagnetic radiation by a free electrons [67]. The differential scattering cross-section between the 'unpolarized' incident and the scattered electromagnetic radiation is given by Eq. (4.1).

$$\left(\frac{\partial\sigma}{\partial\Omega}\right)_{unpolarized} = \left(\frac{e^2}{4\pi\epsilon_0 mc^2}\right)^2 \left(\frac{1+cos^2\phi}{2}\right), \tag{4.1}$$

where ϕ is the angle between the incident and scattered photon and Ω is the solid angle. The total scattering cross-section is given by integrating Eq. (4.1). The Thomson scattering cross section

(σ_T) is given by Eq. (4.2),

$$\sigma_{\mathrm{T}} = \frac{8\pi}{3}\left(\frac{\mathrm{e}^2}{4\pi\epsilon_0 \mathrm{m_e c^2}}\right)^2 = 6.65\times10^{-29}\mathrm{m}^{-2}. \tag{4.2}$$

Proto-MPEX utilizes Thomson scattering for primarily measuring low T_e (1-20 eV) and high n_e ($> 10^{19} m^{-3}$). A typical schematic of an incoherent Thomson scattering measurement is shown in Figure 4.1. The figure also depicts the arrangement of the optical fiber bundle with respect to the plasma column. The white circles represent the localized volume, where the laser photons interact with a free electron, and measured using the TS system. Hence, the TS system provides the localized spatial parameters as opposed to other spectroscopy diagnostics. The electron temperature (T_e) is obtained by fitting a Gaussian to the thermal Doppler broadened Thomson Scattering spectrum (Eq. 4.3), and the electron density (n_e) is calculated using the area underneath the broadened spectrum. n_e is calculated using the Rayleigh scattering with a known N_2 pressure (see details in Appendix A).

$$\mathrm{T_e} = \left(\frac{\delta\lambda}{\lambda_0}\right)^2 \frac{\mathrm{m_e c^2}}{8\ln(2)}, \tag{4.3}$$

where λ_0 is the rest wavelength of the laser, $\delta\lambda$ is the spread in wavelength FWHM due to scattering from free electrons, m_e is the mass of the electron, c is the speed of light. A detail discussion of the Thomson scattering laser system, initial implementation and first results in Proto-MPEX can be found elsewhere [68, 69].

The existing Thomson scattering laser beam is recycled from the target region to the central chamber for the second pass. This chapter will present a brief description of the Thomson scattering diagnostic hardware in Proto-MPEX in 4.2, a detailed description of the second laser beam-line installation in 4.2.1, the results of the measurement from two locations in deuterium plasma discharges in 4.3, and also discusses the near target measurement using the Thomson scattering system in 4.4.

4.2 Thomson scattering diagnostics hardware

Proto-MPEX uses a Newport Quanta-Ray Pro 350-10 Hz laser system for its Thomson scattering diagnostic to measure electron temperature and density pulsed every 100 ms during a plasma shot. Figure 4.2 shows a photograph of the Quanta-Ray Pro laser. The fundamental wavelength of the Nd:YAG laser system is at 1064 nm, and when the laser passes through the potassium di-hydrogen phosphate (KD*P) crystals it is frequency-doubled to produce light at half the wavelength (532 nm). The maximum energy output from the laser is up to 1.4 J per 8 ns pulse. A PI MAX III intensified charge-coupled device (ICCD) camera with generation III intensifier from Princeton Instruments is used to collect the scattered signal through a Kaiser Optical Systems

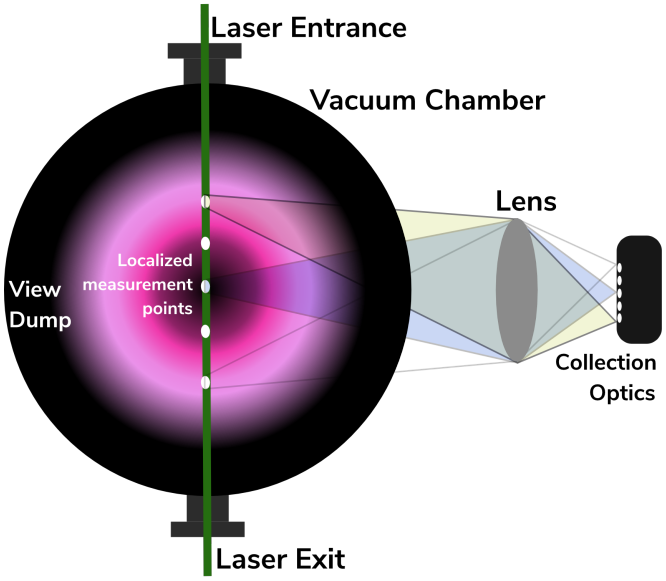

Figure 4.1: Setup of an incoherent Thomson scattering experimental configuration in Proto-MPEX. The dark core represents highly ionized deuterium plasma typically observed in Proto-MPEX. The arrangement of the optical fiber bundle with respect to the plasma column is presented. The localized volume where the light scattering after the interaction with a free electron measured from the TS diagnostics system is represented by the white dots.

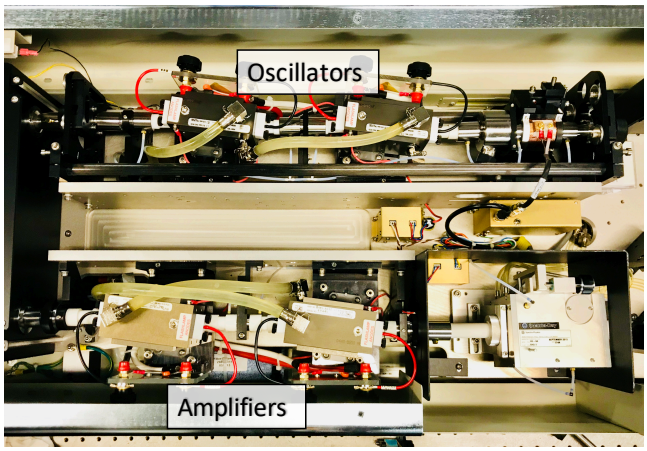

Figure 4.2: Quanta-Ray Pro 350 laser system used for Thomson Scattering in Proto-MPEX. Two oscillators are shown on the top of the image and amplifiers on the bottom (left) along with frequency doubling crystal (bottom right).

Holospec f/1.8 spectrometer. Ideally, the fiber-coupled intensifier is gated to ~ 10 ns to reduce bremsstrahlung emission detection. However, functionally a gate width of 70 ns or higher is required to accommodate timing jitter of the triggering system and to allow light to travel back from the machine to the spectrometer. Since two fiber bundles of differing lengths transport the light, the minimum gate width is effectively 100 ns to reliably record photon counts.

4.2.1 Second laser pass implementation

The motivation for the double-pass laser system arose to replace perturbative diagnostics such as Langmuir probes with a robust and non-invasive diagnostic system at multiple axial locations. Langmuir probes can suffer physical damage in the presence of high localized heat fluxes from auxiliary heating, and since they also depend on simplifying assumptions in a magnetic field, they can be challenging to interpret when attempting to measure electron temperatures and densities from ECH/EBW and ICH.

Multiple axial Thomson scattering system [64] are present in other linear devices. The upgrade in Proto-MPEX enables simultaneous measurement of axial T_e and n_e gradients between the central chamber and the target region, which will allow observing gradients in plasma parameters necessary to study plasma transport.

Figure 4.3 depicts the laser route (red dotted line) passing through two axial locations in the Proto-MPEX chamber. The figure also shows the optical arrangement and a picture of air breakdown, during a vent, at the central chamber and the target region. Figure 4.4 provides a detailed image of the optical arrangement of the Thomson scattering diagnostic system from the Nd:YAG laser source to the laser dump above Proto-MPEX. The laser traverses ~20 m from the source, located at the diagnostics laboratory, to the target region for the first pass through the vacuum vessel. The pink column represents the plasma column, and the dotted red line represents the path of the Class 1 Helium-Neon (HeNe) laser typically used during laser alignment. The amplifier rods, inside the Quanta-Ray Pro 350 Nd:YAG unit, set the output beam diameter of ~11 mm, which is then doubled using a 2×Galilean beam expanding telescope (BET), as depicted in Figure 4.4. The beam output diameter (d_o) with a given magnification at the distance, L, is given by Eq. (4.4),

$$d_o = M_p \cdot d_s + L\left(tan\frac{2\theta}{M_p}\right), \tag{4.4}$$

where M_p is the magnification power, d_s is the source diameter, θ is the beam divergence [70]. With the maximum rated beam divergence of $\theta < 0.5$ mrad, d_o obtained for $L = 20\ m$ is approximately 32 mm. Without BET (i.e. $M_p = 1$), the beam output diameter, for Proto-MPEX, would have been about 31 mm. However, the beam expanding telescope serves two purposes, 1) it expands the beam size, which reduces the power density on the steering mirrors, and 2) it

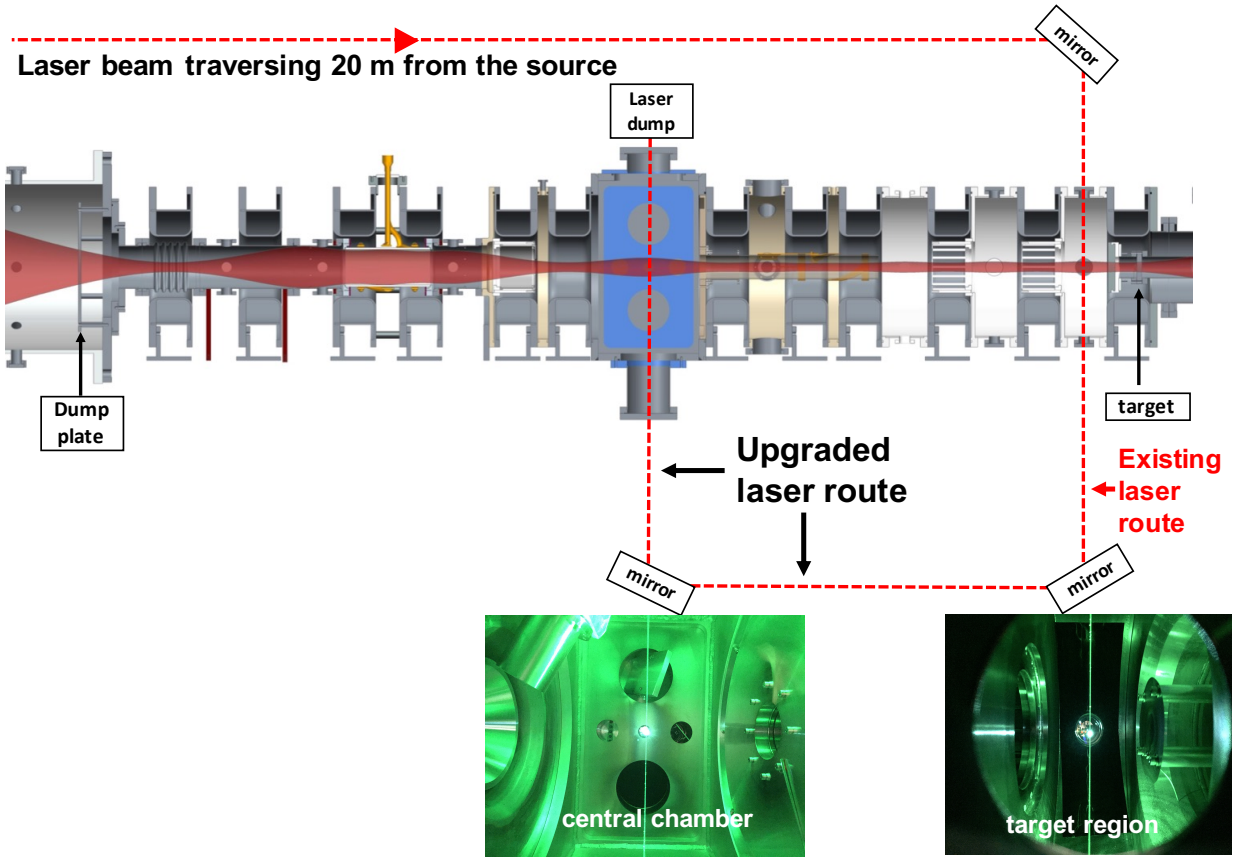

Figure 4.3: The figure shows the laser route through the Proto-MPEX vacuum chamber. The laser route existing near the target chamber, and the recently installed laser route from the 'central chamber' is shown. The red surface depicts the axial variation in the plasma diameter due to the changing magnetic field. The photographs at the bottom show the air breakdown occurring at the focal point at the geometric center of the (vented) vacuum chamber.

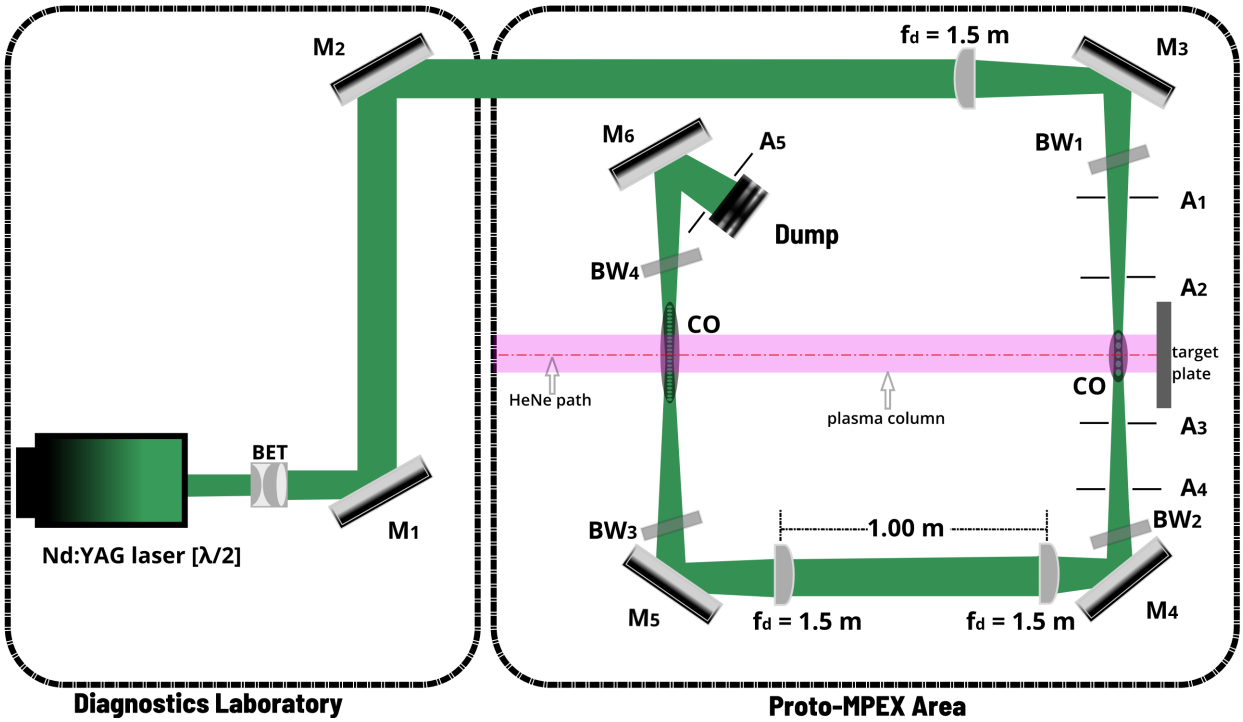

Figure 4.4: An optical schematic of the Thomson scattering diagnostic system from the diagnostics laboratory to Proto-MPEX (not to scale). In the figure, **BET**: beam expanding telescope, $\mathbf{M}_1$-$\mathbf{M}_6$: mirrors, **CO**: collection optics, $\mathbf{A}_1$-$\mathbf{A}_5$: aperture, and **BW**: Brewster window.

collimates the beam and helps in maintaining the smaller beam diameter at very long distances. Without the beam expanding telescope, $d_0 > 31$ mm is reached at L $\geq$ 22 m.

The figure also shows the position of six, 50.8 mm diameter, high energy Nd:YAG/Nd:YLF laser steering mirrors (represented as M_1-M_6) from CVI Laser Optics. All but one mirror (M_6) has remote steering capability. A 50.8 mm diameter laser grade Plano-convex spherical lens (focal distance, f_d = 1500 mm) from CVI Laser Optics is used to focus the beam at the midplane of the vacuum chamber. Without the focusing lens, the beam diameter would be ~30 mm at M_3 before entering the vacuum vessel. As mentioned elsewhere [69], the focusing lens serves two purposes: 1) it enables the laser beam to pass through the standard 70 mm conflat-flanged vacuum tube with the inner diameter of 35 mm, and 2) it focuses the laser beam to a small scattering volume to get a localized measurement. There are four apertures installed in the flight tubes for the first pass to reduce the stray light from the "Brewster angled" window, labeled as A_1-A_4 to reduce the stray light count. Apertures A_1, A_4 have 25 mm diameter, and A_2, A_3 have 20 mm diameter.

For the double-pass upgrade, the existing laser beam, after exiting from the vacuum vessel in the target region, has been directed towards the 'central chamber' using two turning mirrors (M_4 and M_5). The laser dump was removed from under the vacuum vessel at the target region, and replaced by a turning mirror (M_4). The mirror steers the laser beam parallel to the vessel towards the central chamber. At the exit of the laser enclosure box, the diverging laser beam is re-collimated using a laser grade Plano-convex spherical lens and then refocused 1 m downstream using another Plano-convex lens (f_d = 1500 mm). Another remote steerable turning mirror (M_5) then steers the laser beam into Proto-MPEX. The horizontal distance between the target region and the central chamber is measured to be about 1.5 m. Two Brewster angled windows, similar to that used for the first-pass have been installed for the second pass to minimize the reflection. Figure 4.4 shows the four vacuum to air Brewster window (BW_1-BW_4) interfaces used in Proto-MPEX. However, due to space limitation, the vibration mitigation bellows and electrical isolation ceramic breaks, which would electrically and mechanically isolate the beam enclosures from Proto-MPEX, could not be installed for the second pass. The vacuum chamber at the central chamber shapes as a large rectangular box for the auxiliary heating components. Also, a 203 mm diameter, 280 mm long conflat cross attached at the bottom left negligible space for an aperture to be added for the second pass. After exiting Proto-MPEX for the second time, the laser is dumped over a stack of stainless steel razor blades in the laser dump.

Two different sets of collection fiber optics (CO) were installed in Proto-MPEX to collect scattered photons: a 5 × 3 bundle in the target region and a 25 × 1 bundle at the central chamber. At the focal point, the laser diameter is <1 mm which only permits the use of one column of the fiber optics in the target region, but the other two columns are used for passive spectroscopic diagnostics. Moreover, the upgrade has also increased the sampling point from three fibers to five fibers measuring 3 cm radially across the plasma column in the target region, hence, increasing the spatial resolution. The new twenty-five optical fiber bundle at the central chamber spans 8 cm across the plasma radius. The collection diameter of each fiber optic is 400 microns for the near

target bundle and 200 microns for the central chamber fiber bundle. The optical fiber bundles can be translated vertically to measure different radii as required by the nature of the experiment. Due to the limitation of the spectrometer, only a total of 20 sampling points can be used at a given time (typically fifteen at the central chamber and five at the target region).

An ad hoc method was implemented to identify the vertical position of the collection optics and the horizontal position of the laser beam as to the center of the plasma column. Projected Class I helium-neon (HeNe) laser from the center dump plate to the center of the target defined the axis of the plasma column, (red dotted line in Figure 4.4). The HeNe was projected at the center of the target hot spot so that TS would measure the highest possible T_e and n_e. The point where the Nd:YAG, HeNe and the focused collection optics met gave the alignment of the laser beam and the collection optics to the axis of the plasma column.

Before the upgrade, the laser source, which is about ∼20 m, was presumed to be sufficiently far away, so the focusing lens was initially placed approximately 1.5 m upstream from the chamber axis at the target region. However, the high power densities on the lower "Brewster angled" window (BW_2) was regularly impairing the window. The thin lens equation was used to calculate the focal point. Without accounting for the natural divergence and the source distance, the focal point was ∼ 12 cm below the midplane. The lens was moved 12 cm upstream (i.e., 1.62 m from the midplane) from the chamber axis for the first pass.

Similarly, for the second pass, the laser beam focus was ∼14 cm above the midplane; again, the focusing lens was placed 1.64 m upstream from the machine axis. After rectifying the lens position, the air breakdown occurred at the machine axis at both locations vented to the atmosphere, (see Figure 4.3). Additional complications have surfaced with the upgrade of the second pass. During plasma operation, the movement of the laser beam on the second pass was observed when the magnetic field is applied in Proto-MPEX. The movement of the laser beam was causing it to misalign with the collection fiber optics bundle. Any small movement in the laser beam anywhere upstream could also have been severely exaggerated during the second pass; therefore making the probability of maintaining the laser alignment for the second pass even smaller. The process to identify the cause of the movement is still in progress, but presently the Rayleigh scattering calibration with nitrogen is conducted in the presence of the magnetic field to account for any movement that may be present during plasma discharges.

The noise on the signal arriving at the collection optics from the laser stray-light and the plasma background is always a challenge with a Thomson Scattering diagnostic. In order to reduce the optical noise, a significant portion of the vacuum chamber and the laser flight tubes have been covered with Acktar Spectral Black foil at both the central chamber and the target region (Figure 4.5). Similarly, reflecting surfaces at the central chamber, which are used for microwave injection are anodized with a black coating. The laser dump is placed at ∼40° — 50° angle to minimize the light reflection into the flight tube. An iris with an adjustable aperture (A_5, see Figure 4.4), is placed in front of the laser dump to minimize the scattered light back into the laser flight tube.

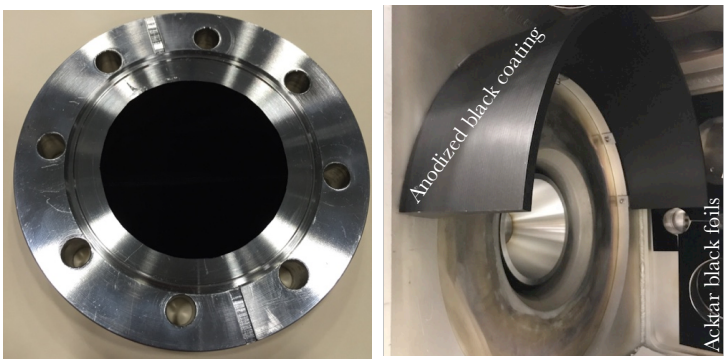

Figure 4.5: The conflat vacuum flange covered with Acktar Spectral Black (left), and the microwave reflecting surface anodized with black coating (right) to minimize light reflection.

Moreover, the ICCD camera is triggered twice, during and 20 ms after the laser pulse, using a Stanford Research Systems pulse generator to subtract the nuisance emissions and bremsstrahlung. With this technique, plasma background light and the stray light can be measured separately from the Thomson scattering signal. Typically, an ensemble of 5-10 discharges is required to obtain a reliable electron temperature and density profile. Moreover, to improve the statistics, and to remove the noise 2× or 4× pixel binning in the wavelength axis of the ICCD camera has been implemented. The pixel binning reduces the signal-to-noise ratio and increases the ICCD readout frequency [66].

4.3 Results from double-pass TS in deuterium plasma

The increase in signal-to-noise ratio and advancement in machine performance has vastly improved the Thomson scattering diagnostics in Proto-MPEX. The number of shots required for an ensemble has been reduced from ~ 40 shots to ~ 10 in high electron density ($2-5\times10^{19}$ m^{-3}) deuterium discharges. The spectrometer background is about 1300 counts. However, using the double triggering technique, the plasma background count for the 100 ns gated width was observed to have a minuscule contribution to the optical noise when compared to the instrumentation noise and the laser stray-light. Moreover, from the Rayleigh scattering calibration, the stray-light limited lowest measurable density was calculated to be 1.5×10^{18} m—3. Figure 4.6 shows a fit to Thomson scattering data obtained from a fiber at r = -1.5 cm from the target region. In Figure 4.6a, the blue dots represent the fitted Thomson photon counts, and the red line factors the Gaussian fit. The stray light count still dominates the collected Thomson scattering photons. Therefore, the center of the laser light near the laser wavelength (532 nm) is masked during the Gaussian fitting process, where the open circles in show excluded data around 532 nm. Figure 4.6a shows the residuals to the fit, where the open circles are again the excluded data.

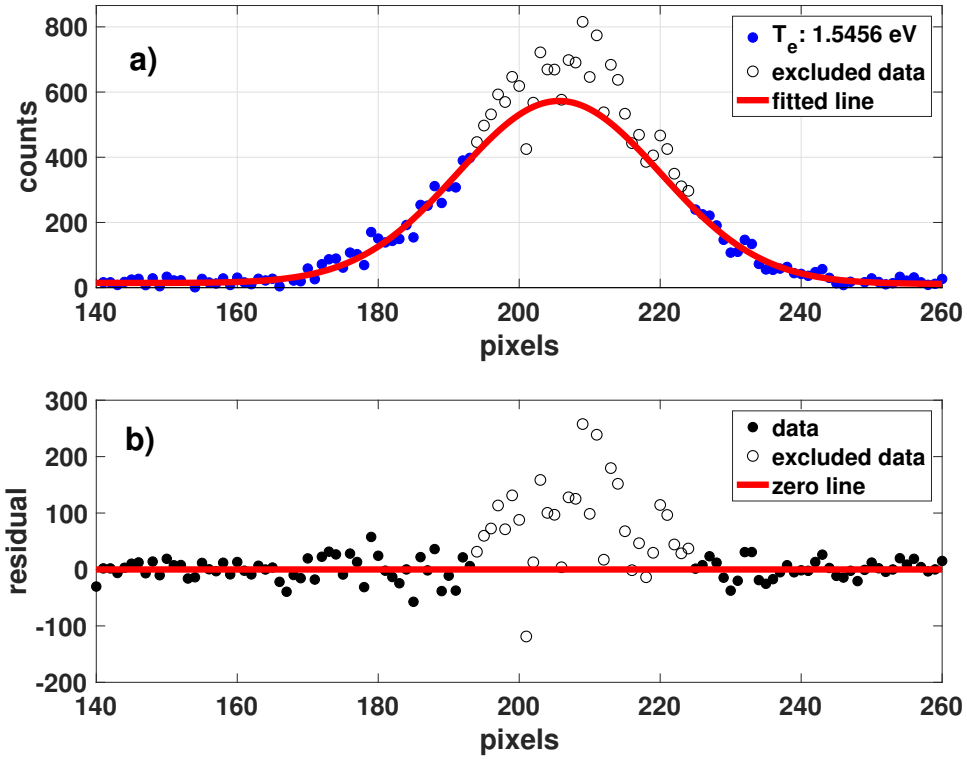

Figure 4.6: A fit to the Thomson scattering data from a fiber at the target region is shown. In a) blue dots are the scattered photon counts, open circles are the excluded data around the 532 nm, and the red line is the Gaussian fit to the data. In b) black dots are the residual from fitted data, open circles are the excluded data, and the red line is the zero reference line.

Proto-MPEX has successfully produced high densities plasma with light ions. Results shown here are experiments conducted with deuterium discharges when the magnetic fields were set to ~ 0.7 T on the main coil, and ~ 0.03 T around the helicon plasma source. Seventeen sampling point at the central chamber and three sampling points at the target region have been used for the presented results. TS ensemble provided an on-axis n_e of $2.05 \pm 0.26 \times 10^{19}\ m^{-3}$ and T_e of $3.96 \pm 1.31\ eV$ at the central chamber, and n_e $1.23 \pm .17 \times 10^{19}\ m^{-3}$ and T_e of $1.16 \pm 0.17\ eV$ at the target region. The radial T_e and n_e profiles obtained simultaneously in the central chamber and the target region are shown in Figures 4.7a and 4.7b, respectively. It should be noted that the radius (R) shown in the radial profiles is local to the measurement locations [71].

Using the 95% confidence interval from each coefficient in the Gaussian fit, error is propagated to obtain relative error of the measured T_e and n_e. The estimated TS systematic uncertainty is $\sim 10\%$. These uncertainties are propagated with the photons and fitting errors, as shown here. Near the edge of the plasma, the TS scattered counts are negligible, which constitutes for the large error bars in the radial profile obtained at the central chamber. As seen in Figure 4.4, some of the optical fibers at the central chamber lie above the plasma column [71].

4.4 Near target measurements using Thomson scattering

A movable target translation stage was installed to axially translate the target plate relative to the center spool 11.5. The target plate could be moved 0 to 8 cm away from the center of spool 11.5. Figure 4.8a shows the image of the translation stage, where one could install various material target plate. The capability of moving the target towards the diagnostics gives the ability to study the plasma characteristics near the target plate.

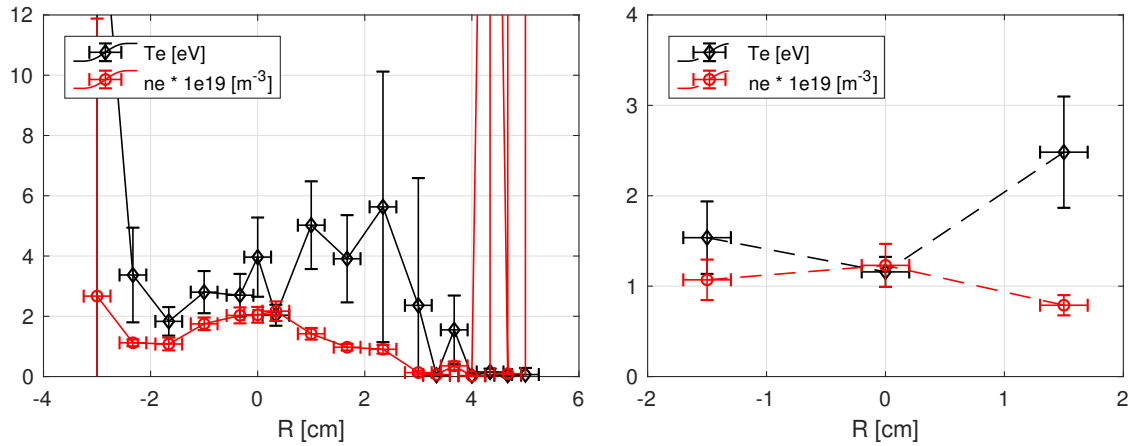

(a) Central chamber **(b)** Target region

Figure 4.7: TS Radial profiles of the electron temperature and density measured in (a) the central chamber, and (b) in the target region.

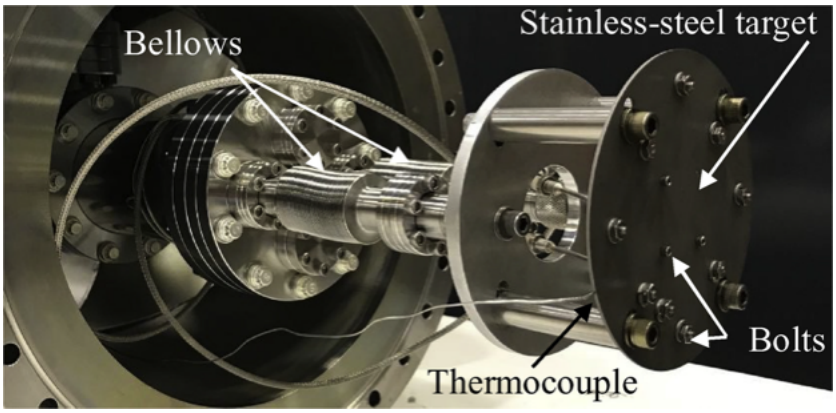

(a) Movable target station

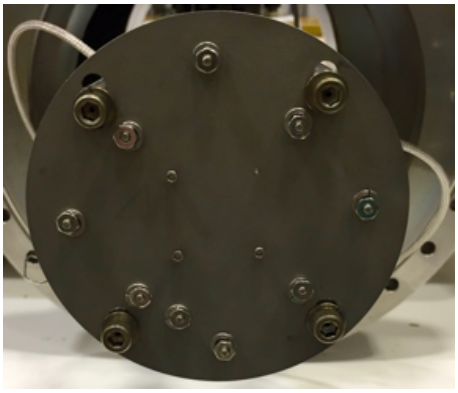

(b) Target Front View

Figure 4.8: (a) An axially translating target system with respect to the target spool-piece. As shown a stainless steel target is attached to the bellows of the translating system. A thermocouple is attached to the back of the target surface. Bolts seen on the front side of the target surface was used to hold a target heater. (b) Front view of the target plate.

Results from these experiments show that understanding the region (∼2 cm) in front of the target is crucial in determining the different regimes in Proto-MPEX. One solution considered to improve the stray light has been to replace the target plate with no bolts and nuts on the front side, as shown in Figure 4.8b. Experiments with the translating stand were conducted in Configuration A. Figure 4.9 shows T_e (black) and n_e (red) as a function of the target position with respect to the center of the the target spool piece. The position of the TS laser is at the center (z = 0). The negative scale in the plot indicates the target plate moving away from the TS laser towards the ballast tank. Measurement shows T_e fluctuating between 2 and 3 eV when scanned from from -4 to -1.25 cm, but in general a relatively flat profile was observed, and in contrast, n_e decreases from -4 to -2 cm, but increases to 4×10^{19} from -2 to -1.25 cm. Obtaining a reasonable measurement within 1.25 cm of the target was not possible because the laser stray-light was overwhelming the collection optics. Results shown here could not conclusively determine the plasma transport behavior closer to the target. A different technique might be needed in the future to study the near target phenomenon in greater detail. Schlieren imaging systems are being studied as an alternative technique to quantify near target measurement [72].

4.5 Summary

The work presented in this chapter discusses the major upgrade of the Thomson scattering diagnostic from a single pass system near the target region to a double pass system, which adds a new measurement location at the central chamber in Proto-MPEX. The Thomson scattering upgrade gives confidence in the measurement of the plasma parameters at multiple locations in Proto-MPEX. Furthermore, an improvement of the signal-to-noise ratio has increased the

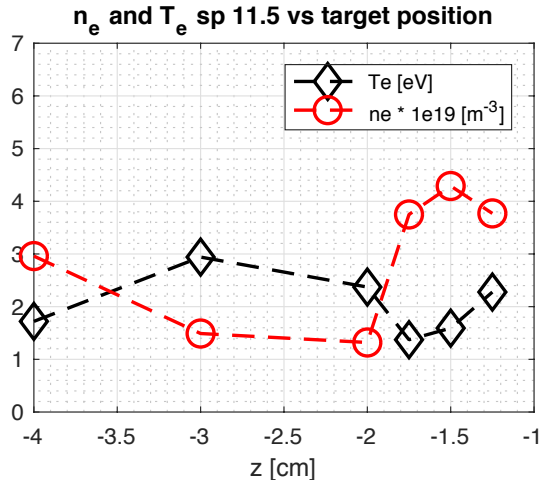

Figure 4.9: Figure shows T_e and n_e as a function of target position relative to the TS laser. z = 0 cm is the position of the TS laser, and the negative scale represents distance further way from the center of the TS laser position. A scan of the target position is taken 1 to 4 cm away from the target.

efficiency of the diagnostic system. The simultaneous measurement of electron temperature and density can now be used for reliable measurement of the axial plasma gradients in Proto-MPEX.

The stray light from the laser beam still needs further optimization. In some experiments, moving the target plate closer to the Thomson scattering laser beam saturated the detector with excessive stray-light as it exceeded its dynamic range; thus, making it tough to quantify near target parameters. Also, the added travel length from the Configuration B upgrade has contributed to the misalignment at the second pass. A small motion and the vibration of one of the mirrors during plasma discharges could be causing the laser beam to drift away from the intended position. It may be contributing to the misalignment of the laser as to the collection optics. This study was also useful in identifying a need for decoupling the optical components attached to Proto-MPEX, and an addition of an active laser beam stabilizing unit to improve the system performance.

Chapter 5

Helicon plasma transport in Proto-MPEX and comparison with B2.5-Eirene modeling

Reproduced from N. Kafle, L. Owen, J. F. Caneses, T. M. Biewer, J. B. O. Caughman, D. C. Donovan, R. H. Goulding, and J. Rapp, "Plasma flow measurements in the Prototype-Material Plasma Exposure eXperiment (Proto-MPEX) and comparison with B2.5-Eirene modeling," Phys. Plasmas, vol. 25, no. 5, 2018, with the permission of AIP Publishing.

N. Kafle contribution is with the experimental design; most of the data collection and data analysis, literature review, and writing the paper. **L. Owen** conducted B2.5-Eirene modeling. **D.C. Donovan** advised on the experimental design, helped to define the problem statement. **J. Caneses** and **R.H. Goulding** helped with the experimental design, data analysis, and operating Proto-MPEX, **T.M. Biewer** oversees the development of many of the diagnostic systems used to make measurements reported in this paper, **J.B.O. Caughman** oversees modification and operation of the Proto-MPEX, and also helped running experiments and guide the research. **J. Rapp** is leading the R&D effort on Proto-MPEX for the MPEX project.

5.1 Introduction

Experiments have been conducted to study the helicon plasma flow (without auxiliary heating) from the source to the target plates in Proto-MPEX and compared with B2.5-Eirene modeling. Comparisons between experimental results and the modeling for the axial flow have been encouraging. This chapter will discuss the results from the B2.5-Eirene modeling and the experiment.

Transport studies are important in linear plasma devices to understand the plasma reaching the target and optimizing the heat and particle fluxes to the target. Plasma traversing the axial length of the column undergoes radial diffusion, plasma-neutral interactions, and ion-electron interactions. Several modeling efforts using B2.5-Eirene have been conducted to understand the particle transport in linear devices [73, 74, 75, 38]. Linear plasma devices with their relatively simple geometry and good diagnostic access facilitate direct comparison of experimental measurements with modeling and simulations. Comparisons between experiments and B2.5-Eirene modeling have been conducted in Proto-MPEX [76], PSI-1 [77] and Pilot-PSI [78]. In a prior study in Ref. [76] on Proto-MPEX, a data constrained radial transport comparison with the B2.5-Eirene was made, along with some predictions on axial plasma transport. In the study presented in this chapter, data-constrained analyses of plasma transport in helicon discharges in Proto-MPEX has been performed in order to obtain predictive calculations of axial electron temperature and density from the modeling. The interpretive and predictive modeling capability of B2.5-Eirene is necessary for design activities towards MPEX. This chapter reports plasma flow measurement conducted in Proto-MPEX, as well as results from axial plasma transport, benchmarking the B2.5-Eirene code against the experiment. The experiment and the modeling setup is presented in 5.2 and 5.3, respectively. The comparison between experimental and modeling results is given in 5.4.

5.2 B2.5-Eirene

The B2.5-Eirene [79, 80, 81] code was developed to solve the parallel and perpendicular transport of plasmas along the field line in which the field lines intersect a target or a wall [82]. B2.5 solves coupled conservation equations for parallel momentum, density for each charge state, and each electron and ion energy. The 3-D kinetic Monte Carlo code Eirene is used to solve the transport of neutral species. The radial transport, in Proto-MPEX model, is assumed to be diffusive across magnetic field lines, and is described typically with anomalous values of particle diffusivity (D) = 0.5 m^2/s, which is within the range (0.23 - 0.74 m^2/s) of measured value in Pilot-PSI [83], and thermal diffusivities (χ_i and χ_e)=1.0 m^2/s . A field-aligned grid is used in the B2.5-Eirene transport simulations. The transport model has not been coupled to a heating code in Proto-MPEX simulations. In Figure 5.1, the assumed volumetric heating power density from helicon wave heating is shown on the physical grid. The assumed volumetric heating power density in Fig. 2 is based on the assumption that plasma production and heating via helicon waves are localized near and under the helicon antenna. T_e measurements and full-wave electron heating calculations suggest that this is a reasonable assumption. Recycling coefficients characterize pumping surfaces in the model.

The following set of boundary conditions are prescribed for the modeling. The radial particle and energy-momentum flux are set to zero on the axis, at the outermost field line density. The temperature decay length is 1 cm, and the density decay length is 0.5 cm, which are assumed

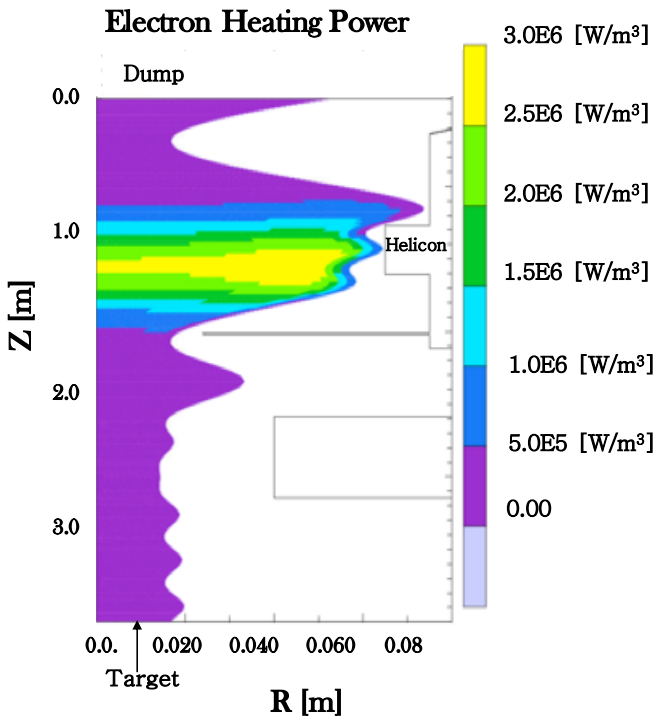

Figure 5.1: Contour plot of the assumed electron heating distribution [W/m^3] from the helicon wave.

to be constant along the outer boundary of the B2.5-Eirene grid. The density and temperature boundary conditions at the axis are $dn/dr = (dT_e)/dr = (dT_i)/dr = 0$. Bohm conditions, where the plasma flow reaches the sound speed, is assumed at both the dump and the target plates. The data constrained modeling results presented here are focused on fitting the core (near the axis) region where helicon wave heating is dominant, rather than the edge-dominant TG mode. The model uses cylindrical symmetry. Based on steady-state gas puffing experiments, recycling coefficients of 0.984 and 0.80 were assigned to dump and target plate annuli, respectively [76].

5.3 Experimental measurements

An extensive array of diagnostics coverage was implemented to obtain the axial parameters in Proto-MPEX. Figure 5.2 shows the 2D cross-section of Proto-MPEX along with its key components. This figure is described in detail in Chapter 2. Proto-MPEX was in Configuration A during this experiment, with one key difference. A mass flow controller (MFC) was fueling the neutral deuterium gas instead of a piezo gas valve. Deuterium gas (D_2) was puffed at 0.2 m downstream from the helicon source in two stages (Figure 2.4a). The use of piezo puffer was later identified to be an efficient method to fuel the gas by increasing precision and reducing

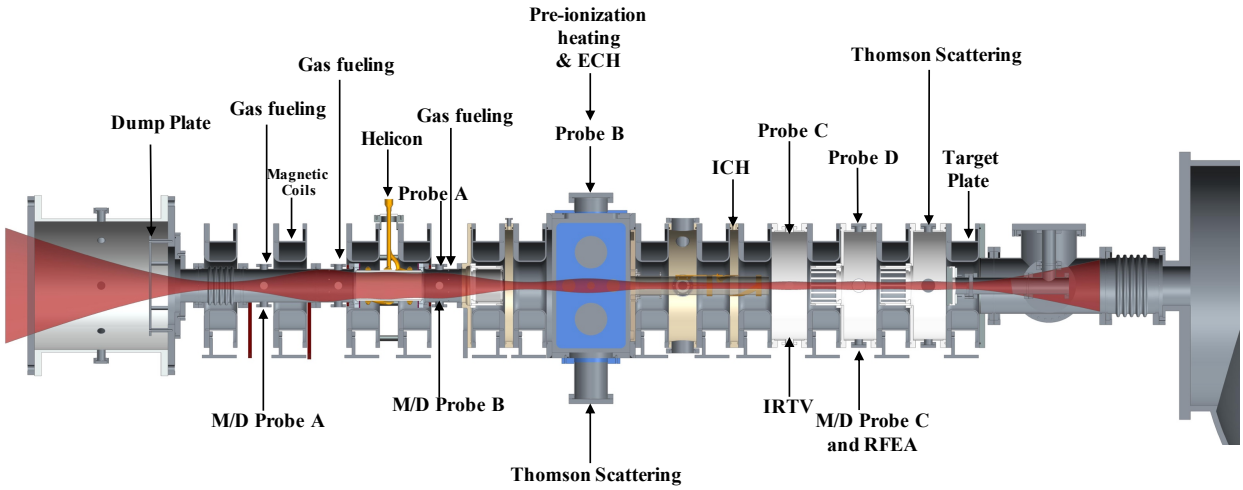

Figure 5.2: A cross-sectional schematic of Proto-MPEX in Configuration A, showing the helicon antenna along with auxiliary heating sources, and critical diagnostics locations

the residual gas downstream towards the heating locations, which also improved the heating efficiency.

Radial probe scans were taken to obtain T_e and n_e profiles using Probe B through D (Figure 5.2), along with TS during high-density helicon RF discharges. Radial T_e and n_e distributions from different probes and Thomson scattering measurements are shown in Figure 5.3. Large T_e of 10 to 12 eV measured by Probe B are near the edge of the plasma column where n_e is in the order of $1 \times 10^{18} m^{-3}$. The high T_e could be due to the presence of the TG mode at the edge plasma [37]. B2.5-Eirene simulations are focused on fitting the near-axis measurements of n_e, T_e and M in high density helicon discharges, so such edge plasma with large T_e and small n_e are excluded from the modeling. Flatter T_e and peaked n_e profiles show that helicon wave heating in the core is achieved when compared to the previous study in Proto-MPEX [76]. The asymmetries in the measured profiles could be due to the probe misalignment of Probes C and D relative to the plasma core. Moreover, Proto-MPEX does not have a faraday shield around the helicon antenna, so a slight asymmetry in plasma profile is caused by capacitive coupling [37, 84].

5.4 Axial comparison between experiment and B2.5-Eirene modelling

T_e, n_e and M measured at various axial locations permitted data-constrained B2.5-Eirene modeling of the entire plasma column. Conservation of parallel momentum was applied in the B2.5-Eirene model in Proto-MPEX device. The electron plasma pressure (p_e) peaks near the axial vicinity of the helicon source, creating a pressure gradient on either side of the source. Figure 5.4 shows the axial p_e profile comparison between the B2.5-Eirene modeling and the experiment

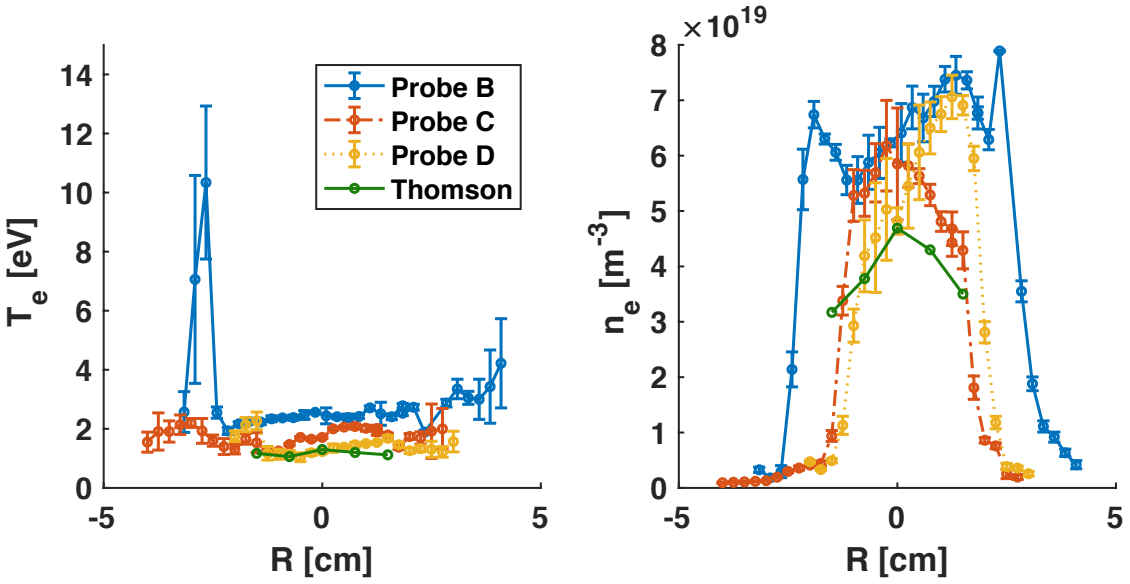

Figure 5.3: The figure presents radial T_e (left) and n_e (right) profiles from the central chamber to near target measured using DLPs (Probes B-D) and Thomson scattering. The radial T_e profile is relatively flat at different axial locations, except at Probe B where T_e at the edge peaks to 10-12 eV. Probe B measured radial profile at the central chamber, and Probes C and D took the radial measurement 60 cm and 90 cm downstream from the central chamber, respectively. The Thomson scattering measured T_e and n_e ~10 cm in front of the target plate.

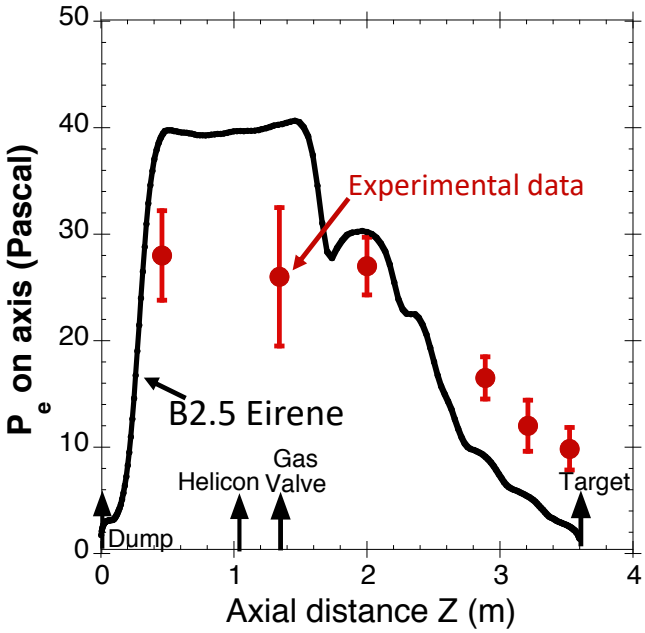

Figure 5.4: Axial plasma pressure (p_e) profile along Proto-MPEX. Comparison between measured (red dots) and modeled plasma pressure (solid curve) from B2.5 Eirene is shown. Higher pressure is observed near the source than near the target.

are in reasonable qualitative agreement. The plasma pressure is observed to be peaking near the plasma source and decreasing toward the target plate from the experiment. RF power deposition is not uniform near the helicon antenna, which causes electron heating and thermalized plasma production near the helicon antenna and causing non-uniform plasma pressure along the axis of the device [85]. The plasma pressure gradient is the driving force of the plasma from the source toward the target along the field lines. The experiment and B2.5-Eirene show a similar trend, but the model over-predicts p_e near the source region and under predicts p_e towards the target. Since static p_e is the product of T_e and n_e it will be interesting to compare axial T_e and n_e from the experiment and the modeling, separately.

An axial comparison between measured T_e and n_e (red dots) and the B2.5-Eirene simulation (solid curve) is shown in Figure 5.5. The axial T_e (Figure 5.5 left) and n_e (Figure 5.5 right) profiles from the modeling follow a similar trend as seen in the experiment; though some quantitative inconsistency between them is observed. Electron-neutral collisions most likely cause the axial decrease in T_e away from the helicon source. Electron-ion equipartition also causes T_e to decrease further until it reaches to about 1 eV where volumetric recombination could begin to dominate. From B2.5-Eirene T_e was higher than the measured value near the source region, and by contrast n_e was lower, particularly toward the dump end, suggesting that recycling may be stronger than assumed in this region. Since the power density assumed in the modeling is based only on approximations of what the real distribution may look like, the discrepancy between the measurements and the B2.5-Eirene simulations could be due to the lack of a self-consistent

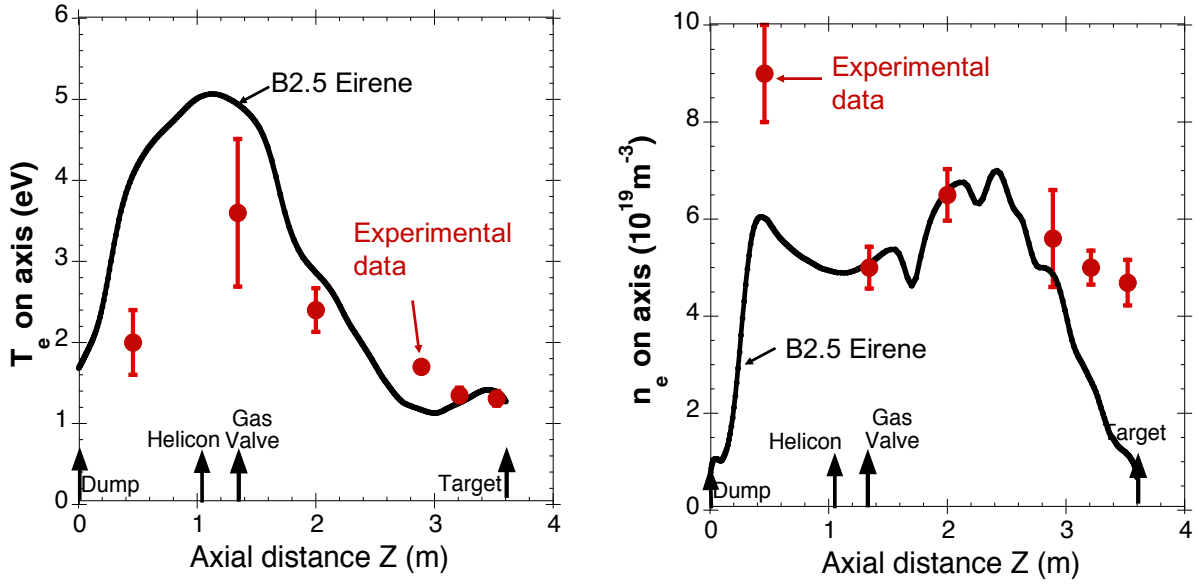

Figure 5.5: (left) shows the axial T_e profiles and (right) shows the axial n_e profiles from experiment (red dots) and B2.5-Eirene model (solid curve). Plasma at the source has higher T_e which decreases downstream from the source

description of the plasma and input power deposition profile. A full-wave code linking the RF power deposition to the fluid plasma code B2.5 is planned but not yet available.

Measurements using Mach probes at M/D Probe A through M/D Probe D shows stagnation in the region where the plasma pressure is peaked, while the flow increases in the ∇p_e region. Differential plasma pressure and the magnetic field variation is driving the plasma flow towards the target. Comparison between the Mach probe data and the modeling in Figure 5.6 shows good agreement in the stagnation region near the source; however, some disagreement arises for Mach probe data near the target in the high magnetic field. The overestimated Mach number from the experimental measurement is likely due to the short connection length between the downstream current collecting tip and the target plate [86, 87]. If the probe is too close to the target, it may reduce the amount of plasma that can diffuse and replenish the flux tube of the shadowed probe tip. At this point, the parallel particle loss to the current collecting surface exceeds the cross-field particle source and reduces the plasma density in the flux tube, which causes a reduction in the ion saturation current of the downstream tip and effectively overestimates the plasma flow. The effect gets exacerbated in high magnetic fields due to the reduction in cross-field transport. Observations in Proto-MPEX with the fast-visible camera located at Probe D location provide evidence of probe shadowing being present in the visible light emission (Figure 5.7). An alternative method to measure the plasma flow is to measure the Doppler shift of Ar II emission of argon seeded deuterium plasmas. The spectroscopic technique, however, is a line-integrated measurement and requires the use of impurities but eliminates the short connection length effect associated with the Mach probe.

Figure 5.8 compares the radial Mach number profile from the experiment to B2.5 Eirene at z = 0.45m (between coils 1 and 2). The radial asymmetry in the plasma profile is also apparent in the figure due to the reason discussed above. In addition, the figure shows the Mach number from B2.5 Eirene at z = 0.36 m (9 cm from the axial location of the measurement), which is in better agreement with the experimental results. The Mach probe (M/D Probe A) at z = 0.45 m shows a Mach number of -0.5, but B2.5-Eirene model shows the Mach number to be approximately -0.2 at that location. The discrepancy in the measured Mach number compared to that predicted using B2.5-Eirene could be due to the presence of a steep gradient in the Mach number (Figure 5.6) and shows that a small uncertainly in the axial location of the Mach probe will vastly differ from the measured Mach number.

5.5 Summary

First plasma flow measurements were performed using Mach probes on high density deuterium plasmas discharges in Proto-MPEX with helicon RF source. The flow is stagnant near the helicon source and flows away towards the target due to axial plasma pressure gradients. However, experimentally measured flow using Mach probe is observed to be faster in a high magnetic field with short connection length when compared to the predicted result from B2.5-Eirene

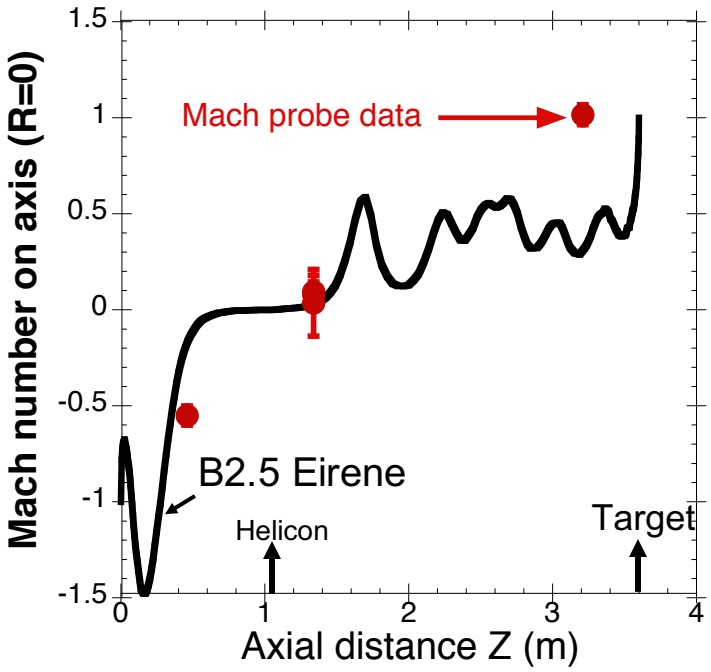

Figure 5.6: Axial Mach number along Proto-MPEX. Mach number compared between the experiment (red dots) and modeling (solid curves). Stagnation region observed near the source and increased Mach number near the targets at both ends.

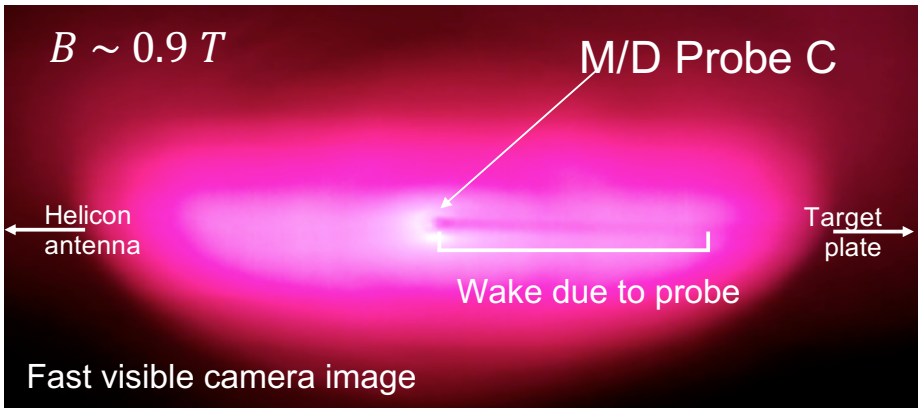

Figure 5.7: Probe shadowing in the visible light emission observed by the fast-visible camera at M/D probe C location.

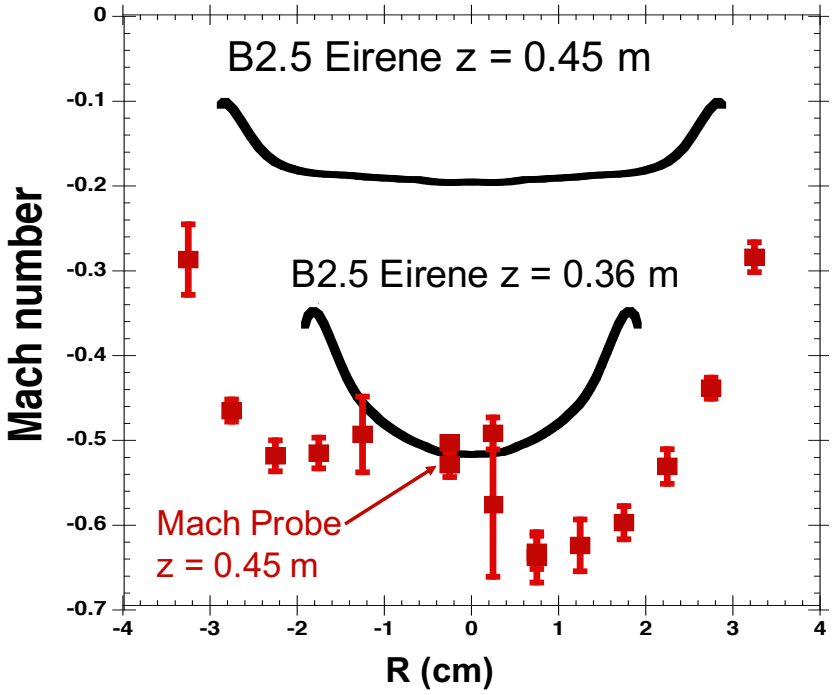

Figure 5.8: Radial Mach number at z = 0.45 m from Mach probe, M/D Probe A (red dots) is compared to B2.5-Eirene model (solid curves). From modeling, radial flow profile at z = 0.36 m (closer to the dump plate) is in better agreement with the experimental data.

modeling. The measurements of T_e, n_e and M were also compared to fluid plasma/kinetic neutrals simulations by B2.5-Eirene. Simulations show qualitative agreement to the experimental data measured axially along Proto-MPEX and suggest that helicon-only produced plasma can be described by a plasma fluid model, with transport coefficients in the range of 0.5 m^2/s, coupled to Monte Carlo neutrals. The agreement between theory and experiment is best at locations away from the target and dump plates where the recycling regions maybe least. Accurately modeling high recycling scenarios require a computationally intensive iteration process. Recycling conditions will be investigated in more detail as additional diagnostic data for varied operating conditions becomes available.

The findings presented here show that plasma generated in the helicon region is transported out axially towards both the target and dump plate. As the plasma streams away from the source, electron-neutral collisions lead to a reduction in the electron temperature. Independent ion and electron heating will be required to increase the plasma temperature and thereby the heat flux at the target in Proto-MPEX. Proper management of the neutral pressure in the downstream device is necessary to maintain high T_e near the target region. Various gas puffing rates (to increase the helicon density production) and skimmers for neutral gas management may be necessary for steady-state operation at the high particle fluxes expected in MPEX.

Chapter 6

Experimental investigation of plasma transport with auxiliary heating

In chapter 5, the data constrained B2.5-Eirene model from the helicon-only source predicts that the plasma in Proto-MPEX has high static plasma pressure in the source region and that the pressure gradient is driving the plasma towards the end plates where the static pressure is lower than at the source. Further analysis of heat conduction and heat convection from the B2.5-Eirene model shows that the plasma in the source region is conduction dominated and that the plasma transport in the target region is convection dominated. To be useful as a divertor simulator, MPEX needs auxiliary power to increase heat and particle fluxes. Therefore, it is essential to understand plasma transport (to the target region) with the addition of supplemental heating systems (ECH/EBW and ICH) in Proto-MPEX. The additional energy from ECH/EBW will result in a population of energetic particles, which tend to be trapped in the mirror wells in Proto-MPEX. The mirror trapping phenomenon may limit the plasma transport of energetic particles to the target and is a crucial topic to quantify. In order to understand the transport of the EBW heated particles, it is important to study the influence of magnetic mirrors in desired operating conditions. A comparison between Configuration A and B can be made with the addition of EBW. As described in 2.3, Configuration A is an older Proto-MPEX geometry where the 28 GHz launcher was present at the central chamber, and Configuration B is the upgrade configuration where the 28 GHz launcher is moved downstream of the central chamber.

This chapter focuses on identifying the transport phenomenon in Proto-MPEX, which includes stating assumptions for a model that could describe and relate transport in Proto-MPEX to the SOL transport in a tokamak. After establishing the model, experimental investigations are analyzed for plasma discharges with and without auxiliary (28 GHz – EBW) heating in Configurations A and B. This chapter also identifies the dominating heat flux pattern in both configurations, and the influence of overhill and downhill B-fields on the heat transport. The motivation for overhill and downhill magnetic field conditions emerges to evaluate the efficiency of the energized particles transporting heat to the target plate. The overhill condition is also

conducive for the ICH power coupling for ion heating, but due to the presence of a small magnetic hill between the 28 GHz launcher and the target, the presence of the mirror might still trap some of the energized particles. This dissertation does not focus on studying the efficiency of ICH heating.

6.1 Transport model as divertor SOL in Proto-MPEX

The power in tokamaks is exhausted at a robust material target, which can withstand the harsh plasma condition. Two major types of surfaces considered for the termination of the edge plasma in toroidal devices have been limiters and divertors. Several advantages, such as a lower power density, increased component lifetime, and reduced impurities transport to the main plasma has made the divertor a more practical option than limiter designs [26]. As mentioned in chapter 2, the transport study in Proto-MPEX is motivated by the analogy of the straightened out tokamak scrape-off-layer (SOL). Stangeby, in Ref. [26], goes into a detailed analysis of the SOL in tokamaks, starting with the simple analytical model of the SOL, then adding complexities to it. The goal of the work presented is to model an understanding of the plasma transport behavior in Proto-MPEX compared to the edge transport in a toroidal device. The near divertor plate transport phenomenon in a tokamak has been described primarily using two types of models: 1) a sheath-limited regime (SLR), and 2) a conduction-limited regime (CLR). In an attempt to quantify the transport behavior in Proto-MPEX, this section uses simple SOL assumptions and the criteria from the two-point model to identify the regimes in Proto-MPEX.

6.1.1 Simple SOL heuristic model

An analogy between different regions of Proto-MPEX described in chapter 2 and a divertor SOL flux surface in a tokamak can be made. The transport comparison between Proto-MPEX and a tokamak can be made using a series of steps. In a divertor, particles are transported radially outwards from the main plasma towards the SOL surface. As shown in Figure 6.1a, particle entering the SOL near the outer midplane are transported poloidally, splitting into two directions. There is a dominating particle transport direction depending on where they enter into the SOL, i.e., particles entering above the outer midplane move towards the inner divertor and particles entering below the midplane migrate towards the outer divertor [88, 89]. In this analogy, the particle source is the helicon antenna, which then leaves the source region in two different directions (towards the dump plate and the target plate), as shown in Figure 6.1b. Similarly, heat from the main plasma is transported radially outward into the SOL surface of a tokamak, as shown in Figure 6.1c. In Proto-MPEX, particles are energizied using auxiliary heating systems (ECH/EBW and ICH), as shown in Figure 6.1d. Combined pictures for a tokamak and Proto-MPEX are shown in Figures 6.1e and 6.1f. In Proto-MPEX the particle source and the heat source can be controlled independently, which provides added capability of utilizing the linear device to

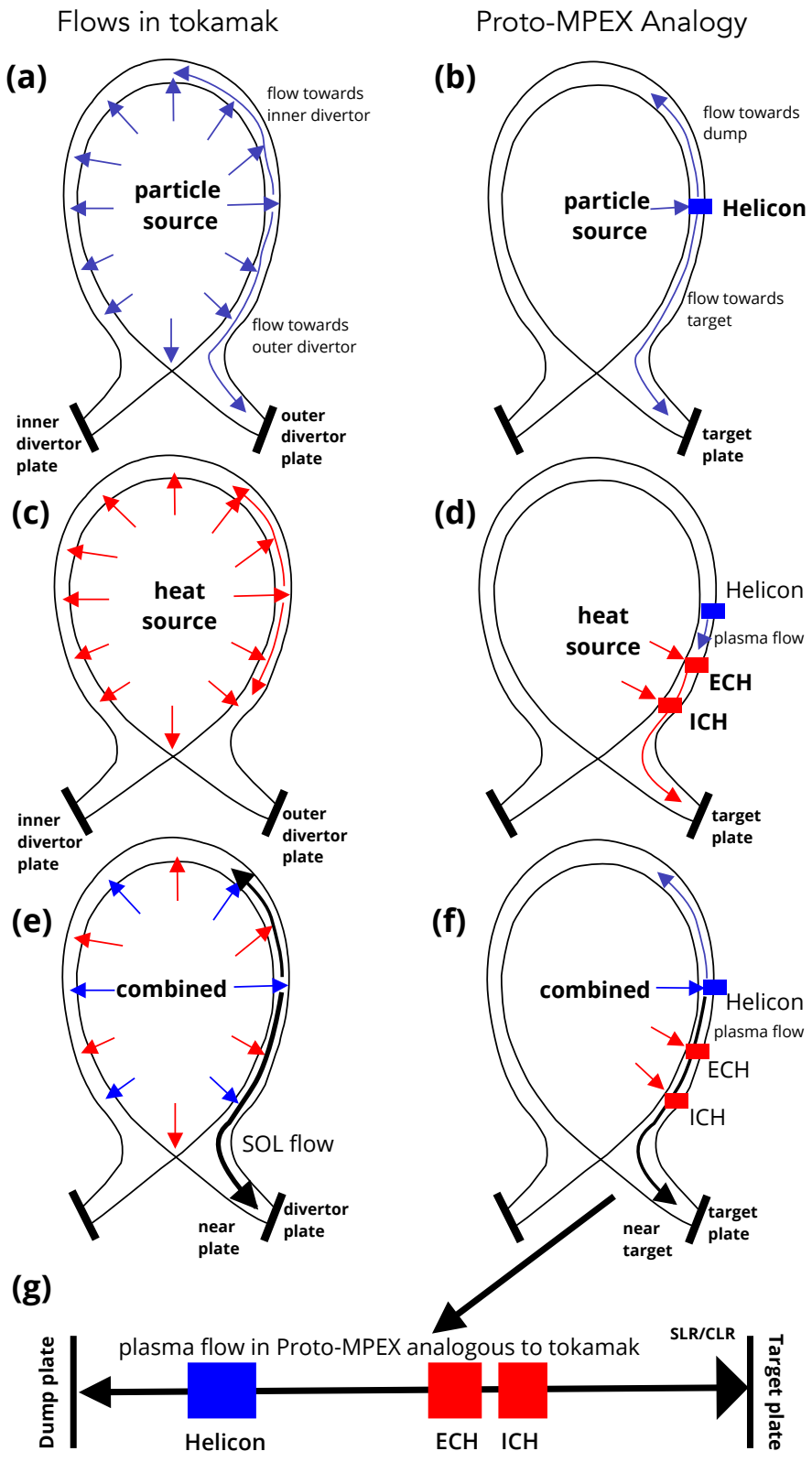

Figure 6.1: Different regions of Proto-MPEX illustrated in relation to a divertor SOL.

access different regimes as desired. Analogous to a 'straightened-out' image of a divertor SOL, the plasma transport is depicted in Figure 6.1g.

The plasma transport in tokamaks has been described using two different types of scrape-off layer characteristics: 1) Simple SOL and 2) Complex SOL. A simple SOL typically includes the properties of a sheath-limited regime, and a complex SOL contains the features of a conduction-limited regime. Descriptions of the sheath and conduction-limited regimes are as follows:

1. **Sheath-limited regime, SLR**
   In the sheath-limited regime (SLR), the plasma is approximately isothermal along each magnetic flux tube. The particle source in SLR is generally cross-field transport from the main plasma, and volumetric sources and sinks of particles, momentum, and energy in the SOL do not exist [26].

2. **Conduction-limited regime, CLR**
   Contrary to the sheath-limited regime, the conduction-limited regime has a significant parallel temperature gradient. Ionization and volumetric sources and sinks within the SOL can occur. As a subcategory, for the conduction-limited regime with high electron density production near the target is called the high recycling regime (HRR) [26].

Starting with the basic model of a simple SOL, and being conscious of the differences between of the axial profile of Proto-MPEX and the tokamak SOL, for helicon discharges the transport region taken into consideration is downstream from the helicon antenna to near target. Similarly, for helicon with 28 GHz discharges transport region is downstream from the heating section to near target; this is because power coupling from 28 GHz system causes a local rise in core T_e measured near the heating section. Moreover, the power coupling is directed towards the target and does not significantly alter upstream T_e; therefore, it is appropriate to only consider transport behavior between the heating and the target regions.

A simple two-point model could provide a further understanding to distinguish between a sheath-limited and conduction-limited regime. The model also provide some information on the boundary between the regimes in Proto-MPEX. Stangeby, in Ref. [26] presents rigorous analysis to connect the upstream and downstream parameters in a tokamak. The basic two-point model equations derived by Stangeby are shown in Eq. (6.1),

$$\begin{aligned} n_u T_u &= 2 n_t T_t, \\ T_u^{7/2} &= T_t^{7/2} + \frac{7}{2}\frac{q_\parallel L}{\kappa_{0e}}, \\ q_\parallel &= \gamma e n_t T_t c_{s,t}, \end{aligned} \tag{6.1}$$

where n_u and n_t are electron densities and T_u and T_t are electron temperatures at the upstream and target locations, respectively. $q_\parallel$ is the parallel heat flux, κ_{0e} is obtained from Spitzer's

formula for electron heat conductivity, where $\kappa_0 = 2000$ for electrons, and L is the flux tube length. In those three equations T_u, T_t, and n_t are the dependent variables and $n_u, q_{\|}$, and L are the control variables. In the two-point model, heat conduction dominates the heat transport in the SOL, and the total pressure along the flux tube is constant. The model relates the upstream and target parameters, and there are two factors useful to evaluate differences between the sheath-limited and conduction-limited regime. The first criterion would be to identify the change in the temperature from the upstream vs. the target is given by,

$$f_T = \frac{T_u}{T_t}, \tag{6.2}$$

The second criterion is using the plasma collisionality (ν^*), which is given by

$$\nu^* = \frac{L}{\lambda}, \tag{6.3}$$

where λ [m], is the collisional mean free path given by,

$$\lambda_{ee} \approx \frac{10^{16} \mathrm{T_e^2}}{\mathrm{n_e}} \tag{6.4}$$

for T in eV, and $\mathrm{n_e}$ in $\mathrm{m^{-3}}$. Where classically, $f_T > 3$ is recognized as high temperature gradient and $f_T < 1.5$ is a low temperature gradient [26]. When the plasma gradient is small and the collisionality, $\nu^* < 10$, a sheath-limited regime is obtained. When the gradient is large and the collisionality, $\nu^* > 15$ then the plasma could be considered to be in the conduction-limited regime.

From the experimental results shown in Chapter 5, the typical n_e and T_e measured in Proto-MPEX are 4×10^{19} [$\mathrm{m^{-3}}$], and 4 eV, respectively, which gives λ_{ee} of ≈ 0.40 cm (Eq. 6.4), and ν^* for ~ 2 m is 888. Moreover, $\mathrm{T_u} \sim 4$eV and $\mathrm{T_t} \sim 1.5$eV gives $f_T \approx 2.6$. From both criteria from the basic two-point model, the helicon plasma is highly collisional and yet has a small gradient. From this analysis, one cannot readily identify the transport regime; therefore, further analysis or a modified model is needed to identify the transport regime for the helicon discharges. Proto-MPEX properties deviate from the basic two-point model, which was built solely for the scrape-off-layer of toroidal geometry. Some of the plasma transport properties exhibited in Proto-MPEX are:

1. Plasma in Proto-MPEX is 'quasi-isothermal' (with small axial plasma gradient). The $\mathrm{T_e}$ drops in the transport regions to 1—2 eV.
2. Conductive transport of plasma is limited near the helicon region, and negligible near the transport region
3. The neutral density in the transport region (i.e. away from the source) is small

4. The velocity of the plasma increases away from the source, which makes it convection dominated plasma, which enables larger heat convection towards the target.

5. Using the basic two point model with corrections could be better approach in defining transport regime in Proto-MPEX.

A rigorous model for the transport regime in Proto-MPEX will be required as a future study. However, when the parallel heat convection dominates the parallel heat transport, the plasma will exhibit an isothermal axial profile. This is valid for the helicon plasma discussed in 6.4. In configuration A, during 28 GHz power injection, the electrons are heated at the central chamber. A deep well is present there, and the perpendicular electron energy increases. The heated electrons become less collisional, and kinetic mirror effect dominates.

6.1.2 Cross-field diffusion

Most of the analysis in this chapter focuses on a single flux tube and on-axis data points, so it is essential to calculate the cross-field diffusion of particles in Proto-MPEX. The classical perpendicular cross-field diffusion using Spitzer parallel electrical resistivity ($\rho_{\parallel}^{\text{spitzer}}$) of a fully ionized plasma is given by [26],

$$\begin{aligned} D_{\perp}^{\text{classical}} &= 2\rho_{\parallel}^{\text{spitzer}} n \frac{kT_e + kT_i}{B^2} \\ \rho_{\parallel}^{\text{spitzer}} &= 8\times10^{-4}/(kT_e)^{3/2} \end{aligned} \tag{6.5}$$

Proto-MPEX is estimated to have $>75\%$ ionization fraction [31]. The cross-field diffusion in Proto-MPEX plasma is calculated using Eq. (6.5). Axial measurement of T_e and n_e along Proto-MPEX have been conducted for Configurations B. In the classical diffusion, $D_{\perp}^{\text{classical}}$ has $1/B^2$ dependence, but in tokamaks the dependence has been found to be stronger than measured values [26, 41]. A semi-empirical formula developed by Bohm (Eq. 6.6) has inverse linear relationship between $D_{\perp}^{\text{Bohm}}$ and B, i.e. $D_{\perp}^{\text{Bohm}} \propto 1/B$.

$$D_{\perp}^{\text{Bohm}} = \frac{1}{16}\frac{kT_e}{eB} \tag{6.6}$$

Using on-axis T_e and n_e at different axial locations both classical and Bohm diffusion coefficients are calculated; classical cross-field diffusion values are given in Table 6.1, and Bohm cross-field diffusion values are given in Table 6.2. Moreover, perpendicular cross-field diffusion is used to estimate a characteristic diffusion distance (λ_{diff}), which is given by Eq. (6.7),

$$\lambda_{\text{diff}} = (D_{\perp}L/c_s)^{1/2} \tag{6.7}$$

where L is the characteristic length of the device. For Proto-MPEX, using L = 4 m, $T_e = 3\ eV$, $c_s = 1.2\times10^4 \text{ms}^{-1}$, and $D_{\perp} = 0.657\text{m}^2\text{s}^{-1}$, gives λ_{diff} of 1.4 cm. However, the transport

Table 6.1: Classical perpendicular cross-field diffusion in Configuration B in overhill and downhill magnetic fields.

z [m]	$\mathbf{D_{\perp}^{classical}}$ $[m^2 s^{-1}]$	
	Overhill	**Downhill**
1.1	0.091	0.099
2.6	0.275	0.21
3.2	0.042	0.021
4.1	0.035	0.039

Table 6.2: Bohm perpendicular cross-field diffusion in Configuration B in overhill and downhill magnetic field.

z [m]	$\mathbf{D_{\perp}^{Bohm}}$ $[m^2 s^{-1}]$	
	Overhill	**Downhill**
1.1	0.657	0.542
2.6	1.5301	2.003
3.2	0.322	0.579
4.1	0.278	0.851

region between the heating and the target region, where L is approximately 1.2 m, gives $\lambda_{\text{diff}} \approx 0.5$ cm.

The IR thermography on the target plate observed a similar scale of cross-field diffusion of the plasma in Proto-MPEX. Analysis has shown that only a small cross-field diffusion exists in Proto-MPEX and probably is not quite significant for the current connection length in Proto-MPEX. However, if L is longer for future MPEX device, it may be required to take into consideration.

6.2 Compressible nature of plasma

Proto-MPEX exhibits axial variation in the B-field. Figure 6.2 shows the magnetic field variation that is present axially in Configuration A. The study of compressible fluid nature of plasma is important to understand as the density may need adjustments with the change in the cross-sectional area of the flux tube. Different magnetic field variation is studied later in this chapter, especially while comparing the heat flux between the overhill and downhill magnetic field. For a constant magnetic field (B), magnetic flux (Φ) passing through a surface area (A) given by Eq. (6.8),

$$\Phi = BA \tag{6.8}$$

Using the conservation of the magnetic flux [41], one gets

$$\Phi_0 = \Phi_1, \tag{6.9}$$

$$\left(\frac{r_1}{r_0}\right)^2 = \frac{B_0}{B_1}, \tag{6.10}$$

where r_1, and r_0 are the cross section radii. And from conservation of mass in fluid dynamics, ($nvA = constant$),

$$\frac{(nv)_0}{(nv)_1} = \left(\frac{r_1}{r_0}\right)^2, \tag{6.11}$$

where n_0 and n_1 are densities.

$$\frac{B}{nv} = \text{constant}, \tag{6.12}$$

suggests that transverse compression of the magnetic flux increases both B and nv [90]. For incompressible fluid: n stays constant as B↑, but v ↑ with B, and for compressible fluid: v stays constant as B ↑ and n ↑ with B.

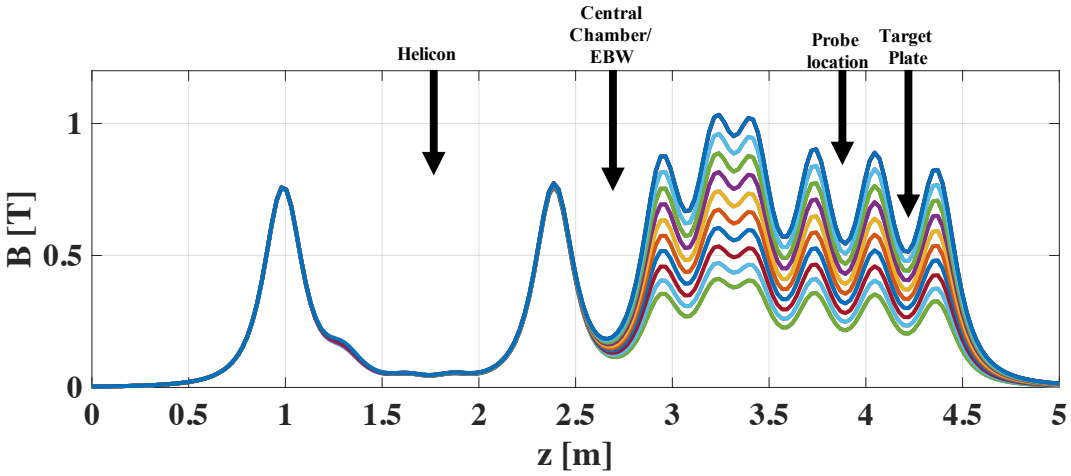

Figure 6.2: Axial magnetic field profiles in Proto-MPEX in Configuration A. The variation in the field obtained from the B-field scan conducted for the compressible flow study.

In Proto-MPEX Configuration A (described in Chapter 2), an experimental case study was conducted to study whether the plasma in Proto-MPEX is incompressible or compressible. Mach-double probe (M/DLP) measured axial plasma parameters (n_e, T_e and M) at r = 0 in the varying magnetic field region downstream of the central chamber for helicon-only discharges (see Figure 6.2). During the experiment, the source conditions were kept constant.

Figure 6.3a shows n_e as a function of B at the measurement location. n_e clearly increases linearly with B-field, and M (Figure 6.3b) is approximately constant with B-field, staying above 0.3, T_e stays about the same, which fluctuates between 1.5 and 2 eV. It should be noted that M > 0.3 for the entire scan; Ref. [91] states that when M > 0.3, the fluid should be considered as a compressible fluid. Hence, these experimental observations imply that plasma flow in Proto-MPEX should be treated as a compressible fluid, which is important to understand when examining transport and loss mechanisms. The particle density on the flux tube may vary even though the number of particles is not changing because of the flux-tube cross-sectional area variation.

Eq. (6.12) shows the ratio of B/nv remains constant, and since $B \propto I$, the ratio of I to nv is plotted in Figure 6.4 and normalized to the peak value. The plots show small variation in the ratio with an increase in the coil current, suggesting that it stays constant to the change in the magnetic field. In the case of an incompressible fluid, where the density stays constant with the change in the cross-sectional area, and the velocity goes up. The observation shown here shows the density goes with the field, and the flow stays approximately constant on the flux tube with the increase in the field. All the evidence indicate the plasma is **compressible** in Proto-MPEX. The density variation needs accounting for any change in the flux expansion.

6.3 Parallel heat transport

The understanding of the transport of plasma from the source to the target can be carried out by determining the parameters such as T_e, n_e, electron pressure (p_e), Mach number (M) along the axial length of the device and provides the change in plasma behavior along the device. The use of those experimental data to create a data-constrained model using the B2-Eirene fluid-neutral revealed the plasma fluid approximation that is traditionally used in the edge plasma region of a tokamak is sufficient to define plasma transport in Proto-MPEX (discussed in chapter 5). In fluid plasma transport, the energy tranfer from the source to the target is mainly governed by convection and conduction. The energy transport parallel to the magnetic field, in the SOL, is obtained from Eq. (6.13) [92, 93],

$$\frac{d}{ds}\left[-k_{\parallel}(T_e)\nabla_{\parallel}T_e + nu_{\parallel}\left(\frac{5}{2}(T_e+T_i)+\frac{1}{2}m_i u_{\parallel}^2 + I_0\right)\right] = S_E \tag{6.13}$$

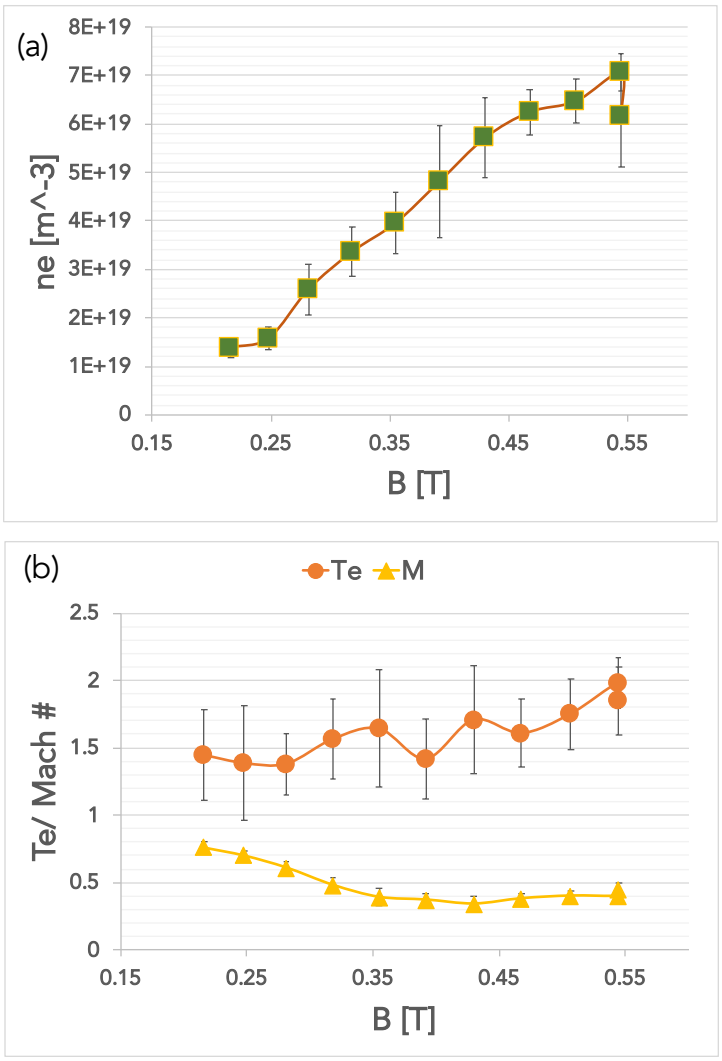

Figure 6.3: Plasma (a) electron density (b) electron temperature, and Mach number as a function of B at the measurement location.

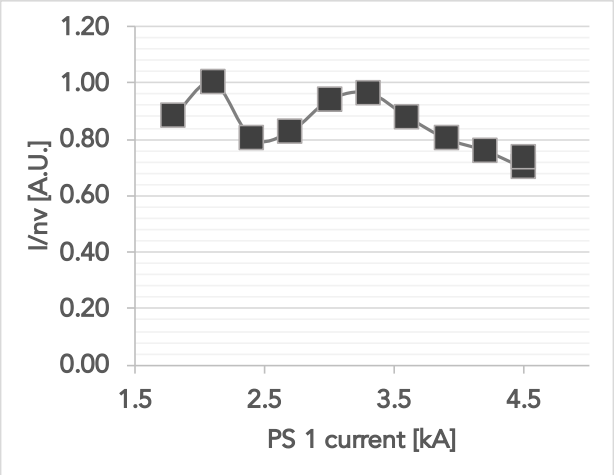

Figure 6.4: Ratio of I to nv as a function PS1 current taken downstream of the central chamber (at z = 2.7 in Figure 6.2) is plotted and normalized to the peak value. PS1 is used as a proxy to the change in magnetic field.

where, $k_{||}$ is the parallel electron thermal conductivity, given by,

$$k_{||} = \frac{3.2\tau_e n_e T_e}{m_e} \tag{6.14}$$

$k_{||}$ is function of T_e given by $\kappa_0 T^{5/2}$, and for pure hydrogenic plasma it is approximately 2000 $T^{5/2}$ for electrons. τ_e is the electron collision time, given by,

$$\tau_e = \frac{3\ \sqrt{m_e} T_e^{1.5}}{4\ \sqrt{\pi}\ n_e\ e^6 ln(\Lambda)} \tag{6.15}$$

S_E is the volumetric source and sink of energy, I_0 is the atomic ionization and molecular potential, which is 13.6 eV for hydrogen and 2.2 eV for deuterium. The first term is the electron thermal conduction equation,

$$q_{d||} = -k_{||}(T_e)\nabla_{||}T_e, \tag{6.16}$$

and the second term is the thermal convection equation,

$$q_{v||} = nu_{||}\left(\frac{5}{2}(T_e + T_i) + \frac{1}{2}m_i u_{||}^2 + I_0\right). \tag{6.17}$$

Understanding the nature of plasma close to the target is critical for PMI studies. In addition, the plasma target acts as the energy and particle 'sink' and is a critical component in defining the transport regime for the entire device. The B2-Eirene model has shown the transport from the axial vicinity of the source, and away towards the endplates, the transport is primarily conductive. To corroborate, experiments using a Mach probe near the helicon have also given $M \approx 0$.

6.4 Heat transport on Configuration A

Chapter 5 discusses the axial transport of plasma parameters for configuration A for helicon only discharges. To reiterate, the axial length of the Proto-MPEX, in this configuration, could be compartmentalized into three sections: 1) source region, 2) central chamber/28 GHz launch, and 3) target region. The 28 GHz for the helicon only discharges are not present, but the central chamber region remains a unique axial location in Proto-MPEX where a large magnetic well exists due between two high B-fields separating the helicon source and transport region. In Chapter 5, using the axial parameters a data-constrained B2.5-Eirene model was created and compared with the experimental observation. The B2.5-Eirene model is also used to obtain the axial heat transport profile. Figure 6.5, retrieved from Ref. [94], shows the heat flux from conductive and convective components in Configuration A using B2.5-Eirene.The model showed the $q_{d||}$ was present near the helicon source region where P_e was 30–40 Pa and the plasma velocity was small;

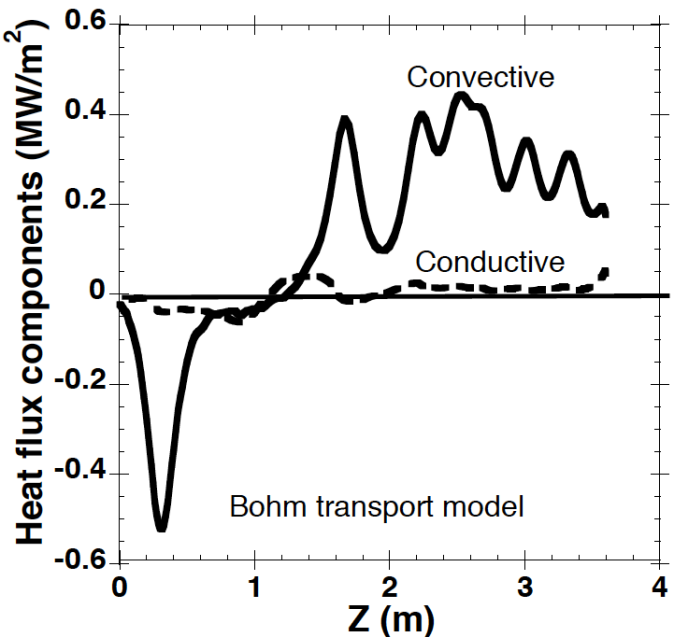

Figure 6.5: Axial heat fluxes from conductive and convective transport in Proto-MPEX Configuration A

therefore, $q_{v||}$ is negligible at the source. But, $q_{v||}$ predominates a short distance away from the source reason which suggested pressure driven transport towards the target region. $q_{v||}$ away from the plasma source is significantly higher than the $q_{d||}$. The plasma flow increases towards the target and because the electron temperature gradient is small comparatively, the $q_{d||}$ is almost negligible.

Moreover, during the 28 GHz launched at the central chamber in Configuration A, local electron heating off-axis was evident in an overdense plasma. Figure 6.6, obtained from Ref. [46], shows radial measurements from the Thomson scattering system at the central chamber (left) and at the target (right). The plot presents helicon-only (black) and helicon with EBW (red) T_e and n_e profiles. The vertical radial profiles at the central chamber indicate T_e rise at the top of the plasma column where the 28 GHz power was injected. The local T_e rises from 5 eV (helicon-only) to ≈15 eV (helicon + EBW). The core electron density at the central chamber decreases slightly during EBW, but n_e remains overdense, which confirms the occurrence of EBW heating. Despite the large T_e rise in the central chamber, the increase in the target T_e remained minimal.

Just looking at the two-point measurements from the Thomson scattering at the central chamber and the target region with EBW heating indicates a large T_e-gradient from the heating section to the target. However, the presence of the mirror cannot be ignored. The particles could be trapped from being transported towards the target region. As the electrons are heated, they become increasingly collisionless and are kinetically trapped in the magnetic well at the central chamber. Monte-Carlo simulation conducted on Proto-MPEX [95] has shown high energy tails of EEDF distribution become kinetically trapped as the 90-degree scattering mean free path becomes

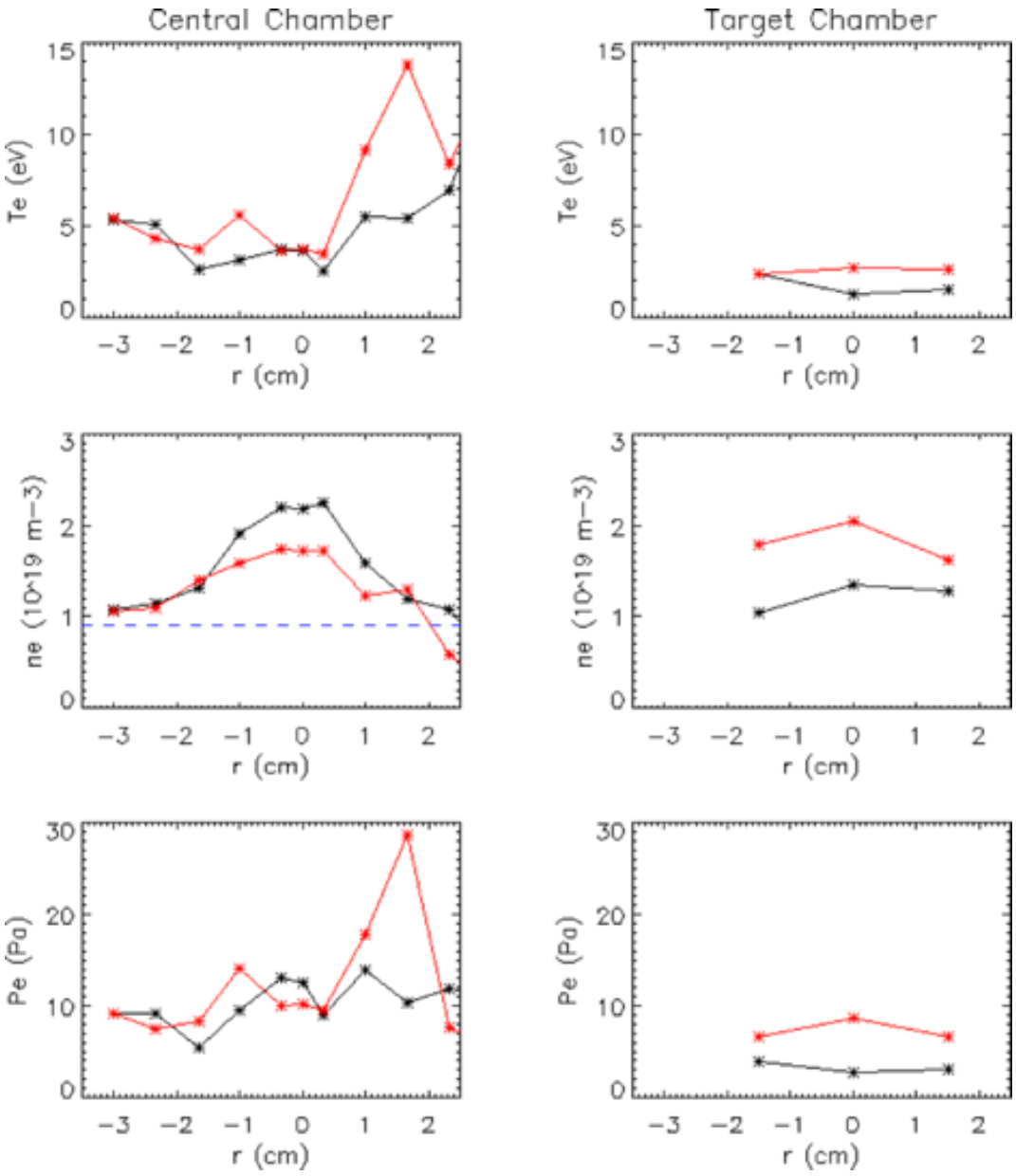

Figure 6.6: Thomson scattering radial Profile of n_e, T_e, and P_e with (red) and without (black) 28 GHz measured in (left) the central chamber, and (right) in the target region. The 28 GHz wave is launched at the central chamber, and blue line represents the cut off of the electron cyclotron wave propagation.

larger than the length of the mirror ($L_m \approx 0.5$m) at the central chamber. These results obtained from heating at the central chamber prompted the upgrade of Proto-MPEX to Configuration B. 6.5 presents the axial transport of helicon and auxiliary heating in Configuration B.

6.5 Axial plasma transport on Configuration B

As discussed previously in Chapter 2, Proto-MPEX in Configuration B can be axially divided into four separate regions: 1) source, 2) central chamber, 3) auxiliary heating, and 4) target. In this configuration, measurements are taken at each region, represented by the orange boxes, as shown in Figure 6.7. Experimentally measurements of the plasma parameters were taken at the critical axial locations using DLPs at each of the four locations. To obtain DLP radial profiles at each axial location required several discharges.

The operational premise of overhill and downhill B-field cases was to identify the most efficient transport of heated plasma particles to the target. In the overhill configuration, the energetic electrons are transported towards the target through higher B-field region, as the heated electron pass through the higher field, there is a possibility of a small portion of the electron tail population being trapped. Operating Proto-MPEX in the downhill condition with a downward slope or flat magnetic field profile should improve the transport efficiency of particle and heat fluxes on to the target. A key plasma parameters comparison between the overhill and downhill field condition with and with 28 GHz is conducted below in this section.

6.5.1 Axial plasma behavior on helicon and auxiliary heating

The axial T_e, n_e, p_e, and M profiles for the helicon discharges for overhill (red) and downhill (black) magnetic field conditions are shown in Figure 6.8. The plasma parameters in both configurations are similar near the source region, but the n_e is higher at the heating launcher due to compression of the magnetic flux tube in the overhill B. The temperature as a result decreases. p_e (where$P_e = T_e n_e$), is highest near the source and decreases axially toward the target. Moreover, p_e in both the overhill and downhill cases are similar. During the experimental campaign, a DLP at z = 1.1 m (i.e., spool 1.5) is taken to be as the closest approximation to the conditions at the

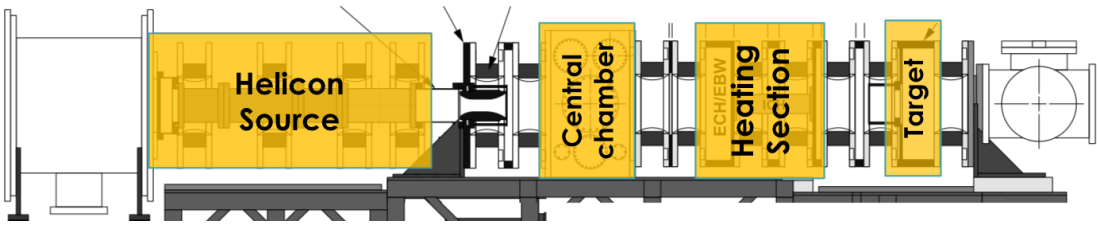

Figure 6.7: Axial division of Proto-MPEX into different transport regions in Configuration B

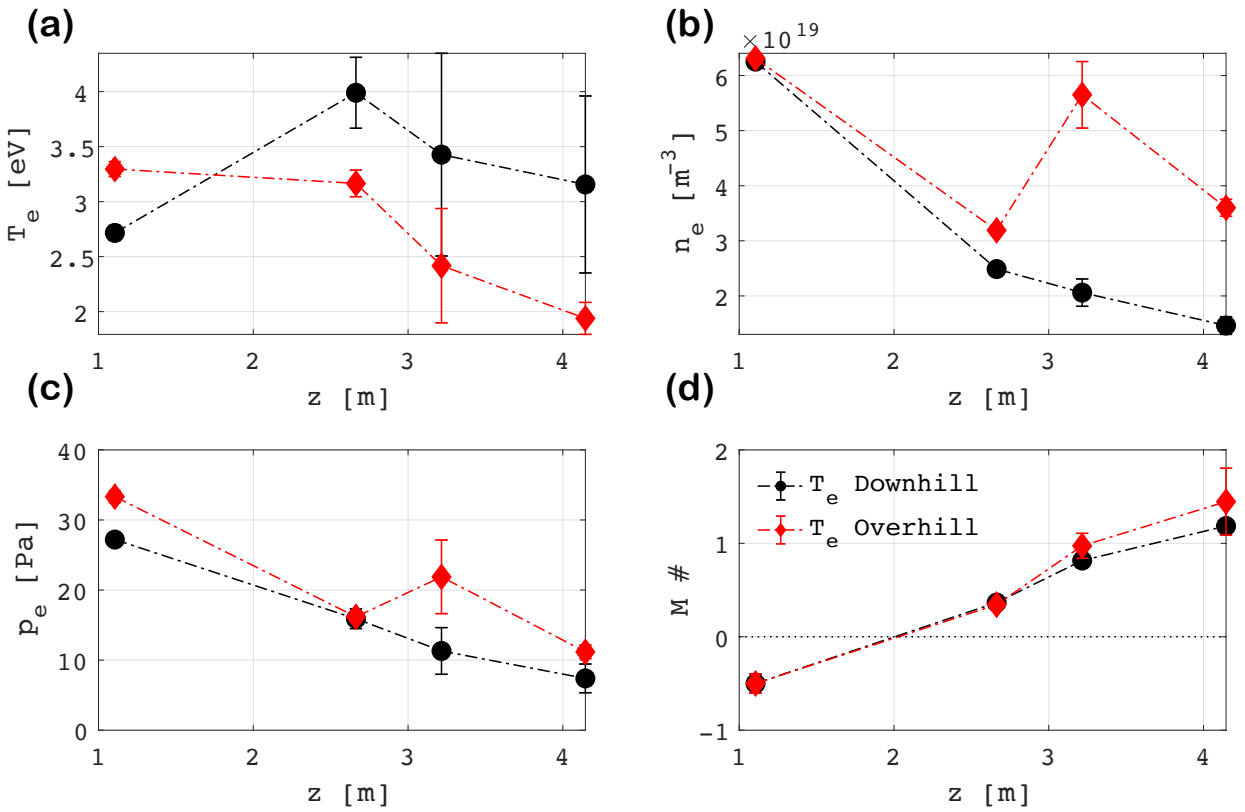

Figure 6.8: Axial plasma parameters showing (a) axial electron temperature, (b) density, (c) static plasma pressure, and (d) Mach number for **helicon-only** discharges. The red and the back profiles represent two magnetic configuration applied downstream of the auxiliary heating section for electron heating.

helicon source. A standard DLP was used for measurements instead of Mach-double Langmuir probe (MDLP).

Figure 6.8d shows a continual increase in the Mach number downstream of the source in both overhill and downhill field geometries. Configuration B used M of 0.5 measured at spool 1.5 in Configuration A. Since the source dimensions and parameters remained consistent between Configurations A and B in Proto-MPEX, M of 0.5 is an appropriate approximation.

The axial plasma profile with EBW auxiliary heating is also studied with both the overhill and downhill magnetic field conditions. 28 GHz microwave power is launched with the electron density above the cutoff (1e19 m^{-3}) for the second harmonic O-mode launch. T_e near the target in both Configurations A and B were comparable for the helicon-only discharge. However, in upgraded Configuration B, T_e rose both at the 28 GHz launcher and near the target during EBW resonance coupling. T_e increased 3.5 eV (helicon-only) to 8 eV (helicon + EBW) at the launcher, which propagated toward target, where T_e increased from 2 to 7 eV (see Figure 6.9). A large T_e increase of 4 to 5 eV was never observed in the target region in Configuration A, where T_e increase was local to the central chamber. The rise in the temperature is evidence of the improved transport performance when launching the 28 GHz near the top of the magnetic hill.

Figure 6.9 (top) shows T_e axial profile comparing helicon and helicon + EBW heating discharges for (a) overhill and (b) downhill configuration. Similarly, n_e, P_e, and M are compared for two conditions in consequent plots in the figure. The electron density drops when 28 GHz is launched downstream towards the target, which is more prominent in the overhill case than the downhill. n_e with 28 GHz drops to similar values for both cases. The physics understanding of the density drop phenomenon is under investigation. Comparing the axial p_e during helicon discharge the pressure continually drops from the source region to the target, but after adding EBW to the system, there is a small pressure increase between the 28 GHz launcher and the target, which is chiefly because of the rise in T_e. The increase in the pressure downstream is still smaller than the pressure near the helicon source. The plasma pressure gradient, therefore, is still the driving mechanism of plasma transport from the source to the target with 28 GHz added. The Mach number profile (bottom) in Figure 6.9, drops at the launcher and the central chamber with 28 GHz but increases near the target.

For a side-by-side comparison of the EBW performance during overhill (red) and downhill (black) B geometry, axial profiles of T_e, n_e, p_e and M are plotted in Figure 6.10. T_e profile from both downhill and overhill conditions were observed to be similar; however, average T_e rise from 28 GHz heating in the downhill condition was $\sim$ 1 eV higher than the overhill condition. The density profiles in both cases were similar; even though overhill condition produces larger flux compression. The axial pressure and flow profiles were similar in both cases.

Using the criteria of the two-point model f_T and ν^* is calculated with the addition of EBW heating. For this case, T_e between the heating and target are considered as T_u and T_t. With $T_u = 9eV$ and $T_t = 7$, $f_T \approx 1.28$ is obtained. The connection length (L) is $\sim 1\ m$, n_u is $1.5 \times 10^{19} m^{-3}$,

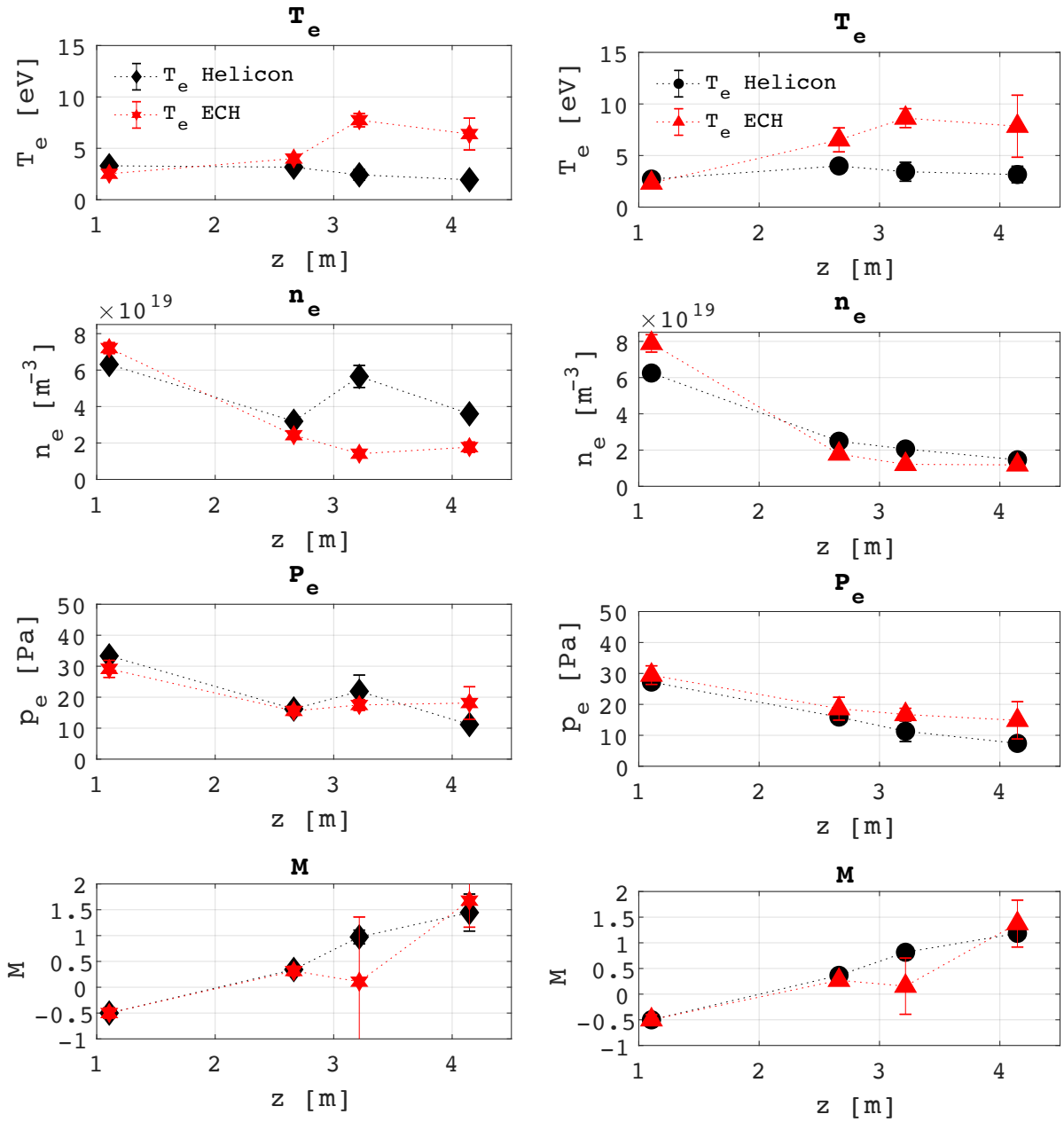

(a) Overhill condition

(b) Downhill condition

Figure 6.9: Axial plasma parameters showing (from top to bottom) axial electron temperature, density, static pressure, and Mach number for helicon (black) and with 28 GHz (red) discharges for the (a) Overhill condition and (b) Downhill condition.

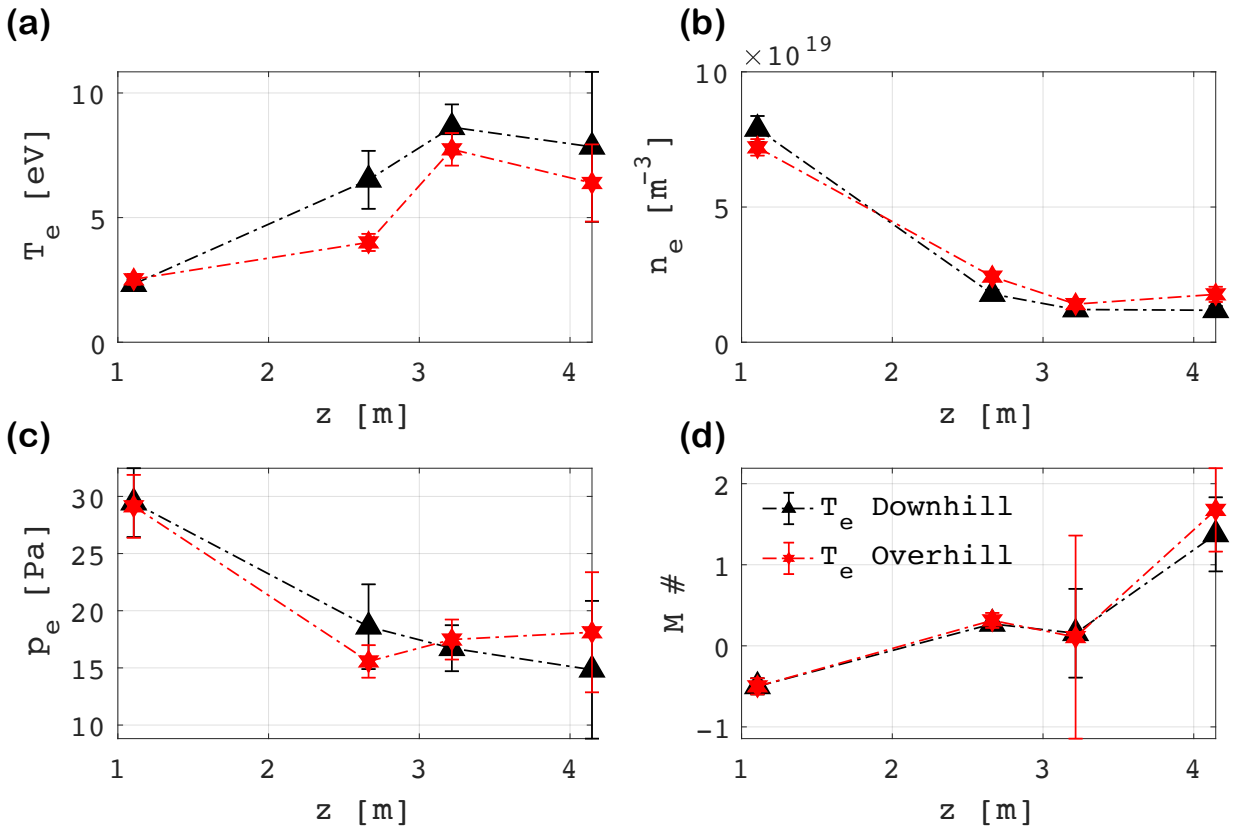

Figure 6.10: Axial plasma parameters showing (a) axial electron temperature, (b) density, (c) static pressure, and (d) Mach number for overhill (red) and downhill (black) field conditions when **28 GHz EBW is applied** to the helicon plasma.

which gives $\nu^* \approx 18$. In this case, $f_T < 3$ and ν^* is much lower than the helicon-only case ($\nu^* \sim 890$). Based on the criteria previously identified, the plasma transport with EBW heating in Proto-MPEX is close to the sheath-limited regime. Heat transport analysis will further illuminate this case.

6.5.2 Heat transport in Configuration B

The parallel heat transport during the helicon-only discharge in configuration B is still primarily conductive near the source region and away from the source is predominantly convective. From the previous section, it was identified that p_e in the source region is higher than the pressure downstream. The pressure-driven profile suggests that the heat transport towards the target for the helicon-only plasma is still mostly governed by convective heat flux. Likewise, after adding 28 GHz to the system, the plasma pressure gradient is again driving the particles away from the source region toward the target.

Figures 6.11 and 6.12 shows the axial heat fluxes calculated from the measured parameters. Figure 6.11 shows $q_{d\|}$ comparing helicon and helicon with EBW plasma for (a) downhill, and (b) overhill magnetic fields. In both overhill and downhill cases, helicon-only discharges show $q_{d\|}$ higher near the source than near the target. $q_{d\|}$ directed towards the target is denoted using positive values and vice versa. Peak q_d reaches $\sim$40 kW/m^2 for the helicon-only discharge. Adding EBW elevated T_e at the launcher, which increased $q_{d\|}$ between the central chamber and the heating section. A new T_e gradient is created at the heating section, which drives the conductive heat both towards the helicon source and the target plate. Comparing the magnitude of $q_{d\|}$, shows that the heat flux at the launcher is larger in the downhill case than the overhill case. An asymmetric mirror present between the heating and the target section seem to have affected the transport in the overhill case, which may also have reduced the transport efficiency.

Similarly, Figure 6.12 shows the convective heat flux ($q_{v\|}$) for helicon-only and helicon + EBW plasma for (a) downhill, and (b) overhill magnetic fields. In the downhill magnetic field, for the helicon-only discharge, q_v increases away from the helicon source. $q_{v\|}$ reaches its maximum of about in the heating section and remains flat up to the target region. Adding EBW in the downhill field, decreased q_v at the heating region, but increased substantially at the target region. The rise in $q_{v\|}$ relates to the rise in T_e and M. In figure 6.12b, $q_{v\|}$ for the overhill magnetic field exhibits similar to that of downhill magnetic field, where $q_{v\|}$ increases away from the helicon source. Similarly, when adding EBW, a fall in $q_{v\|}$ is observed in the launch place. In both plots, $q_{v\|}$ with EBW is much larger at the target region than the helicon-only discharges. $q_{v\|}$ reported in Figure 6.12 showed overhill field delivering higher heat flux on the target than the downhill case. The overhill field seems to be more efficient than the downhill field, but the cross-sectional area of the plasma is much larger in the downhill field.

The convective heat flux is a function of T_e, n_e, and M; therefore, all the measured parameters play a key role in determining q_v. As discussed in the earlier section, due to the

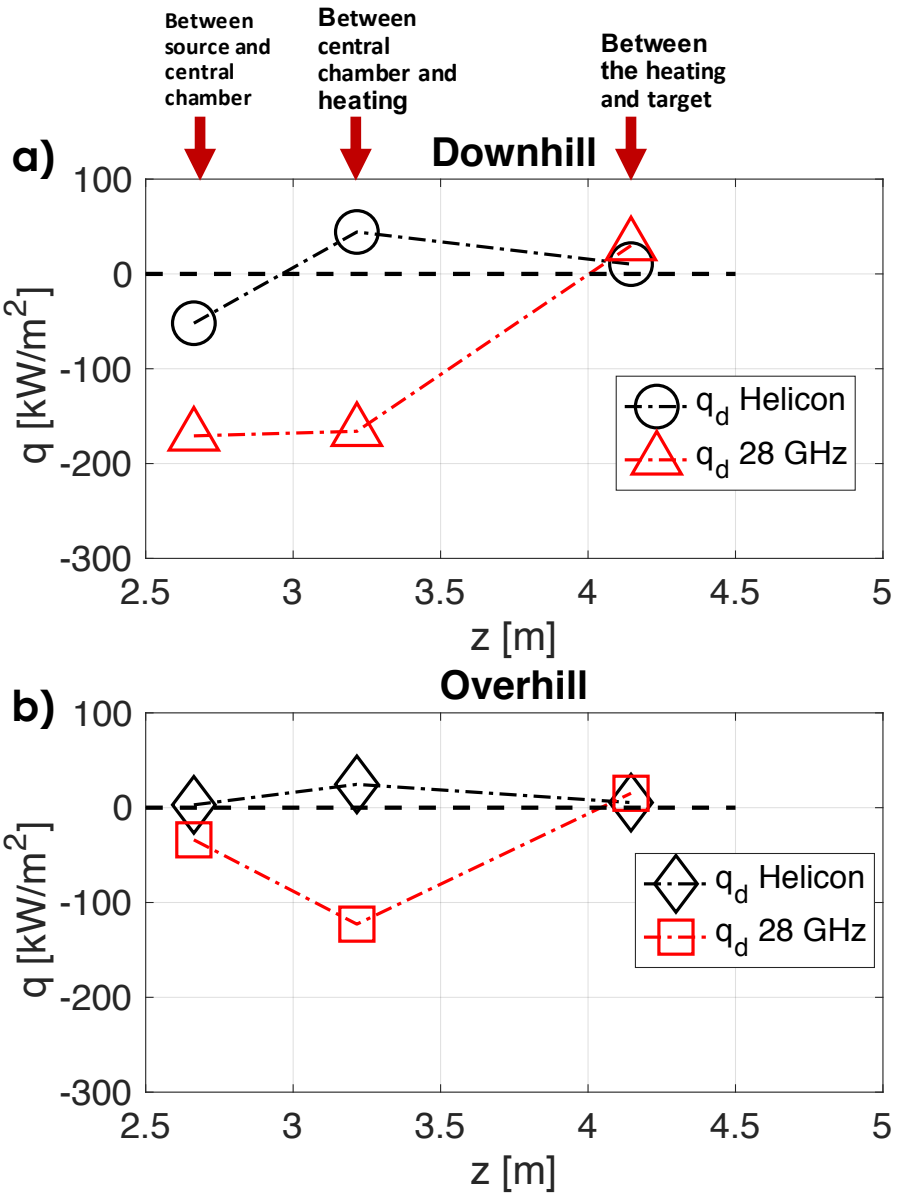

Figure 6.11: On-axis $q_{d\|}$ transport for helicon-only and helicon with 28 GHz discharges for overhill and downhill magnetic field conditions is shown. The data points in the plot shows $q_{d\|}$ between the source and the central chamber, between the central chamber and the heating region, and between the heating and the target region.

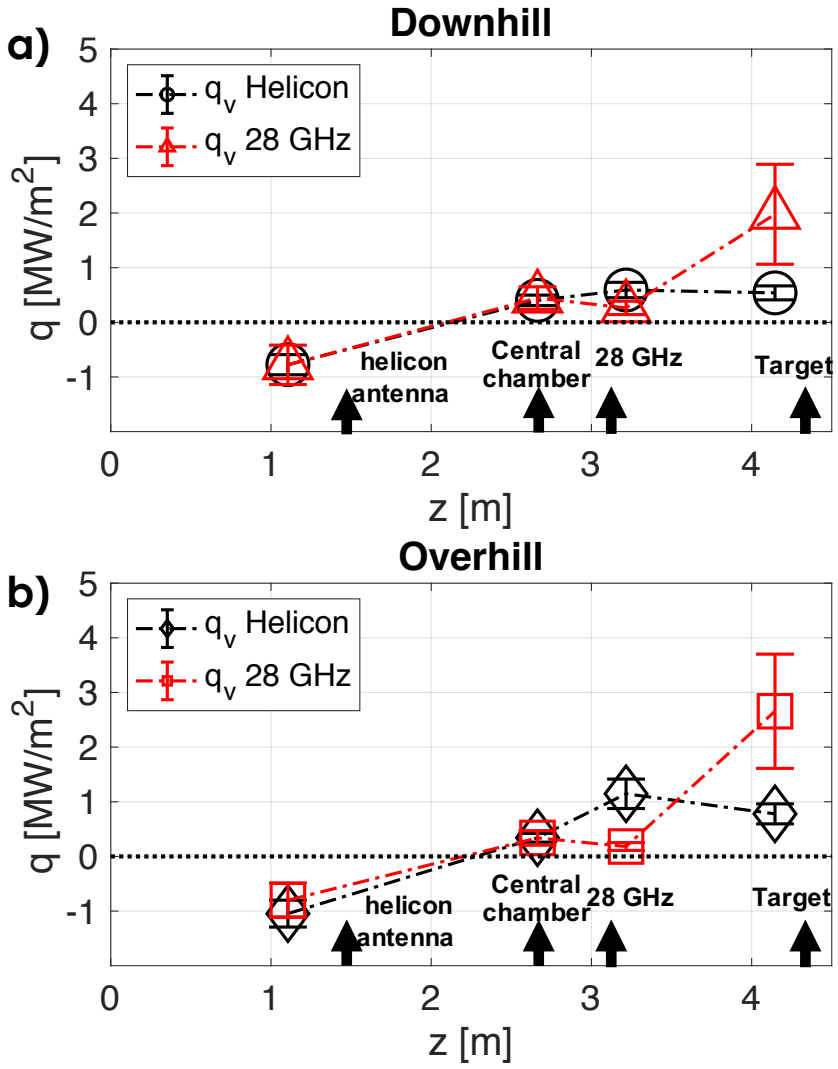

Figure 6.12: On-axis $q_{v\|}$ transport for helicon-only and helicon with 28 GHz discharges for overhill and downhill magnetic field conditions is shown.

compressible nature of the plasma in Proto-MPEX, axial variation in the plasma density exists. Accounting for the density change is important in determining $q_{v||}$. Normalizing one of the magnetic fields to another provides a one-to-one comparison. In this case, downhill field is normalized to overhill field. Figure 6.13 shows the normalized downhill B-field for both helicon only and helicon with EBW discharge. The normalization keeps the axial shape of the axial q_v same but changes the magnitude of the heat flux. The magnitude shows of the normalized downhill heat flux are ≈ 3.5 MW/m^2 at the target region, which is about 1 MW/m^2 higher than the overhill B-field case. A direct comparison shows that the downhill condition is more efficient in transporting plasma to the target compared to the overhill condition. Another advantage of the downhill B-field is the increase in the plasma footprint on the target. The plasma diameter increases by 3 cm (from 5 to 8 cm) in the downhill case when juxtaposed to the overhill case. Moreover, the analysis also shows that the axial $q_{d||}$ is smaller in magnitude than $q_{v||}$ for the majority of the device except near the helicon source (as seen from B2.5-Eirene modeling and the flow measurement near the helicon source).

6.5.3 EBW flow measurement in overhill and downhill magnetic geometry

In addition to the heat flux measurements, Mach-double probes measured axial M for the overhill and downhill conditions. In Configuration B, a probe did not measure M close to the helicon antenna; therefore, in the source region, M of 0.5 was used for both helicon-only and helicon + EBW discharges. Figure 6.14a shows the axial M gathered at r = 0 for the downhill magnetic field. The flow for both helicon and helicon + EBW discharges increases towards the target. However, during EBW heating, the flow was lower both at the central chamber and the heating section, which indicates plasma slowing down. The axial velocity deduced using M and T_e showed a similar trend (Figure 6.14b). However, due to the increase in T_e downstream of the 28 GHz launcher, the plasma velocity slightly increased at the heating section. The average velocity in the target region is much larger than the helicon-only discharge primarily due to an increase in T and M.

Similarly, the axial flow analysis for the overhill case is shown in Figure 6.15a. A similar trend occurred while comparing the overhill and downhill magnetic fields. During the overhill B geometry, measured M was lower at the 28 GHz launcher than in the downhill case. Likewise, Figure 6.15b shows the axial velocity profile in the overhill magnetic field. Again, the velocity trend in the overhill and downhill conditions are similar. The only difference is in the average velocity at the 28 GHz launcher in the overhill B, being slightly lower than in the downhill B. However, in the overall axial flow profile, the differences are minute. The flow profile analysis for both cases showed M upstream of the heating location could be slowing down due to anisotropic resonance heating upstream of the magnetic mirror, suggesting that the mirror may have some

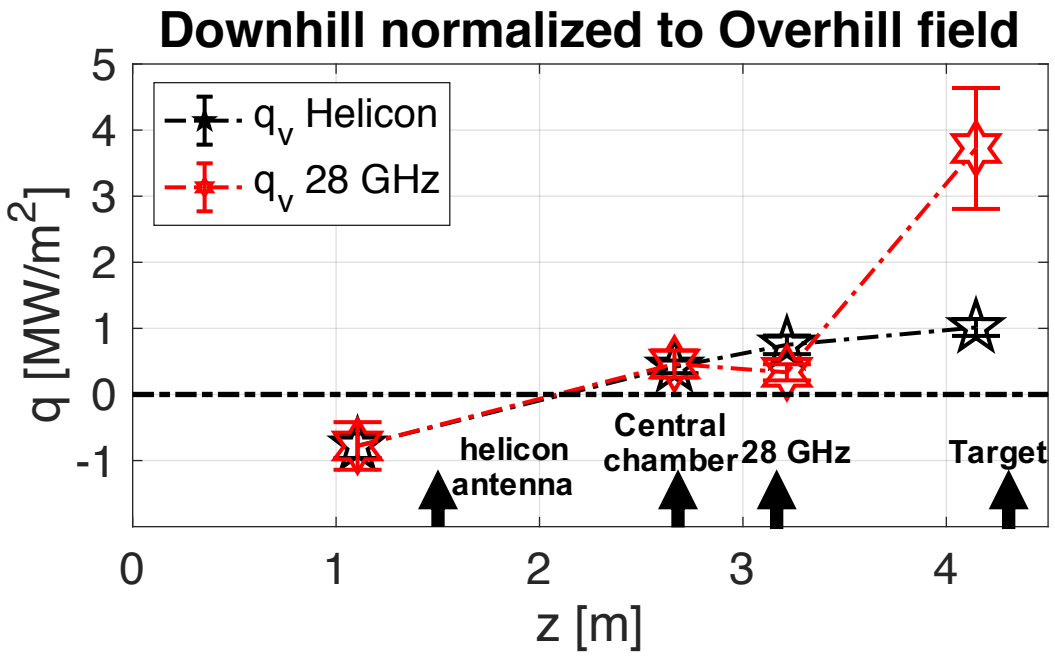

Figure 6.13: Downhill field normalized to the overhill field to investigate the transport efficiency between the two magnetic field geometries.

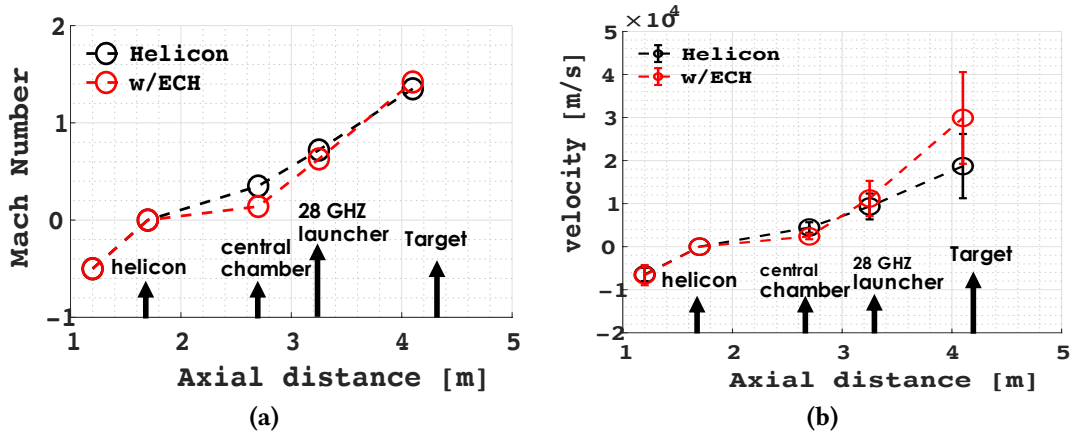

Figure 6.14: On-axis axial (a) Mach number and (b) velocity profile is shown for the **downhill** condition.

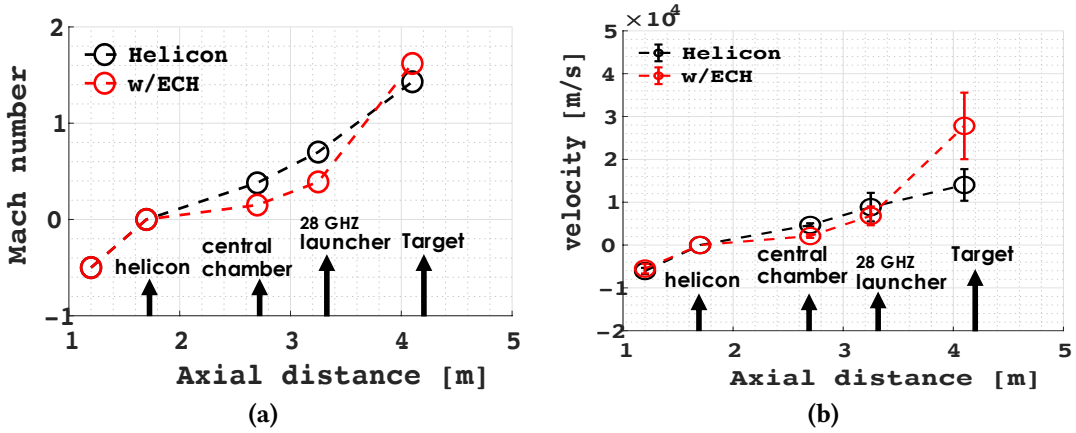

Figure 6.15: On-axis axial (a) Mach number and (b) velocity profile is shown for the **overhill** condition.

effect on the flow behavior. Next chapter will discuss the effects of magnetic mirrors in Proto-MPEX and also the heat flux measurements on the target for the overhill and downhill magnetic geometries.

6.6 Summary

This chapter provided further illustration of Proto-MPEX in the perspective of the divertor SOL surface and pointed out similarities and differences between them. Proto-MPEX is unique in a way as it can direct particle production and heat injection in various amounts as required for experimental studies. The chapter also presented a discussion on the compressible nature of the plasma in Proto-MPEX.

The picture of the Proto-MPEX parallel transport is convection dominated, and a sheath-limited regime exists in Proto-MPEX. A small parallel temperature gradient exists, therefore negligible heat is conducted for the helicon only discharges. Despite a finite temperature gradient after adding 28 GHz heating, the parallel heat conductivity is modest in comparison to convective heat transport along the flux tube. The compressible fluid conversion shows that the downhill configuration is more effective than the overhill configuration at delivering heat to the target.

Chapter 7

Experimental investigation of the effects of magnetic mirrors on plasma transport in Proto-MPEX

7.1 Introduction

Chapter 6 described heat transport in Proto-MPEX and quantified the plasma transport behavior. Chapter 6 also briefly focused on the behavior of the mirrors and highlighted differences in the axial plasma behavior in overhill and downhill field conditions. The effects of the mirror during helicon-only discharges had a small effect on the plasma for the desired operating overhill and downhill conditions. However, an increase in the mirror ratio to a larger value may increase the confinement of the particles. The presence of these mirrors in Proto-MPEX affects plasma transport to the target. Proto-MPEX has three mirrors along the device: helicon source ($L_{m1} \sim 1$ m), central chamber ($L_{m2} \sim 0.5$ m), and target ($L_{m3} \sim 0.1-0.2$ m). The magnetic field near the helicon source is ∼0.05 T, and the peak magnetic field in Proto-MPEX is ∼1.8 T; which results in a large magnetic well for particles traveling from the helicon towards the target. A recent magnetic reconfiguration in Proto-MPEX has allowed the capability to make local B variation without affecting the magnetic field in the source and the target regions. Experiments have been conducted to obtain the axial profiles of various plasma parameters (n_e, T_e, and M) along the axial length of the device for several heating scenarios.

This chapter focuses on the experimental investigation of two plasma population: isotropic low energy plasmas, and anisotropic high energy plasmas. Effect know as Gas-dynamic transport is known to trap collisional and isotropic plasma, where the low temperature plasma gets confined at the magnetic mirror throat. The second is due to kinetic mirror trapping of energetic ions and electrons with the injection of ICH and ECH/EBW. Since Proto-MPEX consists of both types of plasma population, it is essential to investigate the effects of magnetic mirrors. This chapter will

provide a theoretical calculation of the collisional mean free path for ions and electrons, discuss the experimental observation of Gas-dynamic transport, and magnetic mirror effects during ICH and EBW heating.

7.2 Background on magnetic mirrors trap

The magnetic field in Proto-MPEX has many ripples along the axis. In addition to the ripple, there are two deep B-field wells. One of which is in the helicon region, and the other one in between coils 6 and 7. Also, an asymmetric magnetic well is present between the ICH antenna, and the target, which largely depends on the heating scheme such as overhill or downhill conditions.

In the absence of collisions and when the Larmor radius is small compared to gradients in the magnetic field, a charged particle can be indefinitely confined both radially and axially inside a so-called magnetic mirror trap [96]. Magnetic mirror traps consist essentially of a central solenoidal magnetic field region bounded by two higher field regions called magnetic mirrors. Charged particles are adiabatically confined axially via the magnetic mirror force Eq. (7.1) which causes particles to reflect and bounce between magnetic mirrors. This force arises from to conservation of the magnetic moment, μ, shown in Eq. (7.2) and the kinetic energy.

$$F_{\parallel} = -\mu \nabla_{\parallel} B, \tag{7.1}$$

$$\mu = \frac{m u_{\perp}^2}{2B}, \tag{7.2}$$

here $u_{\perp}$ is the perpendicular velocity component. At the magnetic mirror, only $u_{\perp}$ when the parallel velocity component at the turning point is zero, which is given by the conservation of energy (Eq. 7.3),

$$u_0^2 = u_{\perp}^2 + u_{\parallel}^2 = u_{\perp}^2 \tag{7.3}$$

Using the magnetic mirror moment and conservation of energy, a relationship between $u_{\parallel}$ and $u_{\perp}$ is obtained (Eq. 7.4),

$$u_{\parallel}^2 = (R-1) u_{\perp}^2, \tag{7.4}$$

here R is the mirror ratio, which is given by Eq. (7.5),

$$R = \frac{B_{max}}{B_{min}}. \tag{7.5}$$

However, not all charged particles are adiabatically confined. This depends on the pitch angle θ of the particle in the central region relative to the so-called loss-cone angle, θ_{LC}, of the mirror trap. The pitch angle is defined by Eq. (7.6) where $u_\perp$ is the particle velocity perpendicular to the background magnetic field. The loss-cone angle is given by Eq. (7.7) . Particles with a pitch angle in the central region satisfying $\theta > \theta_{LC}$ are adiabatically confined while in the opposite case ($\theta < \theta_{LC}$) particles reside in the loss cone and are lost from the mirror trap. This process leads to the so-called loss-cone distributions in velocity space which are anisotropic due to the depletion of the particles in the loss-cone [97].

$$sin(\theta) = u_\perp / u, \tag{7.6}$$

$$sin(\theta_{LC}) = R^{-1/2}, \tag{7.7}$$

7.3 Two plasma populations in Proto-MPEX

The 90°-scattering frequency ($\nu_\perp$) between the test particle 'a,' and background plasma 'b' is given by Eqs. (7.8) - (7.12) obtained from Ref. [98, 95]. In Proto-MPEX, for the background plasma density (n_b) of $4 \times 10^{19} \mathrm{m}^{-3}$, and temperature 3–4 eV, the 90°-scattering frequencies ($\nu_\perp$) and collision mean free path ($\lambda_\perp$), given by $\nu_t / \nu_\perp$, are plotted as a function of test particle energy in Figure 7.1 for electrons, and Figure 7.2 for ions. Figure 7.1 shows that the helicon plasma falls under particles having low energy; therefore, are the 90°-scattering mean free path is smaller than L_m in Proto-MPEX.

$$\nu_\perp^{ab} = \nu_{ab}^0 \left(\frac{\Phi(x) - \Psi(x)}{x^3} \right) \tag{7.8}$$

where each term is given by,

$$x = \frac{v_t}{v_b} \tag{7.9}$$

$$\nu_{ab}^0 = \frac{n_b e^4 \ln\Lambda}{2\pi m_a^2 \epsilon_0^2 v_b^3} \tag{7.10}$$

$$\Psi(\mathrm{x}) = \frac{\Phi - x\Phi'}{2x^2} \tag{7.11}$$

$$\Phi = \frac{2}{\sqrt{\pi}} \int_0^x \exp\left(-\eta^2\right) d\eta. \tag{7.12}$$

Terms appearing in the equations are as follows: $\mathrm{v_t}$ is the velocity of the test particle, $ln\Lambda$ is the Coulomb logarithm, which has a value between 15–20, ϵ_0 is the vacuum permittivity, and

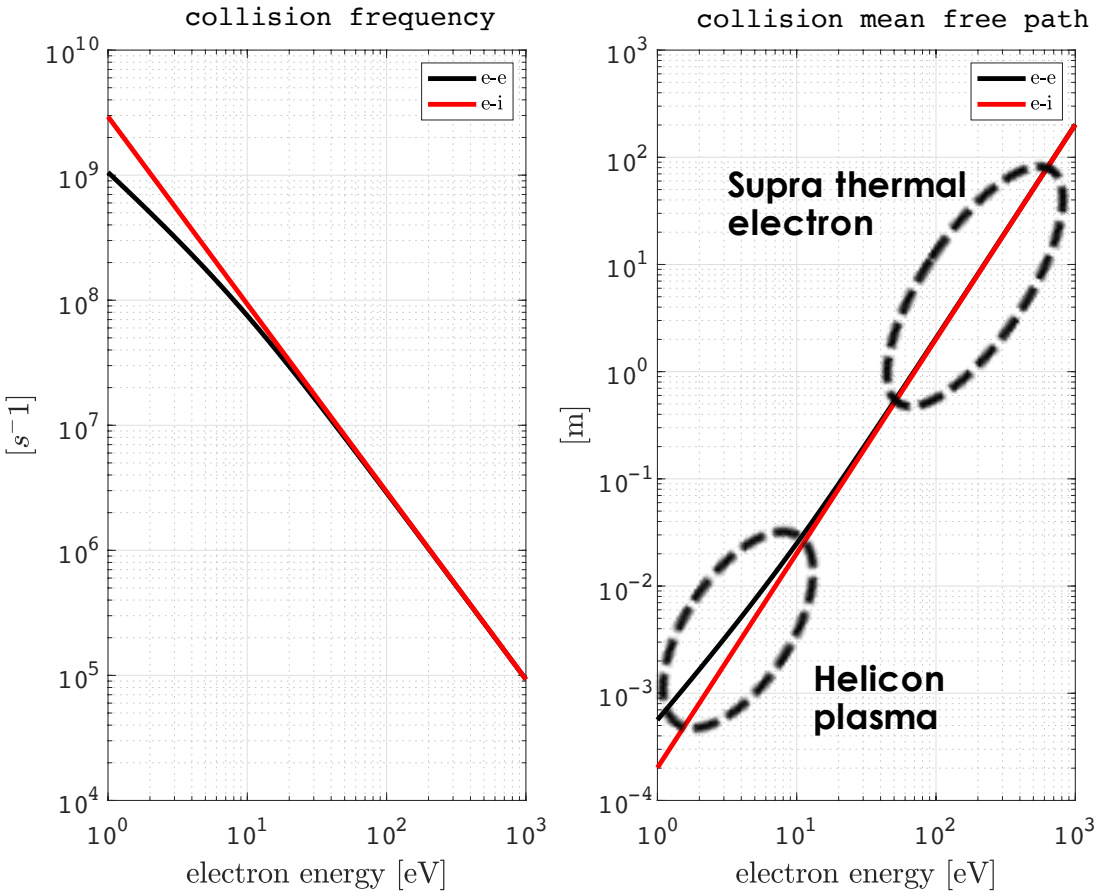

Figure 7.1: Plot shows 90 degree scattering (left) collision frequency ($\nu_\perp$) and (right) mean free path ($\lambda_\perp$). Electron-electron (black) and electron-ion (red) interactions as a function of **electron energy** are plotted.

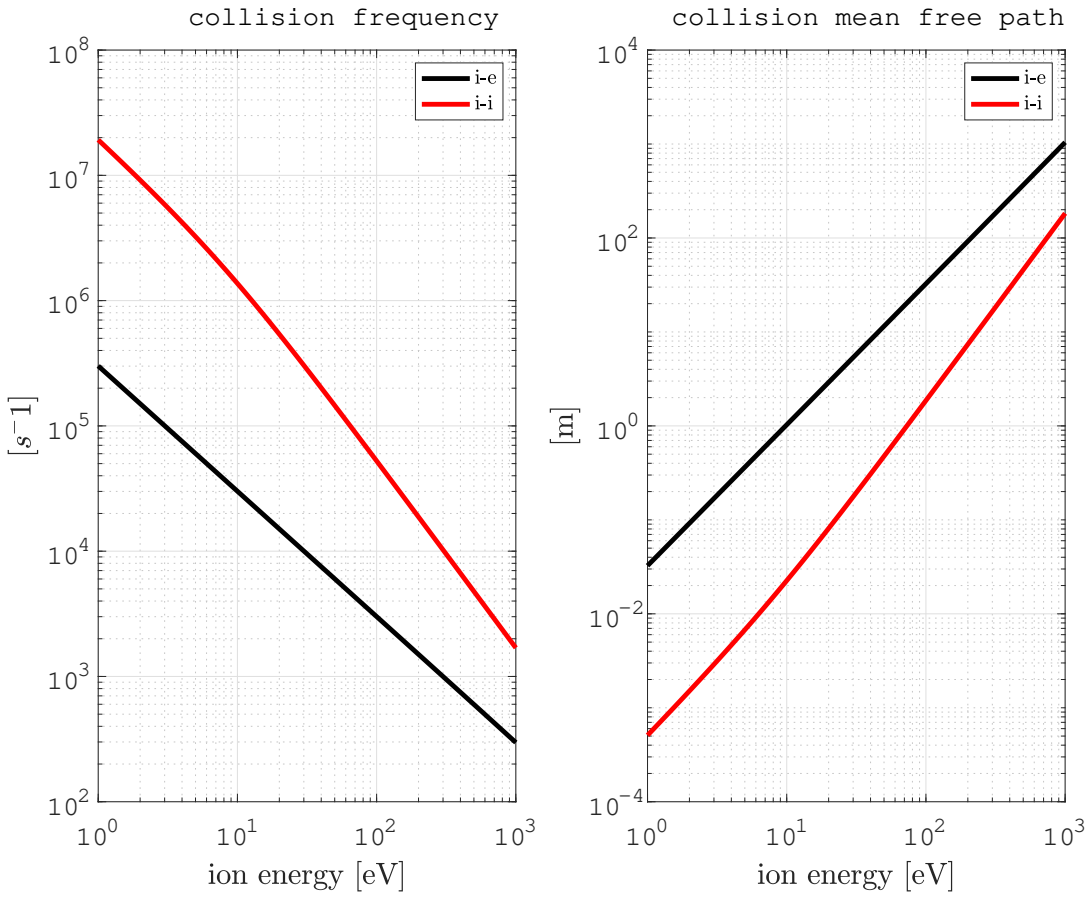

Figure 7.2: Plot depicts 90 degree scattering (left) collision frequency ($\nu_\perp$) and (right) mean free path ($\lambda_\perp$). Here, ion-electron (black), and ion-ion (red) interactions as a function of **ion energy**. are plotted.

v_b is the velocity of the background particle. Both plots show for low energy plasmas from 1-10 eV, which represents typical helicon only discharges in Proto-MPEX, the collision frequency is high and consequently the collision mean free path is low. For these low energy plasmas the mean free path is smaller than the length of the mirror present in Proto-MPEX. However, when energy of the particles increase by an order of magnitude with the addition of electron and ion heating there is an exponential decrease in $\nu_\perp$ and $\lambda_\perp$ becomes larger than the length scale of the device. The mirror effects with the 28 GHz heating is also being investigated using Monte-Carlo simulations [95] in Proto-MPEX for both launcher locations (the central chamber and the heating section).

7.4 Effect of collisions and transport regimes

The presence of collisions has the effect of randomizing the particle's pitch angle θ and is manifested as diffusion in velocity space. This leads to isotropization of the distribution function and populates the loss-cone region thereby enhancing transport out of the mirror trap. The impact of collisions in degrading adiabatic mirror confinement can be assessed by inspecting the ratio $\lambda_\perp/L_m$ where $\lambda_\perp$ is the 90-degree scattering mean free path and L_m the mirror-to-mirror length . Depending on the value of this ratio, two main transport regimes can be identified: When $\lambda_\perp \gg L_m$, charged particles are more likely to bounce adiabatically between magnetic mirrors and form loss cone distribution functions; hereafter, this regime is referred to as "adiabatic". On the other hand, when $\lambda_\perp \ll L_m$ charged particles are more likely to experience randomizing collisions before reflecting from a magnetic mirror. Under these circumstances, velocity space diffusion populates the loss cone and the distribution function approaches an isotropic Maxwellian [96]. Hereafter, this regime is referred to as "Gas-dynamic" [99, 100, 101, 102, 95].

For electron-ion, electron-electron and ion-ion Coulomb collisions, the 90-degree scattering collision frequency of particle type "a" deflecting on a background population of species "b" is approximately given by Eq. (7.13) [96], where $\ln\Lambda$ is the Coulomb logarithm and u_a is the speed of the particle "a".

$$\nu_\perp^{ab} = \frac{n_b e^4 ln\Lambda}{2\pi\epsilon_0^2 m_a^2 u_a^3}, \tag{7.13}$$

Using the definition of mean free path $\lambda_\perp^{ab} = u_a/\nu_\perp^{ab}$, the distance a charged particle must traverse to experience a cummulative 90-degree deflection from Coulomb interactions is given by Eq. (7.14) [96] where $E_{\|a}$ is the parallel kinetic energy of particle "a" in eV and n_b the density of species "b". Notice that the mean free path is independent of the particle mass, so both electron and ion-ion mean free paths are approximately the same for the same energy $E_{\|a}$.

$$\lambda_{\perp}^{ab} = \frac{E_{\|a}^2}{n_b e^2} \frac{8\pi\epsilon_0^2}{ln\Lambda}, \tag{7.14}$$

A plot of $\lambda_{\perp}^{ab}$ is given in Figure 7.3 as a function of particle energy using a plasma density typical of Proto-MPEX $n_b = 4\times10^{19} m^{-3}$. The green area represents the range of mirror-to-mirror lengths L_m found in Proto-MPEX (0.1 to 1 meters). For typical helicon discharges, the electron temperature ranges between 2–4 eV; if we assume a similar ion temperature, the scattering collision mean free paths $\lambda_{\perp}$ for electron-electron, electron-ion and ion-ion are in the order of a few centimeters. When compared to the mirror-to-mirror lengths, these estimates indicate that the helicon plasma transport should behave gas-dynamically and thus exhibit an isotropic Maxwellian distribution function. On the other hand, for particle energies above 100 eV, the calculations in Figure 7.3 indicate that adiabatic transport effects should become important. In Proto-MPEX this is likely to occur during ion and electron cyclotron heating experiments as investigated in reference [95].

7.4.1 Plasma leak rate from a mirror trap in the Gas-dynamic regime

To analytically derive an expression for the plasma loss rate $S_{\|}$ out of a magnetic mirror trap, the magnetic field is assumed to be uniform everywhere inside the trap and then increases abruptly like a step-function at the locations of the magnetic mirrors [103]. Inside the magnetic trap, the distribution function is isotropic and Maxwellian due to collisions. However, within one mean free path, $\lambda_{\perp}$, of the magnetic mirrors, particles inside the loss cone are not confined and this region becomes fully depleted. Hence, the distribution function $f(u_{\|},u_{\perp})$ develops a small but finite anisotropy within one mean free path of the mirrors. Far enough from the mirrors, collisions fill in the loss cone and restore isotropy in the distribution function. The plasma loss rate through a single mirror is calculated by integrating $f(u_{\|},u_{\perp})u_{\|}$ over the loss cone region within on mean free path of the mirror as described in Ref. [103]. The result of this integration is given by Eq. (7.15), which describes the plasma loss rate $S_{\|}$ (in particles per second) out of a single magnetic mirror in the Gas-dynamic regime, where $\bar{u} = \left(8kT/\pi m\right)^{1/2}$ is the mean plasma velocity, n is the plasma density inside the magnetic trap, A_0 cross sectional area of plasma inside the magnetic trap and R the mirror ratio.

$$S_{\|} = \frac{n\bar{u}}{4}\frac{A_0}{R}, \tag{7.15}$$

Eq. (7.15) indicates that the usual particle flux from a Maxwellian distribution is reduced by the factor A_0/R, which represents the decrease in the plasma cross-section by the magnetic

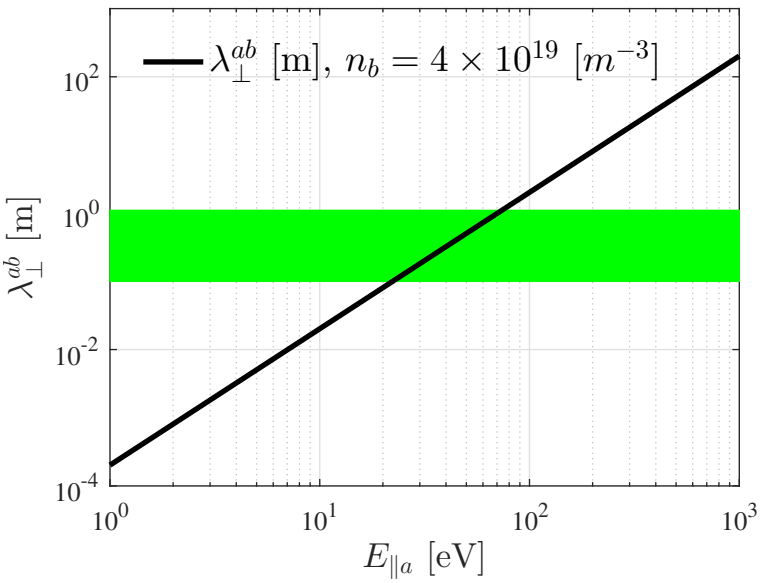

Figure 7.3: 90-degree scattering mean free path for particles “a" on background species “b" as a function of particle kinetic energy. Green area represents the range of mirror-to-mirror lengths in Proto-MPEX

mirror. The factor $1/R$ can be viewed as the fraction of particles from inside the mirror trap, which are not reflected by the magnetic mirror.

7.5 Mirror effects on low temperature helicon plasma

Measurements near the helicon source have shown that the plasma temperature typically produced is between 3-4 eV. These low temperature plasmas are collisional, isotropic, and Maxwellian. The collisional helicon plasma in Proto-MPEX will still experience the effects of mirror force. This slowing down of the particles with the presence of a high B-field has been observed in tandem devices [104], despite the mean free path of the particles ($\lambda_{\perp}^{e,i}$) being much less than the mirror length (L_m).

When diffusion time out of the loss cone is shorter than the transit time the loss cone is filled, $\frac{\lambda}{R} \ll L$, but when the transit time is $\ll$ diffusion time, the loss cone is nearly empty. In such case, there is a weak dependence of axial confinement time ($\tau_{\parallel}$) and the mirror ratio (R). The linearly proportional relationship between the mirror ratio and the axial confinement time [100, 103] is shown in Eq. (7.16),

$$\tau_{\parallel} = \frac{1}{2\alpha}\frac{RL}{c_s} \tag{7.16}$$

where c_s is the ion acoustic sound speed $\sqrt{k(T_i+T_e)/m_i}$, α is a ratio of the end loss current density at the mirror throat to the current density at the mid-plane. From the equation it should be noted that the confinement time increases linearly with R and L, and decreases with $T^{1/2}$, and is independent of the density. $\tau_{\parallel}$ represents the characteristic decay rate of the plasma via convective losses. Using the particle conservation equation and assuming that losses are via the throats of the discharge, the conservation equation can be written as in Eq. (7.17),

$$\frac{\partial n_e}{\partial t} + \frac{n_e}{\tau} = G \tag{7.17}$$

G is the particle generation rate (also in Eq. 3.18). The solution to the first-order ODE is the following,

$$n_e = n_{e0}\exp\left(-\frac{t}{\tau}\right) + \int G(t')\exp\left(\frac{t'-t}{\tau}\right)dt', \tag{7.18}$$

and assuming constant generation rate we get,

$$n_e \approx n_{e0}\exp\left(-\frac{t}{\tau}\right) + Gt \tag{7.19}$$

The equation shows that the density leakage leads to an exponential decay while the particle generation leads to a linear increase in density.

7.5.1 Experimental observation of Gas-dynamic transport

Gas-dynamic transport effects have been observed in Proto-MPEX when operating with helicon-only plasmas. The experimental results are reported in this subsection.

The experimental setup is shown in Figure 7.4. A deuterium helicon plasma (90 kW at $f =$ 13.56 MHz, 500 ms long RF pulses) is generated inside the magnetic mirror trap in the region $1.5 < z < 2$ m which diffuses along the magnetic field to the other regions of the device. Two Double Langmuir Probes (DLP1 and DLP2) [55] are positioned on axis at each end of the device as shown in Figure 7.4 to measure the plasma density n_e and electron temperature T_e. A fast pressure gauge is placed near the target to measure the neutral deuterium gas pressure (P_{D_2}). In Proto-MPEX, P_{D_2} has been shown to be proportional to the total plasma flux ($\int \Gamma_2 dA$) arriving at the target region [95].

The variable magnetic mirror was systematically changed as shown in Figure (7.4) to control the mirror ratio R and thus the plasma transport from the plasma source to the target where DLP 2 is located. The peak of the field at the variable magnetic mirror and the minimum field at the plasma source are used to define the mirror ratio R. During the mirror ratio R scan, the B_0 at the location of DLP1 and DLP2 remains constant ($B_0^1 = 0.23$T and $B_0^2 = 0.3$T respectively), hence, the plasma cross sectional area A at DLP1 and DLP2 remains unchanged; As a result, the plasma leak rate at each end of the device ($n_e \bar{u} A_i$) is dependent mostly on the plasma density.

The plasma density measurements at the plasma source (DLP1) and the target region (DLP2) as a function of R are shown in Figure 7.5. The most important aspect to notice is the linear trend of both measurements with mirror ratio R. Similarly to the target n_e, P_{D_2} also decreased inversely with R (see Figure 7.6), which indicates that the total particle flux reaching the target is was reduced.

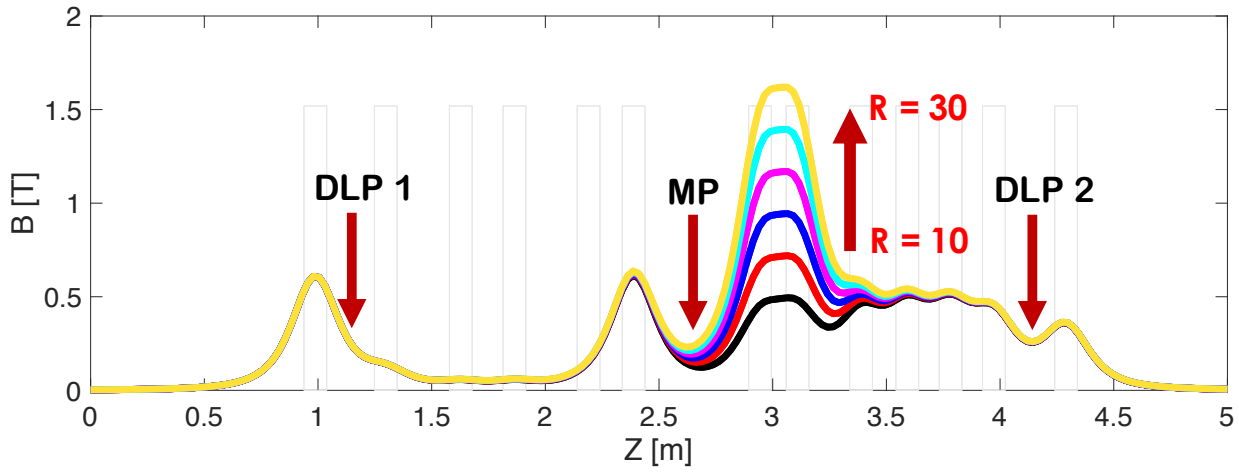

Figure 7.4: The axial magnetic field indicating the location where the B scan was occurring. Double Langmuir probes (DLPs) 1 and 2 measured n_e near the source and the target.

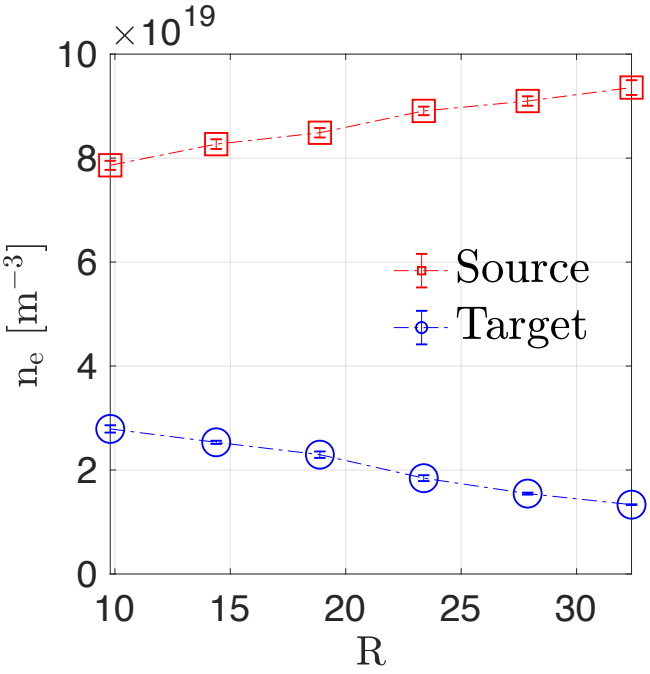

Figure 7.5: n_e as a function of mirror ratio (R) measured near the source location (red), and near the target region (blue).

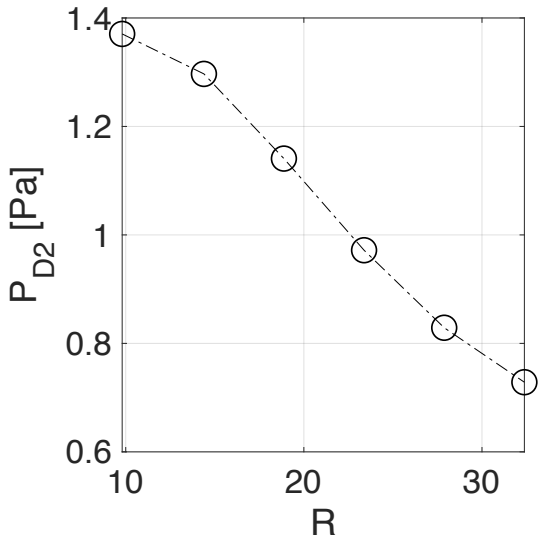

Figure 7.6: Neutral gas pressure (P_{D_2}) measured as a function of mirror ratio R near the target location.

The interpretation is the following: the linear trend of plasma density and total particle flux with the mirror ratio, R, is indicative of Gas-dynamic transport since it scales as 1/R. Increasing the mirror ratio R reduces the plasma transport towards the target region hence causing a reduction in the plasma density and particle flux. Moreover, the reduction in plasma transport towards the target region leads to accumulation of particles in the plasma source region from mass conservation.

7.5.2 Gas-dynamic model

A simple gas dynamic model was created to validate the observed trend during the experiment. The purpose of the model was to predict the confined electron density at the source region using the target density measurement. Beginning with the conservation equation, where the total number of particles generated within the volume is balanced by the plasma leak rate in the steady state is given by Eq. (7.20),

$$\int \nabla \cdot \mathbf{\Gamma} dV = \int G dV \tag{7.20}$$

Using the divergence theorem, Eq. (7.20) becomes,

$$\int \mathbf{\Gamma} dA = \int G dV \tag{7.21}$$

The total generation rate is denoted as S_+, which is given by

$$S_+ = \int G dV. \tag{7.22}$$

The particle transport is considered to be all in the parallel direction and the radial transport is assumed to be negligible. Plasma escapes the confined region through the mirror throats; therefore the total number of particles is given by,

$$\int \Gamma dA = \Gamma_1 A_1 + \Gamma_2 A_2, \tag{7.23}$$

and the particle conservation equation becomes,

$$\Gamma_1 A_1 + \Gamma_2 A_2 = S_+. \tag{7.24}$$

To proceed, an assumption that the plasma generation rate at the source is constant is made during the magnetic field scan, which indirectly observed by the minuscule variation of the neutral gas pressure at the source, as shown in Figure 7.7. In other words, during the magnetic

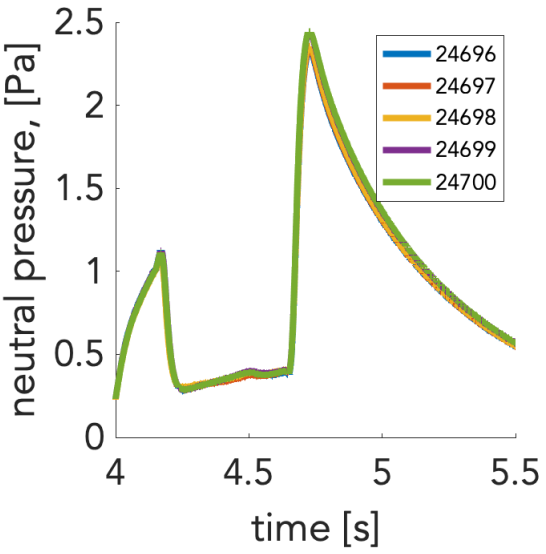

Figure 7.7: Neutral gas profile at the source location stays relatively the same during the mirror ratio scan. A subset of the number of shots is chosen here for representation.

field scan, the particle generation rate remains fixed (i.e. $S_+ =$ constant; thus using Eq. (7.24) one obtains,

$$\Gamma_1 A_1 + \Gamma_2 A_2 = \Gamma_1^0 A_1 + \Gamma_2^0 A_2. \tag{7.25}$$

here subscripts 1 and 2 represent source and target parameters respectively, and superscript 0 represents the initial condition. Substituting $\Gamma = nc_s$ in Eq. (7.25) one gets,

$$n_1 c_{s1} A_1 + n_2 c_{s2} A_2 = n_1^0 c_{s1}^0 A_1 + n_2^0 c_{s2}^0 A_2 \tag{7.26}$$

$$n_1 = n_1^0 \frac{c_{s1}^0}{c_{s1}} + \frac{\left(\mathrm{n}_2^0 c_{s2}^0 - \mathrm{n}_2 c_{s2}\right)}{c_{s1}} \frac{A_2}{A_1} \tag{7.27}$$

Assuming the flow does not change at the source gives,

$$n_1^i = n_1^0 + \frac{\left(\mathrm{n}_2^0 c_{s2}^0 - \mathrm{n}_2^i c_{s2}\right)}{c_{s1}} \left(\frac{B_1}{B_2}\right)^i, \tag{7.28}$$

here superscript 'i' is the ith term during the mirror scan. Following standard error is obtained in the source density due to uncertainty in the magnetic field at the source location, the heating section, as well as flow velocities at their respective locations,

$$\sigma_{n_1} = \frac{\left(\mathrm{n}_2^0 c_{s2}^0 - \mathrm{n}_2 c_{s2}\right)}{c_{s1}} \left(\frac{B_1}{B_2}\right) \left(\left(\frac{\sigma_{B_1}}{B_1}\right)^2 + \left(\frac{\sigma_{B_2}}{B_2}\right)^2 + \left(\frac{\sigma_{c_1}}{c_1}\right)^2 + \left(\frac{\sigma_{c_2}}{c_2}\right)^2 \right)^{\frac{1}{2}} \tag{7.29}$$

Using Eq. (7.28), n_e at the source from Figure 7.5, Figure 7.8 is obtained. The figure shows the plot of experimental density (black) and the theoretical model (red) at the source region as a function

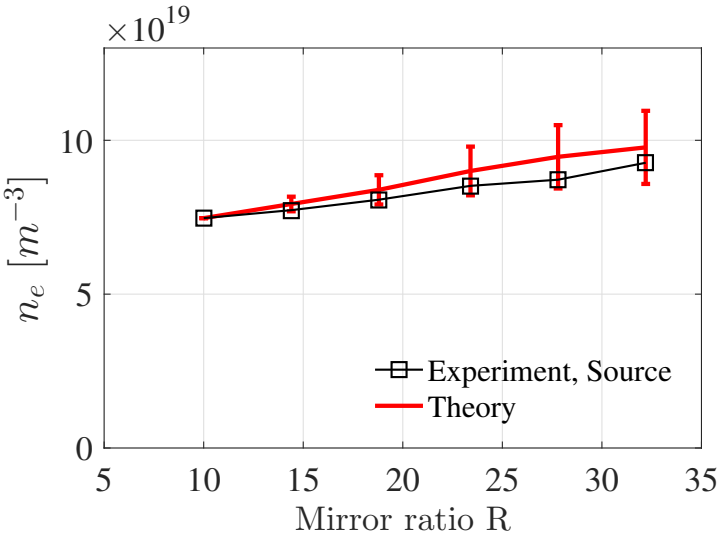

Figure 7.8: Comparison between n_e at the source region obtained experimentally (black) and using the collisional confinement model (red) is shown as a function of the mirror ratio (R).

of R. The initial input data in the model is the initial experimental value at R = 10, where the second term in Eq. (7.28) cancels itself; therefore, no uncertainty is added to the initial data point. The two plots follow the trends of the linear increase in n_e as a function of R, and the values are also comparable.

7.6 Magnetic mirror effect during ion cyclotron heating

The previous section focused on low temperature plasmas experiencing Gas-dynamic transport in Proto-MPEX. As discussed earlier, particles gain energy with the application of auxiliary heating in Proto-MPEX. Energized particles with subsequent collisions with the background plasma increases the temperature of the bulk plasma. However, ICH leads to resonant interaction that adds $u_\perp$ to particles. The resonant frequency is given by,

$$\omega_i = \frac{qB}{m_i}, \tag{7.30}$$

where q is the electric charge, and m_i is the mass of the ion. The 90° scattering mean-free path of the energetic particles also increases, and the particles get trapped within the mirror; such particles bounce between mirrors. Energetic particles experience $\mu\nabla B$ mirror force and are kinetically confined [103]. This section presents experimental results from deuterium helicon plasmas (90 kW, 500 ms long pulses) with ICH (5-25 kW), where the influence of magnetic mirrors is studied primarily using plasma flow behavior using Mach probe (MP). Mach probes are typically placed perpendicular to B_0 in Proto-MPEX, where one tip collects the upstream ion saturation current (J_u), and the other tip collects the downstream ion saturation current (J_d). The probe

head itself shadows the downstream tip, and the ratio of J_u to J_d is used to obtain M, as shown in Eq. (7.31),

$$M = \frac{1}{k} \ln\left(\frac{J_u}{J_d}\right), \tag{7.31}$$

where k is the calibration factor, and k = 1.66 is used for the magnetized probe for this study [61].

Experiments were conducted with 6.5 MHz–ICH to study the axial flow behavior using MP. The probe was placed upstream of the variable magnet and the ICH antenna, as shown in Figure 7.9. Two experiments were conducted to study the influence of magnetic mirrors with ICH. The first experiment measured M as a function of ICH power, in which the helicon source parameters and the magnetic field were kept constant. The thick red B plot in Figure 7.9 represents B used for the ICH power scan. For the second experiment, the variable magnet was systematically raised, as shown in Figure 7.9. The ICH power and the helicon source conditions were kept constant during the B scan. M was measured for helicon-only and helicon + ICH plasma discharges. The results from these two experiments are discussed next.

During the ICH power scan experiment, a temporal MP profile was investigated (see Figure 7.10a) using the raw signal collected by two MP tips. The temporal profile consists of the saturation current collected by two tips before, during, and after ICH power injection. The blue trace in Figure 7.10a represents injected ICH power (P_{ICH}) during the discharge. The important phenomenon to note here is that current on J_d substantially increased during ICH, while J_u showed negligible change. The observation indicates that plasma streaming from the ICH region caused J_d to increase. The increased J_d disappeared when the ICH power was turned off. From the second experiment (Figure 7.10b), reduction in M as a function of ICH power was observed. Increase in the ICH power correlate to the reduction of the plasma flow close to the magnetic mirror.

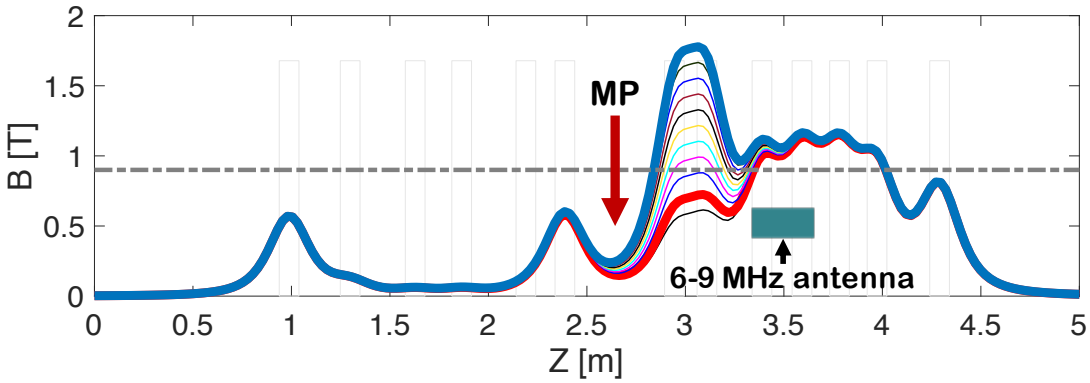

Figure 7.9: ICH resonance region in Proto-MPEX for the ICH frequency of 6.5 MHz. The dashed line indicates the resonant B of 0.9 T for 6.5 MHz RF injection.

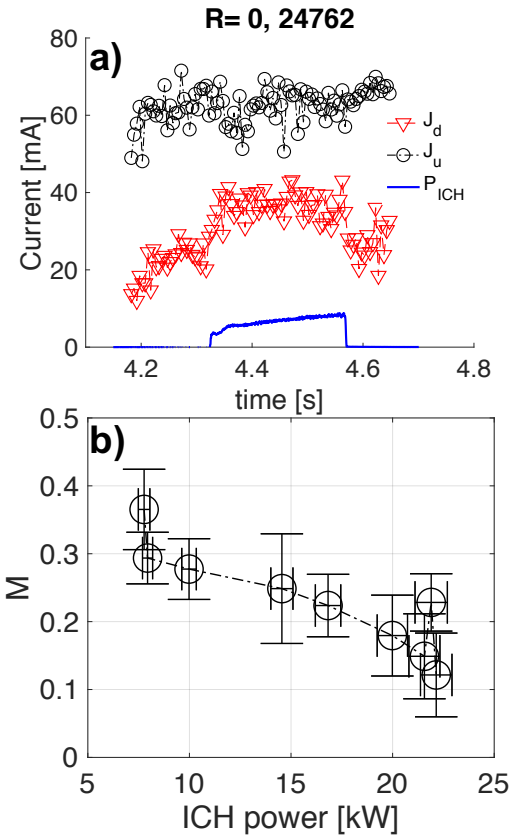

Figure 7.10: Figure (a) shows the temporal current collected by the two Mach probe tips (upstream (black) and downstream (red)) before, after and during ICH power injection. Figure (b) shows the Mach number as a function of the ICH power.

The mirror ratio scan conducted with helicon-only and helicon + ICH is presented in Figure 7.11. The figure shows M as a function of R for helicon-only (black), and helicon with ICH (red). The measurement during the helicon showed some drop in the plasma flow with R, but there was a considerable drop in the M immediately after the ICH power was injected. M continued to decrease with R until $R \sim 31$. However, increasing R further showed an increase in M to ~ 0.5, which was also measured during helicon discharge for the same R. Analyses of the observed results during ICH is made next.

ICH injection at the mirror throat has been used in various devices to trap the plasma particles [105, 96]. Both the ICH power scan and the ICH mirror ratio scan suggest plasma slowing down during ICH coupling in Proto-MPEX. The flow pattern indicates that at the upstream resonance region, highly energized ions increase λ_i; therefore particles could be experiencing adiabatic confinement at higher magnetic fields. Raising the B higher during the R scan reached a critical point which removed the upstream ICH resonance field. The magnetic field near the ICH antenna does not cross the resonant B of 0.9 T (dotted-line) at z $\sim$3.2 m (Figure 7.9), which is represented by outermost (thick-blue) field line. When the ICH resonance coupling was removed from the plasma column in the upstream side, the Mach probe measured higher M. This

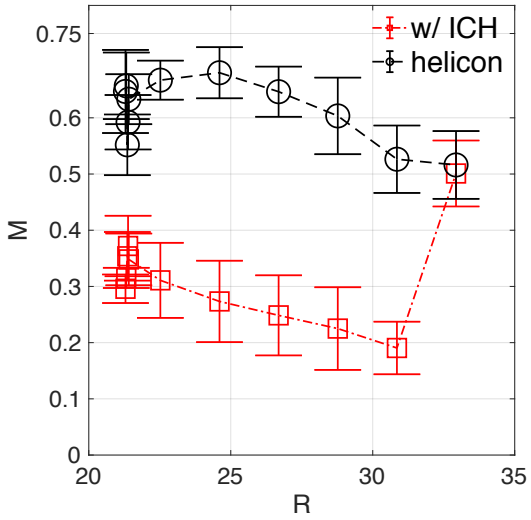

Figure 7.11: Flow measurement taken at the central chamber shows Mach Number, M, as a function of the mirror ratio, R during ICH (red), and during helicon (black).

phenomenon points towards strong adiabatic force slowing down the plasma as long the as the ICH power is coupled to the plasma.

7.6.1 Influence of mirrors on the power deposition on the target with EBW

Power deposition on the target is one of the direct measurements to evaluate the efficiency of the heating mechanism and the magnetic geometry. IR thermography is typically used for in-situ measurement of the target temperature. The measurement is calibrated against known black body radiation with a known emissivity to obtain an accurate temperature measurement of the target plate [106]. Temperature information is deduced further to obtained power and heat flux on the target. The efficiency of EBW is investigated by scanning the magnetic field between the heating section and the target. The source power, the neutral gas input, and the EBW power were kept constant during this experiment. The field profile during the PS2 current scan is shown in Figure 7.12c. The total energy on the target surface was measured during the magnetic field scan for both the helicon only and helicon with EBW discharges, and also simultaneously measuring the corresponding peak heat flux on the target. A magnetic flux cross-sectional area normalization was necessary because the magnetic field varied at the target during the scan due to the flux compression.

Figures 7.12a and 7.12b shows the total energy and peak heat flux on the target as a function of B-field at the target location [95]. The shaded area in Figures 7.12a and 7.12b show the field values of the overhill and downhill field conditions. During the helicon discharge, a minimal decrease in the total energy (black) and the peak heat flux (black) was measured. With the addition

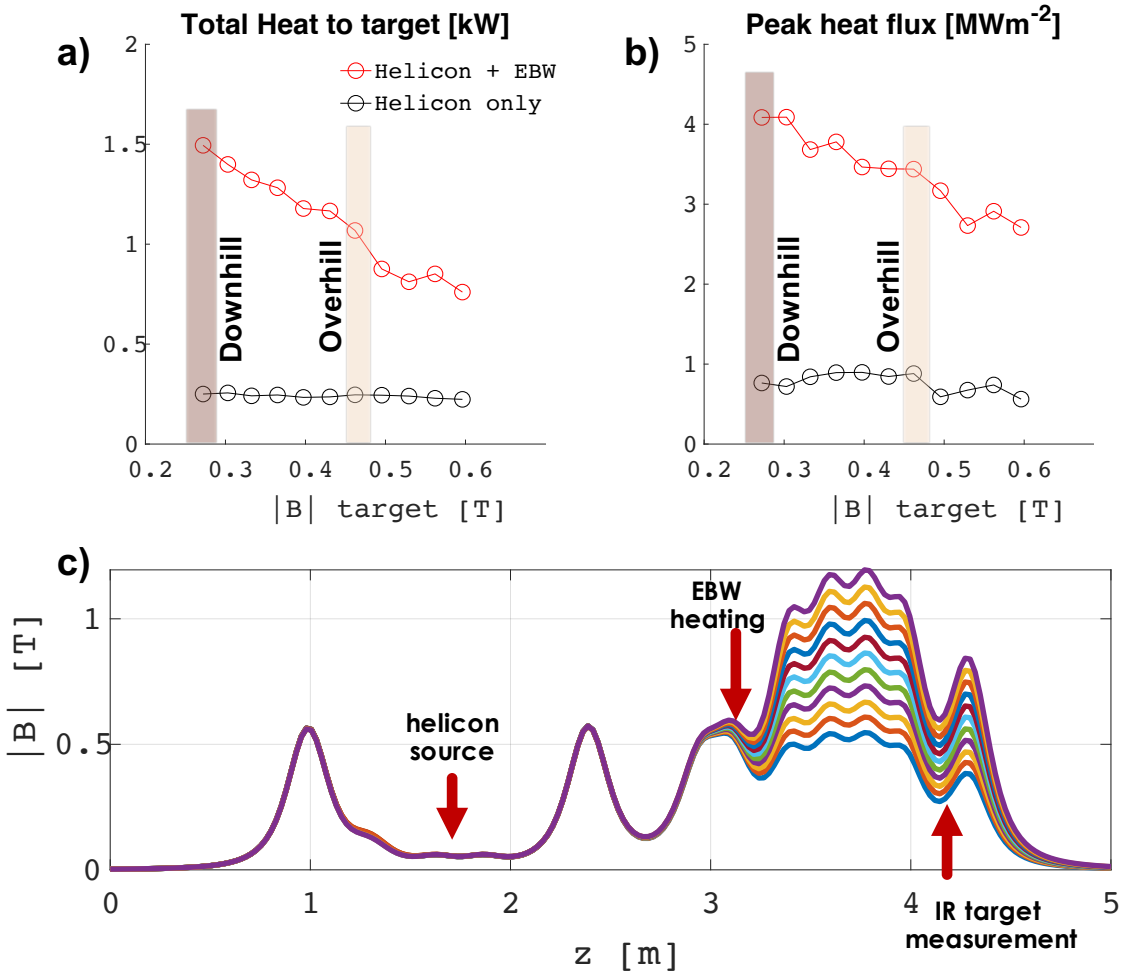

Figure 7.12: The figure shows measurement conducted using IR thermography, where the plot (a) total heat/energy received at the target as a function of the B. Total energy is normalized to the cross-sectional area of the flux tube. (b) shows the peak heat flux at the target again as a function of B. Measured peak heat flux value is irrespective of the flux tube expansion or compression. Black circles in (a) and (b) are for the helicon only discharges, and red circles are with the addition of EBW. The bottom figure (c) shows the scan of the axial magnetic geometry where B between 28 GHz launcher and the target. The data points where the overhill and downhill field conditions lie is also identified.

of EBW the total energy (red) increased from about 0.25 kW to 1.5 kW at low magnetic field; similarly, the peak heat flux (red) increased from ∼0.9 [MWm^{-2}] to 4 [MWm^{-2}]. However, with increasing B-field, both the energy and the peak heat flux decreased much more prominently with EBW then with the helicon discharge. The total average power between the overhill and downhill configurations show that Proto-MPEX during downhill configuration showed higher power and energy on the target surface than in the overhill conditions, which is further evidence of the magnetic mirrors affecting the transport.

7.7 Summary

This chapter focused on plasma transport in the presence of magnetic mirrors. A recent magnetic reconfiguration has allowed the capability to locally change the field in Proto-MPEX without affecting the magnetic field in the plasma source and the target regions. The parallel plasma transport in Proto-MPEX is studied by systematically changing the magnetic configuration for two plasma conditions: (1) helicon-only, (2) helicon + ICH, and (3) helicon + EBW. Increasing the magnetic mirror ratio shows that the low-temperature helicon-generated plasma is Gas-dynamically confined by the magnetic mirror. For the energetic ion and electron population with the injection of auxiliary heating adiabatic kinetic mirror trapping confines the plasma. Both of these transport effects have been observed in Proto-MPEX. The low temperature collisional trapping was observed by measuring n_e, which was further analyzed using a simple Gas-dynamic model. Additionally, plasma flow measurements using Mach probes have shown a decrease in Mach number as a function of the mirror ratio. Plasma flows were further investigated with auxiliary ICH.

Results with the addition of ICH measured upstream of the antenna has shown a decrease in M as a function of the R compared to the helicon-only discharge. Such flow behavior demonstrated plasma slowing down due to increased reverse plasma flow towards the helicon antenna. However, in a high magnetic field, when the resonant magnetic field for the ion energy coupling from ICH was removed from the upstream side, no effects of ICH was observed. Results have shown that plasma transport in Proto-MPEX exhibits has Gas-dynamic transport for helicon generated plasma, but the addition of auxiliary ICH leads to the mirror force affecting the plasma upstream of the antenna. MPEX will have designed flexibility to vary the magnetic field that will allow B_0 of up to 2.5 T. For the EBW resonance coupling at higher B_0, the particle confinement in the helicon source region will increase. Besides, the magnetic field in MPEX design should consider keeping the ICH resonance coupling downstream of the RF antenna without influencing the upstream plasma transport.

Chapter 8

Conclusion and Future Work

8.1 Conclusion

The Prototype Material Plasma Exposure eXperiment at Oak Ridge National Laboratory has successfully produced high electron density plasma discharges using helicon waves. The high electron density ($> 1 \times 10^{20}$ particles/m^{-3}) produced in Proto-MPEX is one of the highest ever produced using helicon power and light ions. The plasma produced is transported towards a material target at the end of the device through a convoluted path consisting of several magnetic mirrors and heating systems. Work presented here provided an in-depth analysis of the transport of the helicon plasma discharges with and without the addition of EBW for electron heating and ICH for ion heating. Upgrades to Proto-MPEX diagnostics (listed in Chapter 3) have enabled the transport characterization. Three key diagnostics that were vital to the transport study and also to MPEX were discussed in the previous chapters 3 and 4. This chapter presents some of the major conclusions along with implications for plasma transport in MPEX. Proto-MPEX uses old and new physics and technologies to prepare its power sources for MPEX, and this chapter also suggests some future experiments for Proto-MPEX.

8.1.1 Mach-double Langmuir probe and Thomson scattering installation

Installation of new diagnostics is a significant accomplishment that enabled the study of the parallel transport behavior in Proto-MPEX. The building of Mach double Langmuir probes provided comprehensive diagnostics coverage of the plasma temperature, density, and flow at multiple locations along the length of the device. Mach probes were developed as part of this research and utilized in Proto-MPEX to measure plasma flows, which were essential measurements for comparisons with computational modeling and to study the effects of magnetic mirrors.

An upgrade of the Thomson scattering diagnostic system improved it from a single-pass low spatial resolution radial measurement to a dual-pass higher spatial resolution radial measurement. Moreover, the upgrade enabled simultaneous measurement of the radial distribution of the electron density and electron temperature with a higher spatial resolution at two key axial locations (the electron heating section at the central chamber and the target). Moreover, the Thomson scattering system upgrade was mandated to replace the use of perturbative probes, which typically distort the plasma at the downstream locations. Moreover, double Langmuir probes at the central chamber were vulnerable to damage during the high heat flux EBW injections and were unable to provide proper measurement; Thomson scattering enabled measurement of increased temperature with EBW at the central chamber. Those results were presented in Chapter 6. Demonstrating the capability of recycling the Thomson laser for multiple passes will be useful for the MPEX device, which is planning to rely heavily on spectroscopic and optical diagnostics. MPEX, which will be a steady-state system, will need constant monitoring of the source and target conditions during PMI studies.

Future work: Previously, an attempt had been made to measure the ion flow velocity using a spectroscopic technique, but with a small tangible result. The Mach probe measurements sometimes are found to overestimate the flow, especially in a high magnetic field with short connection length. Further study of the flow with the spectroscopy will provide a secondary validation to the results presented here. Moreover, experiments to analyze radial flow measurement is needed to identify the presence of a radial shear flow or a radial flow reversal. Thomson scattering diagnostics struggled with the stray light to take measurements close to the target. Other techniques such as Schlieren imaging systems could be considered as an alternative.

8.1.2 Convective heat transport dominant in Proto-MPEX

Analytical calculations have shown the helicon plasma to be highly collisional, isotropic, and Maxwellian. The collisional mean free path analysis is shorter than the length between the magnetic mirrors. The helicon plasma can, therefore, be treated with fluid plasma properties, and the experimental parameters obtained along the axial length of the device enabled data-constrained B2.5-Eirene fluid model to be implemented. B2.5-Eirene was built to model scrape-off-layer transport in toroidal plasma geometry, which uses the governing fluid equations of conservation of mass, momentum, and energy. This work presented one of the first results from Proto-MPEX comparing experimental and modeling results.

Both the experiment and the model show a stagnant and conductively transported plasma in the vicinity of the plasma source, while there is a a pressure-driven convective plasma away from the source. A qualitative agreement between the two methods was observed with some discrepancy near the targets. B2.5-Eirene is predicting low electron temperature, which was consistent with the experimental measurement, but also low electron density near the target. The prediction of the low density was inconsistent with the experimental observation. Low

temperatures and densities are a typical indication of detached plasma, but experimentally this has not been observed.

Future work: A strong D_α single is measured by the filterscopes and a bright plasma light by the visible camera is observed very close to the target. The light emission does not extend out to the distance predicted by the model. B2.5-Eirene was built for modeling tokamak fusion plasma where the electron temperature is an order of magnitude higher than in Proto-MPEX. When the plasma temperature gets ∼1 eV, the cross-section for the volumetric recombination and charge exchange increases. Additional data-constrained B2.5-Eirene model could be implemented in the future with improved neutral gas management and with higher target temperature (with auxiliary heating) to enhance the near target predictions.

8.1.3 Helicon with EBW auxiliary heating

With the injection of EBW heating in the new upgraded Proto-MPEX configuration, electron temperature increased at the heating location, and a rise in the core electron temperature was measured at the target region as well. The electron density, however, drops during EBW heating downstream of the heating location and increases slightly at the source location. The understanding of the physics of density drop is an ongoing process to date.

A small gradient in the electron temperature exists for helicon-only and helicon with EBW discharges. The small temperature drop with EBW only appears in the region between the launcher and the target. There is a sharp drop in the temperature upstream of the launcher because the EBW power is directed to couple with the plasma moving towards the target. The electron temperature in Proto-MPEX with isothermal plasma for both helicon and helicon with EBW with little to no density rise near the target could be considered to be operating in the sheath-limited regime. Moreover, convective heat transport dominates in both cases.

The efficiency study of two magnetic field geometries for the EBW injection was considered. These magnetic field geometry were colloquially referred to as *overhill* and *downhill* (described in Chapter 2). Comparing the two conditions, downhill geometry was more efficient because of the higher heat flux on the target due to the flat or downward directed magnetic field.

Future work: A recent experiment with 20% helium gas has been conducted for preliminary PMI studies in Proto-MPEX. Using the mixture of deuterium and helium fuel has provided phenomelogical evidence of the density rise near the target, which could lead to the conduction-limited regime. Presence of CLR is purely speculative yet, but it could be valuable to identify the physics that could achieve CLR in Proto-MPEX, which will eventually be useful for the MPEX device.

8.1.4 Magnetic mirrors choke the plasma in Proto-MPEX

In the 60s and 70s, linear fusion devices used magnetic mirrors as plugs for fusion reactions, but the feasibility of toroidal devices outweighed the possibility of fusion in linear devices. However, there is an established physics understanding of the particle confinement within magnetic mirrors. The severity of the magnetic mirrors in Proto-MPEX was unknown until this study was conducted. Proto-MPEX requires several magnetic mirrors for the proper operation of the power sources, and the mirrors add complexity to plasma transport; even for the helicon generated collisional and isotropic plasmas. A Gas-dynamic trap model was built to compare the trapping on the helicon plasma. The model was able to predict the linearly increasing plasma confinement with the rising mirror ratio.

Additionally, plasma flow measurements using Mach probes have shown a decrease in the flow as a function of the magnetic mirror ratio. Plasma flows investigated further with ICH heating, showed an increase in the flow from the ICH antenna to the helicon source, hence, decreasing M upstream of the ICH resonance. Plasma flow was reduced as a result of higher mirror ratios and also with higher injected ICH power due to the adiabatic forces.

8.2 Implications for MPEX plasma transport

Mirror effects in MPEX

There are several implications with the presence of the magnetic mirrors in MPEX. Figure 8.1 shows the axial magnetic field geometry in MPEX along with the position of the helicon antenna, location of the ECH/EBW waveguide, two ICH antenna, and the target locations. The 2nd harmonic EBW with 70 GHz ECH will use 1.25 T (black), while the 70 GHz whistler wave will use 2.5 T (red). The magnetic field downstream of the EBW antenna is the preferred field geometry which will aid the efficient transport of plasma towards the target. Using the 1.25 T field at the EBW launcher will produce a mirror ratio of about 12-13, which is nominal to the mirror ratio present in Proto-MPEX. However, choosing the 2.5 T field will increase the mirror ratio to 34-35, which will increase Gas-dynamic confinement in the helicon source region. In such scenario, increasing the helicon power will be warranted to obtain the same throughput as operating at 1.25 T. To make use of the knowledge of the mirror physics in Proto-MPEX, a taller asymmetric mirror upstream of the helicon antenna could be considered to limit the power loss to the dump plate. About 9.1% of power ends up at the dump plate in Proto-MPEX. Collisional confinement can be used to MPEX's advantage if the particles leak rate can be reduced to the dump plate with a bigger mirror.

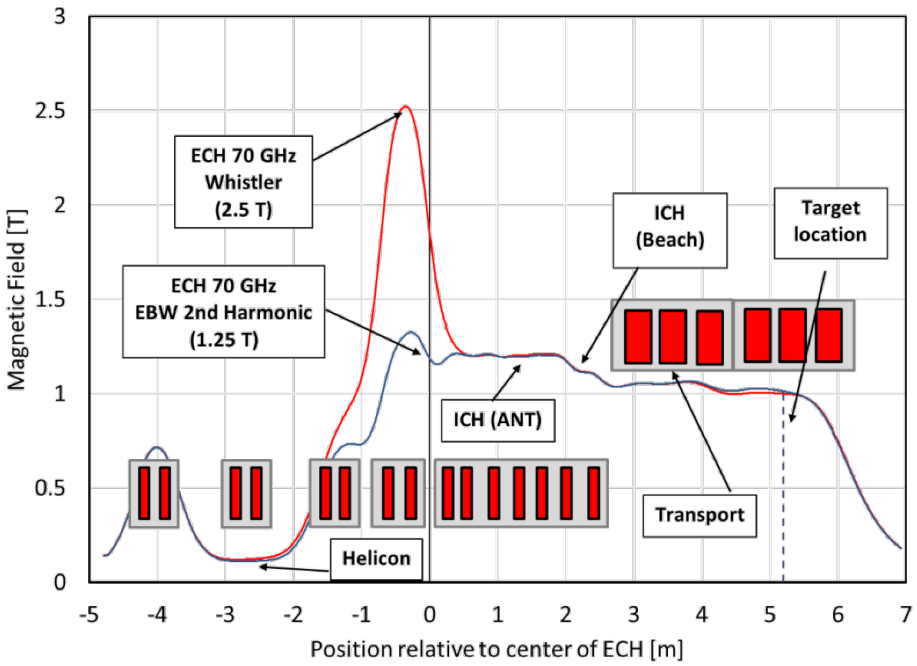

Figure 8.1: Magnetic field profile in MPEX for second harmonic EBW heating (black), and ECH (Whistler) heating (red).

Gas puffing in the target region

Two essential methods to move from the sheath-limited regime to conduction-limited regime is to increase the *plasma collisionality* between the upstream and the target region, and increase the *electron density* at the target region. An attempt was made in Proto-MPEX to puff neutral gas at the target to induce a density increase, and also to detachment. However, the gas puff was not able to penetrate the plasma column and remained localized to the region of injection. A use of supersonic nozzles to puff the neutral gas into the core of the plasma column in MPEX could lead to a decrease in parallel electron temperature. Thus a finite temperature gradient will increase the parallel heat conduction and also increase electron density due to ion-neutral or electron-neutral collisions.

In summary, the Prototype Material Plasma Exposure eXperiment at Oak Ridge National Laboratory has been instrumental in the helicon plasma and auxiliary heating sources development for MPEX user facility. Understanding the transport of plasma heat and particles in Proto-MPEX has provided useful insight into the delivery of the desired power envisioned in MPEX. MPEX will conduct plasma material interaction experiments for the future fusion reactors, which fits into the larger goal of advancing human endeavors of obtaining carbon-free energy for the future.

Bibliography

[1] K. Saidi and S. Hammami, "The impact of CO2 emissions and economic growth on energy consumption in 58 countries," *Energy Reports*, vol. 1, pp. 62–70, 2015. [Online]. Available: http://linkinghub.elsevier.com/retrieve/pii/S235248471500013X 1

[2] R. A. Begum, K. Sohag, S. M. S. Abdullah, and M. Jaafar, "CO2 emissions, energy consumption, economic and population growth in Malaysia," *Renewable and Sustainable Energy Reviews*, vol. 41, pp. 594–601, 2015. [Online]. Available: http://linkinghub.elsevier.com/retrieve/pii/S1364032114006650 1

[3] J. P. Freidberg, *Plasma physics and fusion energy*. New York: Cambridge University Press, 2007, vol. 1. [Online]. Available: http://books.google.com/books?hl=en{&}lr={&}id=Vyoe88GEVz4C{&}oi=fnd{&}pg=PA3{&}dq=Plasma+physics+and+fusion+energy{&}ots=YvnpbizFsX{&}sig=Cu0BZ0VcBGR0LHPrYF0bJZRR3KQ 1

[4] F. F. Chen and G. J. Weisel, *An Indispensable Truth: How Fusion Power Can Save the Planet*. Springer International Publishing, 2011, vol. 79, no. 12. [Online]. Available: http://link.aip.org/link/AJPIAS/v79/i12/p1276/s1{&}Agg=doi 1

[5] CambridgeCore, "Fusion energy," 2016. [Online]. Available: https://www.cambridge.org/core/journals/mrs-energy-and-sustainability/article/fusion-energy/76200CCBE025A62F5FAC0F490060ABFD/core-reader 2

[6] T. J. Dolan, *Magnetic Fusion Technology*. London: Springer, 2013, vol. 19. 2, 5, 21, 24

[7] C. E. Bush, S. A. Sabbagh, S. J. Zweben *et al.*, "Deuterium-tritium high confinement (h-mode) studies in the tokamak fusion test reactor," *Physics of Plasmas*, vol. 2, no. 6, pp. 2366–2374, 1995. [Online]. Available: https://doi.org/10.1063/1.871490 3

[8] A. Gibson, "Deuterium-tritium plasmas in the Joint European Torus (JET): Behavior and implications," in *Physics of Plasmas*, vol. 5, no. 5, 1998, pp. 1839–1847. 3

[9] ITER, "What is ITER?" 2018. [Online]. Available: https://www.iter.org/proj/inafewlines 3

[10] K. Ehrlich and A. Möslang, "IFMIF - An international fusion materials irradiation facility," *Nuclear Instruments and Methods in Physics Research Section B: Beam Interactions with Materials and Atoms*, vol. 139, no. 1-4, pp. 72–81, 1998. [Online]. Available: http://www.sciencedirect.com/science/article/pii/S0168583X97010069 3

[11] D. J. Ward, "The physics of DEMO," *Plasma Physics and Controlled Fusion*, vol. 52, no. 12, 2010. 3

[12] IAEA (International Atomic Energy Agency), "Development of Radiation Resistant Reactor Core Structural Materials," pp. 1–8, 2007. [Online]. Available: https://www-legacy.iaea.org/About/Policy/GC/GC51/GC51InfDocuments/English/gc51inf-3-att7_en.pdf 3

[13] M. J. Baldwin, R. P. Doerner, W. R. Wampler *et al.*, "Effect of He on D retention in W exposed to low-energy, high-fluence (D, He, Ar) mixture plasmas," *Nuclear Fusion*, vol. 51, no. 10, p. 103021, Oct 2011. 3

[14] R. Behrisch, G. Federici, A. Kukushkin, and D. Reiter, "Material erosion at the vessel walls of future fusion devices," *Journal of Nuclear Materials*, vol. 313-316, pp. 388–392, mar 2003. [Online]. Available: https://www-sciencedirect-com.proxy.lib.utk.edu:2050/science/article/pii/S0022311502015805 3

[15] S. Zinkle and L. Snead, "Designing Radiation Resistance in Materials for Fusion Energy," *Annual Review of Materials Research*, vol. 44, no. 1, pp. 241–267, 2014. [Online]. Available: http://www.annualreviews.org/doi/10.1146/annurev-matsci-070813-113627 3

[16] S. Zinkle, "Advanced materials for fusion technology," *Fusion Engineering and Design*, vol. 74, no. 1-4, pp. 31–40, 2005. [Online]. Available: http://linkinghub.elsevier.com/retrieve/pii/S0920379605004060 3

[17] J. Rapp, "The challenges of plasma material interactions in nuclear fusion devices and potential solutions," *Fusion Science and Technology*, vol. 72, no. 3, pp. 211–221, jul 2017. [Online]. Available: https://www.tandfonline.com/doi/full/10.1080/15361055.2017.1333859 5

[18] J. Rapp, T. M. Biewer, J. Canik *et al.*, "The development of plasma-material interaction facilities for the future of fusion technology," *Fusion Science and Technology*, vol. 64, no. 2, pp. 237–244, aug 2013. [Online]. Available: https://www.tandfonline.com/doi/full/10.13182/FST12-565 5

[19] U.S. BPO, "U.S. Burning Plasma Organization eNews," 2010. 5

[20] N. Ohno, "Plasma detachment in linear devices," *Plasma Physics and Controlled Fusion*, vol. 59, no. 3, p. 034007, 2017. [Online]. Available: http://stacks.iop.org/0741-3335/59/i=3/a=034007?key=crossref.4c24f51f7fb71f39071e3fed9b312e85 5

[21] J. Rapp, A. Lumsdaine, C. J. Beers *et al.*, "Latest Results from Proto-MPEX and the Future Plans for MPEX," *Fusion Science and Technology*, pp. 1–10, 2019. [Online]. Available: https://www.tandfonline.com/action/journalInformation?journalCode=ufst20https://www.tandfonline.com/doi/full/10.1080/15361055.2019.1610315 6

[22] T. M. Biewer, C. Lau, T. S. Bigelow *et al.*, "Utilization of O-X-B mode conversion of 28 GHz microwaves to heat core electrons in the upgraded Proto-MPEX," *Physics of Plasmas*, vol. 26, no. 5, p. 053508, may 2019. [Online]. Available: http://aip.scitation.org/doi/10.1063/1.5093321 6, 24

[23] C. Lau, J. F. Caneses, T. S. Bigelow *et al.*, "Evidence of electron heating at different radial locations on Proto-MPEX," *Physics of Plasmas*, vol. 26, no. 3, p. 032503, mar 2019. [Online]. Available: http://aip.scitation.org/doi/10.1063/1.5083814 6

[24] P. Piotrowicz, R. Goulding, J. Caneses *et al.*, "Computational investigation of ion cyclotron heating on proto-mpex," *Physics of Plasmas*, vol. 26, no. 3, p. 033511, 2019. 6

[25] J. Rapp, T. Biewer, T. Bigelow *et al.*, "Developing the Science and Technology for the Material Plasma Exposure eXperiment," *Nuclear Fusion*, vol. 57, no. 11, p. 116001, 2017. 8, 20

[26] P. C. Stangeby, *The plasma boundary of magnetic fusion devices*. Philadelphia: Institute of Physics Publishing Bristol, 2000, vol. 224. 9, 68, 70, 71, 72

[27] M. Baeva, W. J. Goedheer, and N. J. Lopes Cardozo, "Kinetics of Hydrogen Molecules in MAGNUM-PSI," *Plasma Science and Technology*, vol. 10, no. 2, pp. 162–169, apr 2008. [Online]. Available: http://stacks.iop.org/1009-0630/10/i=2/a=05?key=crossref.fff62a0b3aa6c80bcac6ddd6a612cc4b 9

[28] E. M. Hollmann, A. Y. Pigarov, R. Seraydarian *et al.*, "Particle balance measurements during detachment in a gas-target divertor simulator," *Physics of Plasmas*, vol. 9, no. 4, p. 1226, apr 2002. [Online]. Available: http://aip.scitation.org/doi/10.1063/1.1452103 9

[29] N. Ohno, D. Nishijima, S. Takamura *et al.*, "Static and dynamic behaviour of plasma detachment in the divertor simulator experiment nagdis-ii," *Nuclear Fusion*, vol. 41, no. 8, p. 1055, 2001. 9

[30] J. B. O. Caughman, R. H. Goulding, T. M. Biewer *et al.*, "Plasma Source Development for Fusion-Relevant Material Testing," *Journal of Vacuum Science & Technology A: Vacuum, Surfaces, and Films*, vol. 35, 2017. [Online]. Available: http://dx.doi.org/10.1116/1.4982664{%}5Cnhttp://avs.scitation.org/toc/jva/35/3 10

[31] J. Caneses, P. Piotrowicz, T. Biewer *et al.*, "Differential pumping requirements for the light-ion helicon source and heating systems of proto-mpex," *Physics of Plasmas*, vol. 25, no. 8, p. 083518, 2018. 10, 12, 72

[32] A. A. Fridman and L. A. Kennedy, *Plasma physics and engineering*. CRC Press, 2011. [Online]. Available: https://www.crcpress.com/Plasma-Physics-and-Engineering-Second-Edition/Fridman-Fridman-Kennedy-Kennedy/p/book/9781439812280 14

[33] M. Showers, P. A. Piotrowicz, C. J. Beers *et al.*, "Power accounting of plasma discharges in the linear device Proto-MPEX," *Plasma Physics and Controlled Fusion*, vol. 60, no. 6, 2018. [Online]. Available: https://doi.org/10.1088/1361-6587/aab7c8 14

[34] J. Lehane and P. Thonemann, "An experimental study of helicon wave propagation in a gaseous plasma," *Proceedings of the Physical Society*, vol. 85, no. 2, p. 301, 1965. 20

[35] S. Shinohara, "Helicon high-density plasma sources: physics and applications," *Advances in Physics: X*, vol. 3, no. 1, p. 1420424, 2018. [Online]. Available: https://www.tandfonline.com/action/journalInformation?journalCode=tapx20https://www.tandfonline.com/doi/full/10.1080/23746149.2017.1420424 20

[36] J. F. Caneses and B. D. Blackwell, "Collisional damping of helicon waves in a high density hydrogen linear plasma device," *Plasma Sources Science and Technology*, vol. 25, no. 5, 2016. [Online]. Available: https://iopscience-iop-org.proxy.lib.utk.edu/article/10.1088/0963-0252/25/5/055027/pdf 20

[37] R. H. Goulding, J. B. O. Caughman, J. Rapp *et al.*, "Progress in the Development of a High Power Helicon Plasma Source for the Materials Plasma Exposure Experiment," *Fusion Science and Technology*, pp. 1–7, sep 2017. [Online]. Available: https://www.tandfonline.com/doi/full/10.1080/15361055.2017.1352429 20, 60

[38] J. Rapp, L. W. Owen, X. Bonnin *et al.*, "Transport simulations of linear plasma generators with the B2.5-Eirene and EMC3-Eirene codes," *Journal of Nuclear Materials*, vol. 463, pp. 510–514, aug 2015. [Online]. Available: http://linkinghub.elsevier.com/retrieve/pii/S0022311514010009 20, 58

[39] J. F. Caneses, B. D. Blackwell, and P. Piotrowicz, "Helicon antenna radiation patterns in a high-density hydrogen linear plasma device," *Physics of Plasmas*, vol. 24, no. 11, p. 113513, nov 2017. [Online]. Available: http://aip.scitation.org/doi/10.1063/1.5000848 20

[40] P. A. Piotrowicz, J. F. Caneses, D. L. Green *et al.*, "Helicon normal modes in Proto-MPEX," *Plasma Sources Science and Technology*, 2018. 20

[41] F. F. Chen, *Introduction to plasma physics and controlled fusion*, 3rd ed. Springer, 2016. 22, 24, 27, 72, 74

[42] T. Stix, *Waves in Plasmas*. New York: American Institute of Physics-Press, 1992. 23

[43] S. J. Diem, D. L. Green, R. W. Harvey, and Y. V. Petrov, "An electron Bernstein wave heating scheme for the Proto-MPEX linear device," *Phys. Plasmas*, vol. 25, p. 72124, 2018. [Online]. Available: https://doi.org/10.1063/1.5033334 24

[44] F. McDermott, G. Bekefi, K. Hackett *et al.*, "Observation of the parametric decay instability during electron cyclotron resonance heating on the versator ii tokamak," *The Physics of Fluids*, vol. 25, no. 9, pp. 1488–1490, 1982. 24

[45] H. Laqua, V. Erckmann, H. Hartfuß *et al.*, "Resonant and nonresonant electron cyclotron heating at densities above the plasma cutoff by oxb mode conversion at the w7-as stellarator," *Physical review letters*, vol. 78, no. 18, p. 3467, 1997. 24

[46] T. M. Biewer, T. S. Bigelow, J. F. Caneses *et al.*, "Observations of electron heating during 28 GHz microwave power application in proto-MPEX," *Physics of Plasmas*, vol. 25, no. 2, 2018. 24, 80

[47] N. Hershkowitz, "How langmuir probes work," *Plasma Diagnostics: Discharge Parameters and Chemistry*, vol. 1, p. 113, 2013. 27

[48] A. Boschi and F. Magistrelli, "Effect of a rf, signal on the characteristic of a langmuir probe," *Il Nuovo Cimento (1955-1965)*, vol. 29, no. 2, pp. 487–499, 1963. 27

[49] A. Azooz, Y. Al-Jawaady, and Z. Ali, "Langmuir probe rf plasma compensation using a simulation method," *Computer Physics Communications*, vol. 185, no. 1, pp. 350–356, 2014. 27

[50] M. Tuszewski and J. Tobin, "The accuracy of langmuir probe ion density measurements in low-frequency rf discharges," *Plasma Sources Science and Technology*, vol. 5, no. 4, p. 640, 1996. 27

[51] N. S. J. Braithwaite, N. Benjamin, and J. Allen, "An electrostatic probe technique for rf plasma," *Journal of Physics E: Scientific Instruments*, vol. 20, no. 8, p. 1046, 1987. 27

[52] A. Ohsawa, M. Ohuchi, and T. Kubota, "Improved rf-driven probe method for rf discharge plasma diagnostics," *Measurement Science and Technology*, vol. 2, no. 8, p. 801, 1991. 27

[53] F. F. Chen, "Langmuir probe measurements in the intense rf field of a helicon discharge," *Plasma Sources Science and Technology*, vol. 21, no. 5, p. 055013, 2012. 27

[54] L. Oksuz, F. Soberon, and A. Ellingboe, "Analysis of uncompensated langmuir probe characteristics in radio-frequency discharges revisited," *Journal of applied physics*, vol. 99, no. 1, p. 013304, 2006. 27

[55] J. F. Caneses and B. Blackwell, "Rf compensation of double langmuir probes: modelling and experiment," *Plasma Sources Science and Technology*, vol. 24, no. 3, p. 035024, 2015. 27, 103

[56] R. Castro, G. Cirino, P. Verdonck *et al.*, "A comparative study of single and double langmuir probe techniques for rf plasma characterization," *Contributions to Plasma Physics*, vol. 39, no. 3, pp. 235–246, 1999. 27

[57] J. G. Laframboise, "Theory of spherical and cylindrical langmuir probes in a collisionless, maxwellian plasma at rest," DTIC Document, Tech. Rep., 1966. 28, 31

[58] E. H. Martin, "Electric field measurements of the capacitively coupled magnetized RF sheath utilizing passive optical emission spectroscopy," Ph.D. dissertation, North Carolina State University, 2014. 29

[59] L. Oksuz, F. Soberón, and A. R. Ellingboe, "Analysis of uncompensated Langmuir probe characteristics in radio-frequency discharges revisited," *Journal of Applied Physics*, vol. 99, no. 1, p. 013304, jan 2006. [Online]. Available: http://aip.scitation.org/doi/10.1063/1.2158496 36

[60] J. F. Caneses and B. Blackwell, "RF compensation of double Langmuir probes: modelling and experiment," *Plasma Sources Science and Technology*, vol. 24, no. 3, pp. 1–18, 2015. [Online]. Available: http://stacks.iop.org/0963-0252/24/i=3/a=035024?key=crossref.cdf1ba7047e82f4cc93317890e387b7e 36

[61] K.-S. Chung, "Mach probes," *Plasma Sources Science and Technology*, vol. 21, no. 6, p. 63001, dec 2012. 40, 108

[62] D. Evans and J. Katzenstein, "Laser light scattering in laboratory plasmas," *Reports on Progress in Physics*, vol. 32, no. 1, p. 207, 1969. 43

[63] A. Okamoto, S. Kado, S. Kajita, and S. Tanaka, "Laser Thomson scattering system applicable to low-temperature plasma in the divertor simulator MAP-II," pp. 1–4, 2005. 43

[64] H. J. Van Der Meiden, A. R. Lof, M. A. Van Den Berg *et al.*, "Advanced Thomson scattering system for high-flux linear plasma generator," *Review of Scientific Instruments*, vol. 83, no. 12, p. 123505, dec 2012. [Online]. Available: http://aip.scitation.org/doi/10.1063/1.4768527 43, 46

[65] M. Hubeny, B. Schweer, D. Luggenhölscher *et al.*, "Thomson scattering of plasma turbulence on PSI-2," *Nuclear Materials and Energy*, vol. 12, pp. 1253–1258, 2017. 43

[66] K. Lee, K. Lee, J. Kim, and T. Lho, "High resolution thomson scattering system for steady-state linear plasma sources," *Review of Scientific Instruments*, vol. 89, no. 1, p. 013508, 2018. 43, 51

[67] I. H. Hutchinson, *Principles of plasma diagnostics*, 2nd ed. Cambridge, UK: Cambridge University Press, 2005. 43

[68] T. M. Biewer and G. Shaw, "Initial implementation of a Thomson scattering diagnostic for Proto-MPEX," *Review of Scientific Instruments*, vol. 85, no. 11, p. 11D812, nov 2014. [Online]. Available: http://aip.scitation.org/doi/10.1063/1.4886959 44

[69] T. M. Biewer, S. Meitner, J. Rapp *et al.*, "First results from the Thomson scattering diagnostic on proto-MPEX," *Review of Scientific Instruments*, vol. 87, no. 11, p. 11E518, nov 2016. [Online]. Available: http://www.ncbi.nlm.nih.gov/pubmed/27910678http://aip.scitation.org/doi/10.1063/1.4959163 44, 49

[70] "Beam expanders | edmund optics." [Online]. Available: https://www.edmundoptics.com/resources/application-notes/lasers/beam-expanders/ 46

[71] N. Kafle, T. M. Biewer, and D. C. Donovan, "Dual-pass upgrade to the Thomson scattering diagnostic on the Prototype-Material Plasma Exposure eXperiment (Proto-MPEX)," *Review of Scientific Instruments*, vol. 89, no. 10, p. 10C107, 2018. [Online]. Available: http://aip.scitation.org/doi/10.1063/1.5039370 53

[72] M. Jaworski, N. Chopra, J. Pearcy *et al.*, "An optical offset method for increased dynamic range in schlieren imaging systems." 22nd Topical Conference on High-Temperature Plasma Diagnostics, San Diego, California, USA, 2018. 55

[73] L. W. Owen, J. F. Caneses, J. Canik *et al.*, "B2.5-Eirene modeling of radial transport in the MAGPIE linear plasma device," *Plasma Sources Science and Technology*, vol. 26, no. 5, p. 055005, mar 2017. [Online]. Available: http://stacks.iop.org/0963-0252/26/i=5/a=055005?key=crossref.75d37df7e980e06306cc6fd1179a53b7 58

[74] M. Baeva, W. J. Goedheer, N. J. Lopes Cardozo, and D. Reiter, "B2-EIRENE simulation of plasma and neutrals in MAGNUM-PSI," *Journal of Nuclear Materials*, vol. 363-365, no. 1-3, pp. 330–334, 2007. 58

[75] O. Waldmann, H. Meyer, and G. Fussmann, "Anomalous diffusion in a linear plasma generator," *Contributions to Plasma Physics*, vol. 47, no. 10, pp. 691–702, dec 2007. [Online]. Available: http://doi.wiley.com/10.1002/ctpp.200710079 58

[76] L. W. Owen, J. Rapp, J. Canik, and J. D. Lore, "Transport modeling of convection dominated helicon discharges in Proto-MPEX with the B2.5-Eirene code," *Physics of Plasmas*, vol. 24, no. 11, p. 112504, nov 2017. [Online]. Available: http://aip.scitation.org/doi/10.1063/1.5002534 58, 59, 60

[77] H. Kastelewicz and G. Fussmann, "Plasma modelling for the PSI linear plasma device," *Contributions to Plasma Physics*, vol. 44, no. 4, pp. 352–360, jul 2004. [Online]. Available: http://doi.wiley.com/10.1002/ctpp.200410053 58

[78] R. C. Wieggers, D. P. Coster, P. W. C. Groen *et al.*, "B2.5-Eunomia simulations of Pilot-PSI plasmas," *Journal of Nuclear Materials*, vol. 438, no. SUPPL, pp. S643–S646, 2013. 58

[79] B. J. Braams, "Computational Studies in Tokamak Equilibrium and Transport," Ph.D. dissertation, Rijksuniversiteit Utrecht, Netherlands, 1986. [Online]. Available: https://inis.iaea.org/search/search.aspx?orig{_}q=RN:18038616 58

[80] D. Reiter, "The EIRENE Code User Manual Version," *Julich*, 2016. [Online]. Available: http://www.eirene.de/html/manual.html 58

[81] X. Bonnin, A. S. Kukushkin, and D. P. Coster, "Code development for ITER edge modelling - SOLPS5.1," *Journal of Nuclear Materials*, vol. 390-391, no. 1, pp. 274–277, 2009. 58

[82] R. Schneider, X. Bonnin, K. Borrass *et al.*, "Plasma edge physics with b2-eirene," *Contributions to Plasma Physics*, vol. 46, no. 1-2, pp. 3–191, 2006. 58

[83] M. L. Solomon, I. Mihaila, V. Anita *et al.*, "Measurements of plasma diffusion coefficient in Pilot-PSI device using Katsumata probe," *Journal of Automation Mobile Robotics and Intelligent Systems*, vol. 3, pp. 160–162, 2009. 58

[84] D. D. Blackwell and F. F. Chen, "Two-dimensional imaging of a helicon discharge," *Plasma Sources Science and Technology*, vol. 6, no. 4, p. 569, 1997. 60

[85] J. Caneses, "Helicon wave propagation and plasma equilibrium in high-density hydrogen plasma in converging magnetic fields," Ph.D. Thesis, Australian National University, 2015. 62

[86] J. J. Gosselin, S. C. Thakur, S. H. Sears *et al.*, "Overestimation of Mach number due to probe shadow," *Physics of Plasmas*, vol. 23, no. 7, 2016. 63

[87] R. A. Pitts and P. C. Stangeby, "Experimental tests of Langmuir probe theory for strong magnetic fields," *Plasma Physics and Controlled Fusion*, vol. 32, no. 13, pp. 1237–1248, 1990. 63

[88] B. LaBombard, J. Rice, A. Hubbard *et al.*, "Transport-driven scrape-off layer flows and the x-point dependence of the l-h power threshold in alcator c-mod," *Physics of Plasmas*, vol. 12, no. 5, p. 056111, 2005. 68

[89] B. Lipschultz, X. Bonnin, G. Counsell *et al.*, "Plasma–surface interaction, scrape-off layer and divertor physics: implications for iter," *Nuclear Fusion*, vol. 47, no. 9, p. 1189, 2007. 68

[90] E. Priest, *Magnetohydrodynamics of the Sun*. New York: Cambridge University Press, 2014. 74

[91] J. D. Anderson Jr, *Fundamentals of aerodynamics*. Tata McGraw-Hill Education, 2010. 76

[92] S. I. Braginskii, "Transport processes in a plasma," *Reviews of Plasma Physics*, vol. 1, p. 205, 1965. [Online]. Available: http://adsabs.harvard.edu/abs/1965RvPP....1..205Bhttp://people.hao.ucar.edu/judge/homepage/PHSX515/fall2012/Braginskii1965.pdf 76

[93] A. W. Leonard, G. D. Porter, R. D. Wood *et al.*, "Radiative Divertor Plasmas with Convection in DIII-D," *Physics of Plasmas*, vol. 5, no. 5, 1998. [Online]. Available: https://doi.org/10.1063/1.872842 76

[94] J. Rapp, L. W. Owen, J. Canik *et al.*, "Radial transport modeling of high density deuterium plasmas in proto-MPEX with the B2.5-Eirene code," *Physics of Plasmas*, vol. 26, no. 4, p. 042513, apr 2019. [Online]. Available: https://doi.org/10.1063/1.5049808http://aip.scitation.org/doi/10.1063/1.5049808 79

[95] J. F. Caneses, D. A. Spong, C. Lau *et al.*, "Effect of magnetic field ripple on parallel electron transport during microwave plasma heating in the Proto-MPEX linear plasma device," *Plasma Physics and Controlled Fusion*, in review. 80, 96, 99, 100, 103, 110

[96] D. D. Ryutov, "Open-ended traps Open-ended traps," *Soviet Physics Uspekhi*, vol. 31, no. 4, p. 300, 1988. [Online]. Available: http://iopscience.iop.org/article/10.1070/PU1988v031n04ABEH005747/pdf 95, 99, 109

[97] R. F. Post, "The magnetic mirror approach to fusion," *Nuclear Fusion*, vol. 27, no. 10, p. 1579, 1987. 96

[98] W. Fundamenski and O. Garcia, "Comparison of coulomb collision rates in the plasma physics and magnetically confined fusion literature," EFDA-JET, Tech. Rep., 2007. 96

[99] A. A. Ivanov and V. V. Prikhodko, "Gas-dynamic trap: An overview of the concept and experimental results," p. 31, 2013. [Online]. Available: https://iopscience-iop-org.proxy.lib.utk.edu/article/10.1088/0741-3335/55/6/063001/pdf 99

[100] K. L. Lam, B. J. Leikind, A. Y. Wong *et al.*, "Mirror ratio scaling of axial confinement of a mirror-trapped collisional plasma," *Physics of Fluids*, vol. 29, no. 10, p. 3433, 1986. 99, 102

[101] A. Makhijani, A. J. Lichtenberg, M. A. Lieberman, and B. G. Logan, "Plasma confinement in multiple-mirror systems. I: Theory," *Citation: The Physics of Fluids*, vol. 17, p. 1302, 1974. 99

[102] B. G. Logan, I. G. Brown, A. J. Lichtenberg, and M. A. Lieberman, "Plasma confinement in multiple mirror systems. II. Experiment and reactor calculation," vol. 17, p. 80003, 1974. 99

[103] T. D. Rognlien and T. A. Cutler, "Transition from pastukhov to collisional confinement in a magnetic and electrostatic well," *Nuclear Fusion*, vol. 20, no. 8, pp. 1003–1011, 1980. 100, 102, 107

[104] J. R. Ferron, R. Goulding, B. A. Nelson *et al.*, "Electrostatic end plugging accompanied by a central-cell density increase in an axisymmetric tandem mirror," *Physics of Fluids*, vol. 30, no. 9, pp. 2855–2869, 1987. [Online]. Available: http://aip.scitation.org/toc/pfl/30/9https://aip.scitation.org/doi/10.1063/1.866050 102

[105] M. Inutake, T. Cho, M. Ichimura *et al.*, "Thermal barrier formation and plasma confinement in the axisymmetrized tandem mirror gamma 10," *Physical review letters*, vol. 55, no. 9, p. 939, 1985. 109

[106] M. Showers, T. M. Biewer, J. Caughman *et al.*, "Heat flux estimates of power balance on proto-mpex with ir imaging," *Review of Scientific Instruments*, vol. 87, no. 11, p. 11D412, 2016. 110

Appendices

Appendix A

Thomson Scattering calibrations

This appendix presents calibrations of the spectrometer to obtain electron temperature and Rayleigh scattering density using known neutral N_2 atoms for the Thomson scattering diagnostic.

A Spectrometer pixel number to wavelength calibration

Neon light is used for calibration of the wavelength from the Princeton Instrument's PI-MAX-3 camera. The calibration factors are obtained using Eq. (A.1),

$$\lambda_p = \lambda_{\text{offset}} + d_1 p + d_2 p^2 \tag{A.1}$$

where λ_p is the rest wavelength of pixel p, λ_{offset} is the offset in the wavelength, and d_1(nm/pixel) and d_2(nm/pixel^2) are dispersion. A linear fit to the peak values of the spectrum shown in Fig. A.1 gives the pixel to wavelength calibration. Known rest length wavelengths of Ne for the calibration are 5330.77 Å and 5341.09 Å, which are used to obtain the dispersion and offset in the wavelength.

B Density calculation

The Rayleigh scattering (RS) calibration along with the ideal gas law is utilized to calculate the electron density from the Thomson scattering (TS) diagnostics. The measured number of counts (M_{counts}) is equal to the number of photons ($n_{photons}$), the scattering cross section σ and the number density (n)of the scattering object, as shown in Eq. (A.2)

$$M_{\text{counts}} = n_{\text{photons}} \cdot \sigma \cdot n \tag{A.2}$$

The number of photons is proportional to the laser energy (E_{laser}); therefore modifying Eq. (A.2) for RS and TS, which gives Eqs. (A.3) and (A.4).

$$M_{\mathrm{RS}} \propto E_{\mathrm{laser}} \cdot \sigma_{\mathrm{RS}} \cdot n_{N_2} \tag{A.3}$$

$$M_{\mathrm{TS}} \propto E_{\mathrm{laser}} \cdot \sigma_{\mathrm{TS}} \cdot n_e \tag{A.4}$$

where n_{N_2} and n_e are the number density of the nitrogen gas and electrons. From the ideal gas law, it is known that

$$\frac{\mathrm{n}}{\mathrm{V}} = \frac{\mathrm{P}}{\mathrm{RT}} \tag{A.5}$$

where P is the neutral pressure of nitrogen gas back filled in the vacuum chamber, R is the gas constant, which is 8.31 J/(mol-K), and T is the room temperature typically 300 K. Using Eqs. (A.5) and (A.3), the measured number of counts from the Rayleigh scattering calibration can be related to the nitrogen pressure and the laser energy.

$$\mathrm{M_{RS}} \propto \mathrm{E_{laser}} \cdot \sigma_{\mathrm{RS}} \cdot \frac{\mathrm{P}}{\mathrm{RT}} \tag{A.6}$$

Taking the ratio of Eq. (A.6) and Eq. (A.4) one gets

$$\frac{M_{RS}}{M_{\mathrm{TS}}} = \frac{E_{\mathrm{laser}} \cdot \sigma_{RS} \cdot P_{N_2}/\mathrm{RT}}{E_{\mathrm{laser}} \cdot \sigma_{TS} \cdot n_e} \tag{A.7}$$

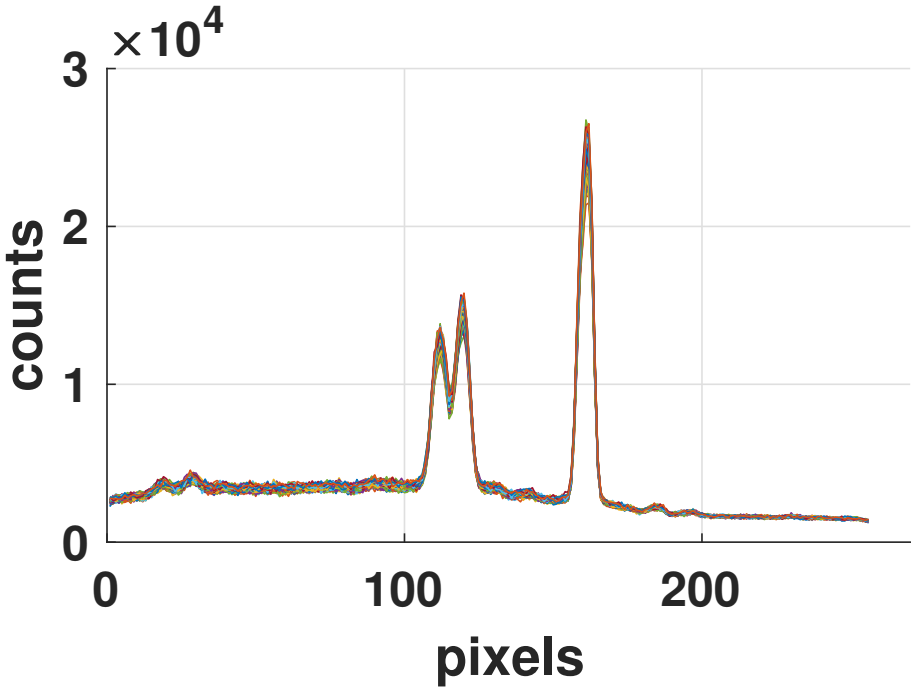

Figure A.1: Spectral lines from the neon lamp.

Rearranging,

$$n_e = \frac{M_{\mathrm{TS}}}{M_{\mathrm{RS}}} \cdot \frac{\sigma_{\mathrm{RS}}}{\sigma_{\mathrm{TS}}} \cdot \frac{P_{\mathrm{N_2}}}{\mathrm{RT}} \tag{A.8}$$

The ratio of the scattering cross-section between the Rayleigh scattering and the Thomson scattering $\left(\frac{\sigma_{RS}}{\sigma_{TS}}\right)$ is 1/380.

Appendix B

Error Propagation

A generalized error propagation formula with independent variables for measured quantities is given by,

$$s_f = \sqrt{\left(\frac{\partial f}{\partial x_1}\right)^2 s_1^2 + \left(\frac{\partial f}{\partial x_2}\right)^2 s_2^2 + \left(\frac{\partial f}{\partial x_3}\right)^2 s_3^2 + \ldots} \tag{B.1}$$

where, s_f is the standard deviation in the function f, and $s_1 \ldots s_3$ are standard deviation in measured quantities $1 \ldots 3$.

Appendix C

Additional probe information

A Alternative method to calculate electron temperature from the IV characteristics from DLP

Double probe has two conditions to satisfy:

i) $i_1 + i_2 = 0$

ii) $V = V_1 - V_2$

Current on probe tip 1: $i_1 = i_{1e} - i_{1i}$
Current on probe tip 2: $i_2 = i_{2e} - i_{2i}$

$$\begin{aligned} i_e &= en_e A\left(\frac{kT_e}{2\pi m_e}\right)^{0.5} \exp\left[\frac{-e(\phi_p - V)}{kT_e}\right] \\ i_i &= en_e A\left(\frac{Z_i kT_e}{2\pi m_i}\right)^{0.5} \chi_i \left[\frac{e(\phi_p - V)}{kT_e}\right]^{\eta_i} \end{aligned} \tag{C.1}$$

Therefore, probe current 1 is:

$$i = i_1 = en_e A\left(\frac{kT_e}{2\pi}\right)^{0.5}\left[\left(\frac{1}{m_e}\right)^{0.5} \exp\frac{-e(\phi_p - V)}{kT_e} - \left(\frac{Z_i}{m_i}\right)^{0.5} \chi_i \left[\frac{-e(\phi_p - V)}{kT_e}\right]^{\eta_i}\right] \tag{C.2}$$

Let,

$$V^\star = V_1 - \phi_p$$
$$\implies \phi_p - V_1 = -V^\star$$

using condition (ii): $V_2 - \phi_p = V_1 - \phi_p - V \implies V_2 - \phi_p = V^\star - V$

$$\implies \phi_p - V_2 = V - V^\star$$

From the above conditions the probe tips currents are shown below in Eqs. (C.3-C.4):

$$i_1 = en_e\left(\frac{kT_e}{2\pi}\right)^{0.5}\left[A_{1e}\left(\frac{1}{m_e}\right)^{0.5}\exp\frac{-e(-V^\star)}{kT_e} - A_{1i}\left(\frac{Z_i}{m_i}\right)^{0.5}\chi_i\left[\frac{e(-V^\star)}{kT_e}\right]^{\eta_i}\right] \tag{C.3}$$

$$i_2 = en_e\left(\frac{kT_e}{2\pi}\right)^{0.5}\left[A_{2e}\left(\frac{1}{m_e}\right)^{0.5}\exp\frac{-e(V-V^\star)}{kT_e} - A_{2i}\left(\frac{Z_i}{m_i}\right)^{0.5}\chi_i\left[\frac{e(V-V^\star)}{kT_e}\right]^{\eta_i}\right] \tag{C.4}$$

Solve for $V^\star$ using condition (i) in $i_1 + i_2 = 0$. This is a transcendental equation that can be solved numerically.

B Mach Probe circuit diagram

A circuit design to drive the Mach probes tips is shown in Fig. C.1. Voltage is applied to the both tips simultaneously; however, the longer tips are vulnerable to damage if operated for the duration of the discharge. In order to minimize the current being drawn by Tip 1 and Tip 1 a relay switch gates the probe with 4-10% duty cycle. The BNC connection from the probe has the same machine ground as Proto-MPEX.

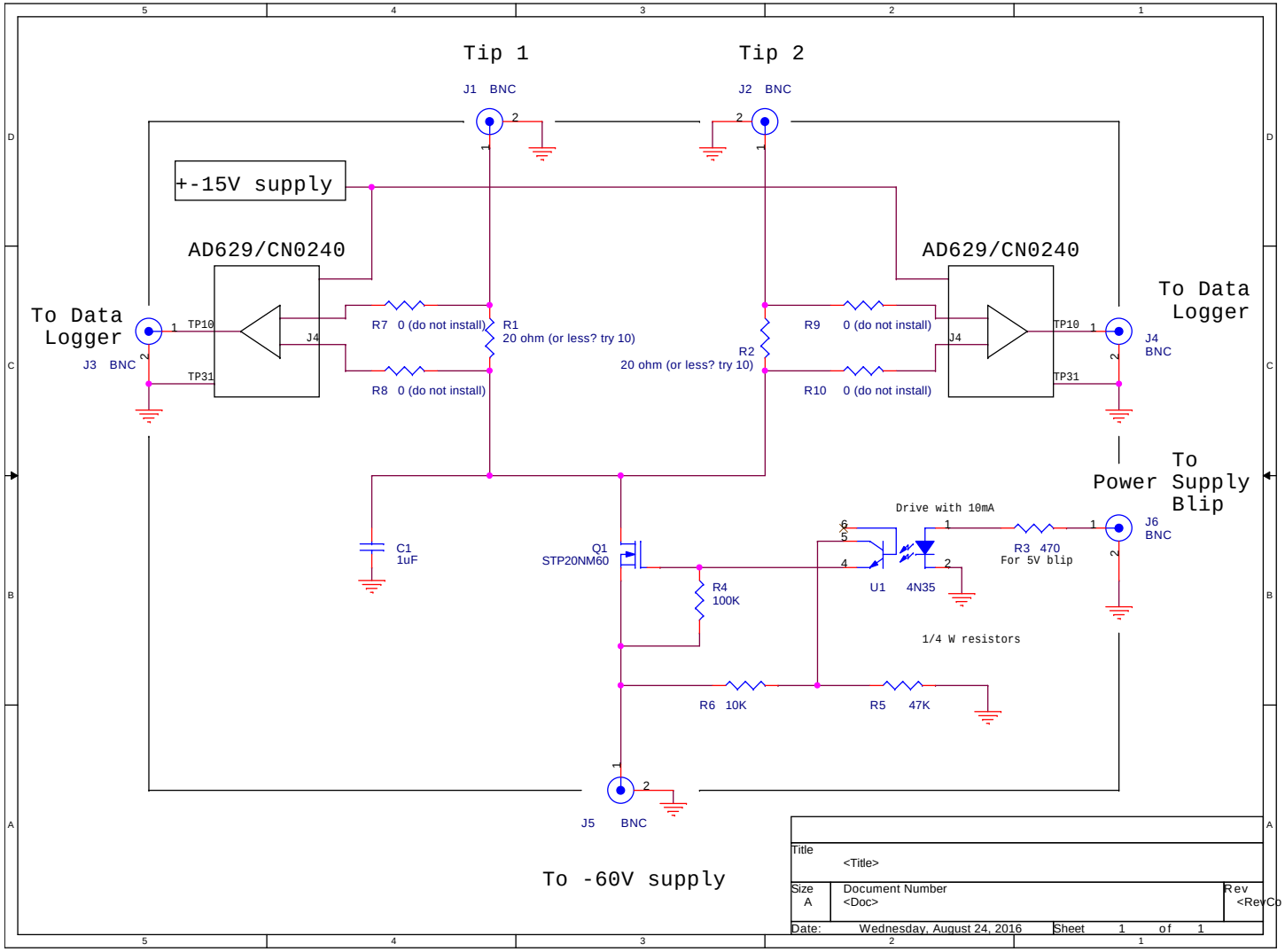

Figure C.1: The Mach probe driver circuit built for Proto-MPEX to provide DC power to the Mach probe tips and measure the saturation current. Commercial off the self components were used in the circuit.

Appendix D

Additional plots

A Flow measurement with ICH

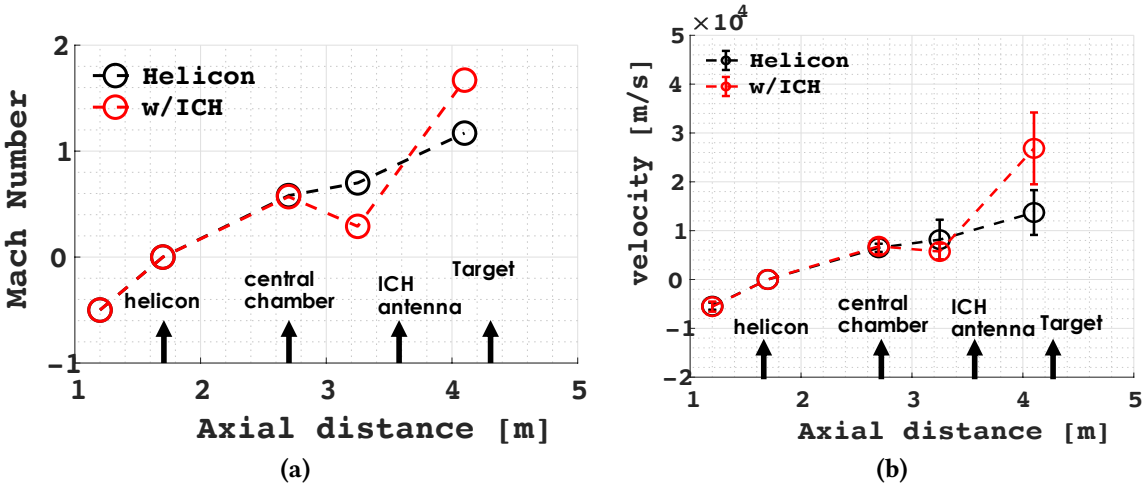

Figure D.1: On-axis axial (a) Mach number and (b) velocity profile is shown for helicon with ICH operation.

B Double Langmuir probe radial profiles

B.1 Downhill magnetic field

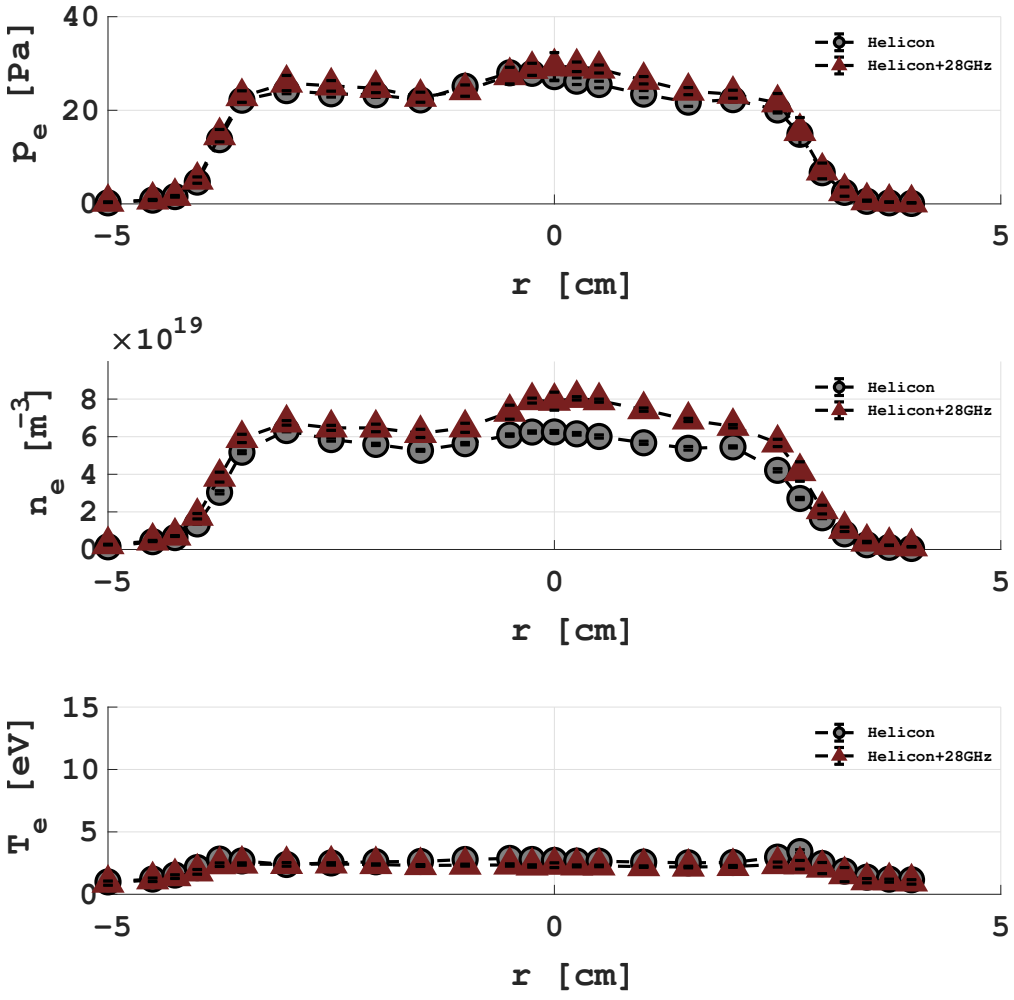

Figure D.2: p_e, n_e, and T_e at spool 1.5

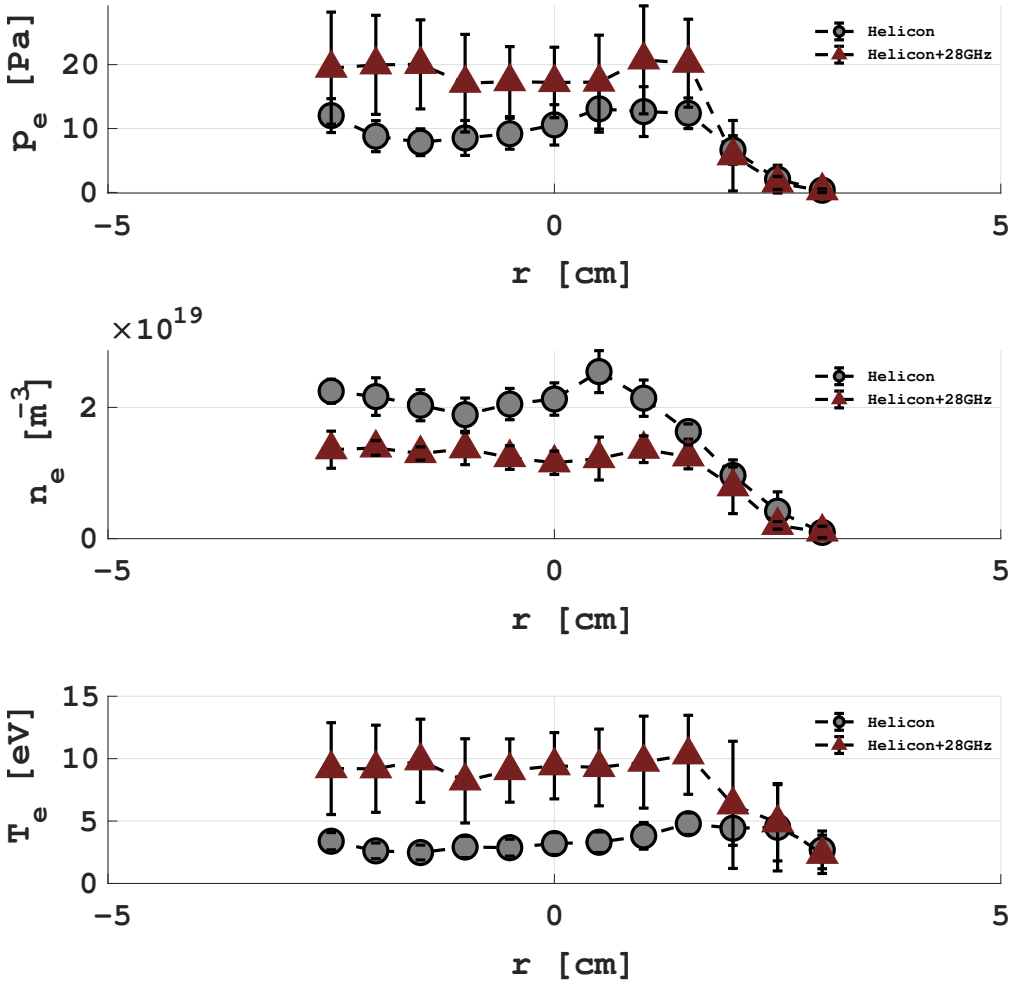

Figure D.3: p_e, n_e, and T_e at spool 8.5

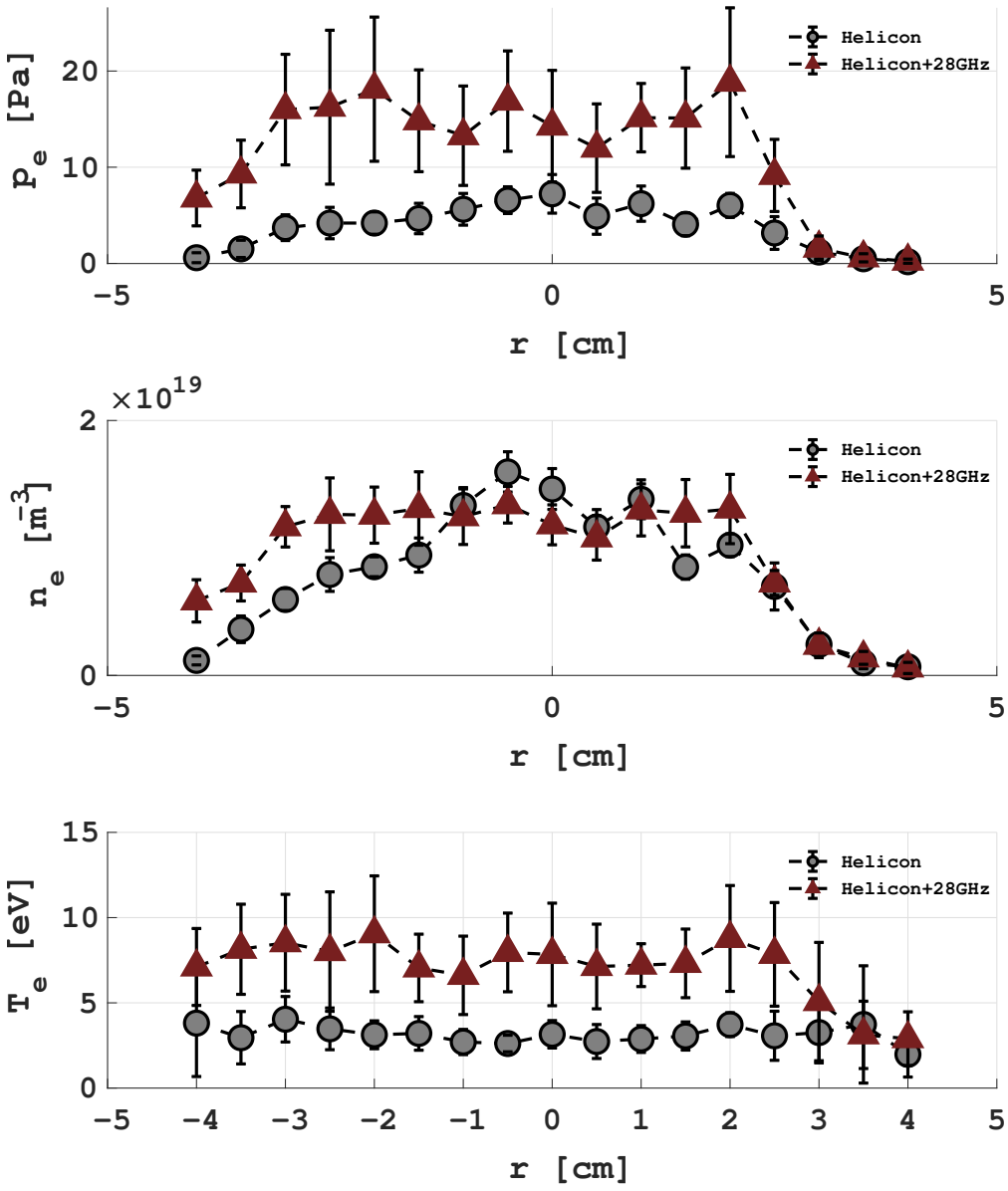

Figure D.4: p_e, n_e, and T_e at spool 12.5

B.2 Overhill magnetic field

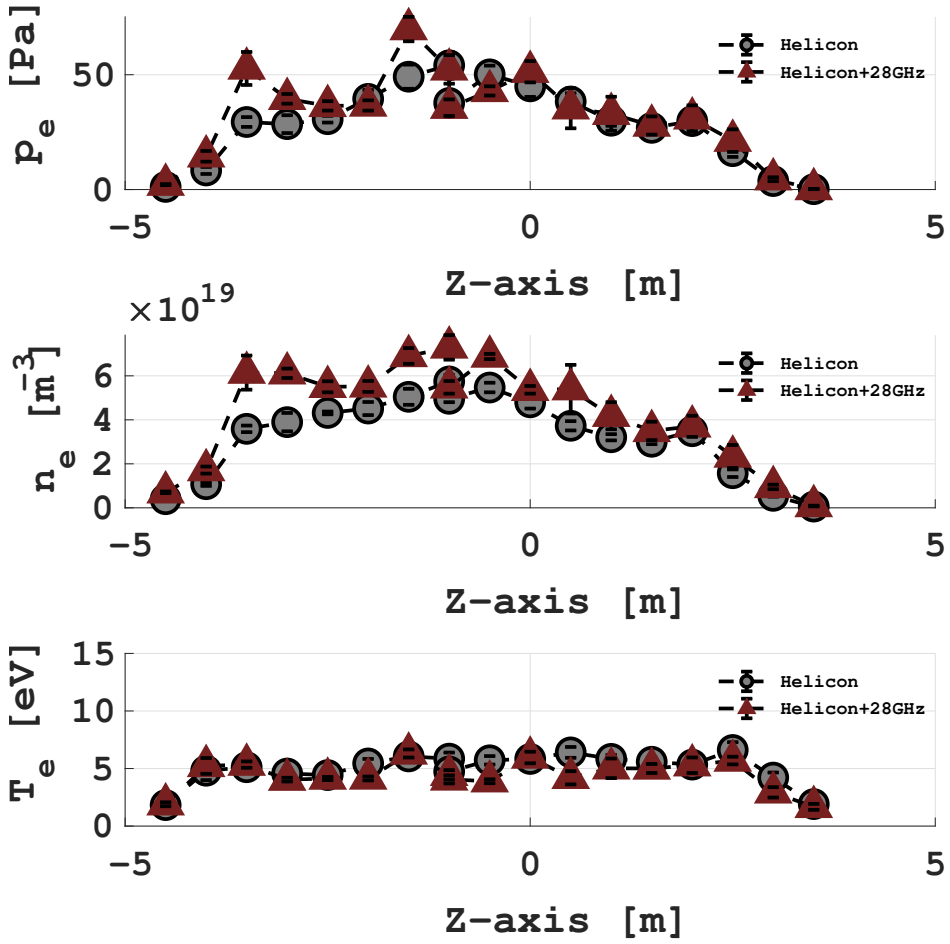

Figure D.5: p_e, n_e, and T_e at spool 1.5

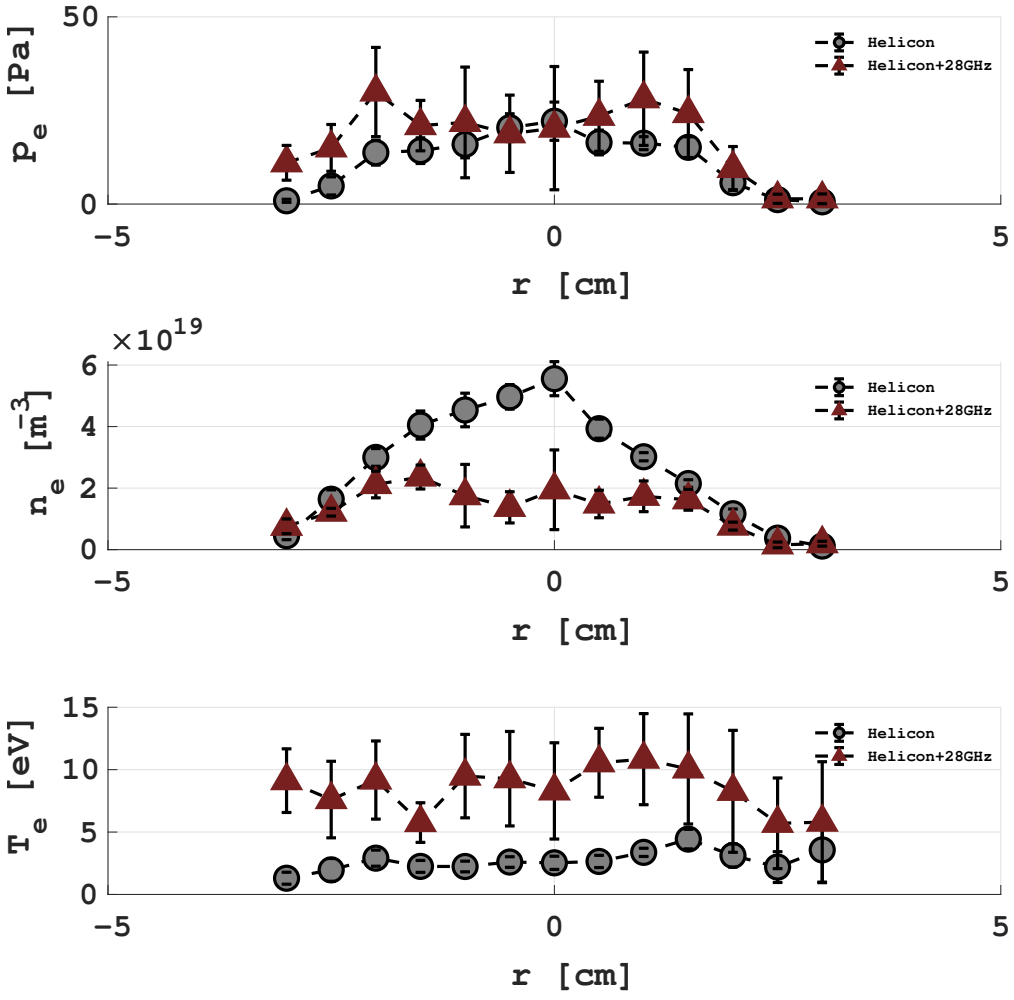

Figure D.6: p_e, n_e, and T_e at spool 8.5

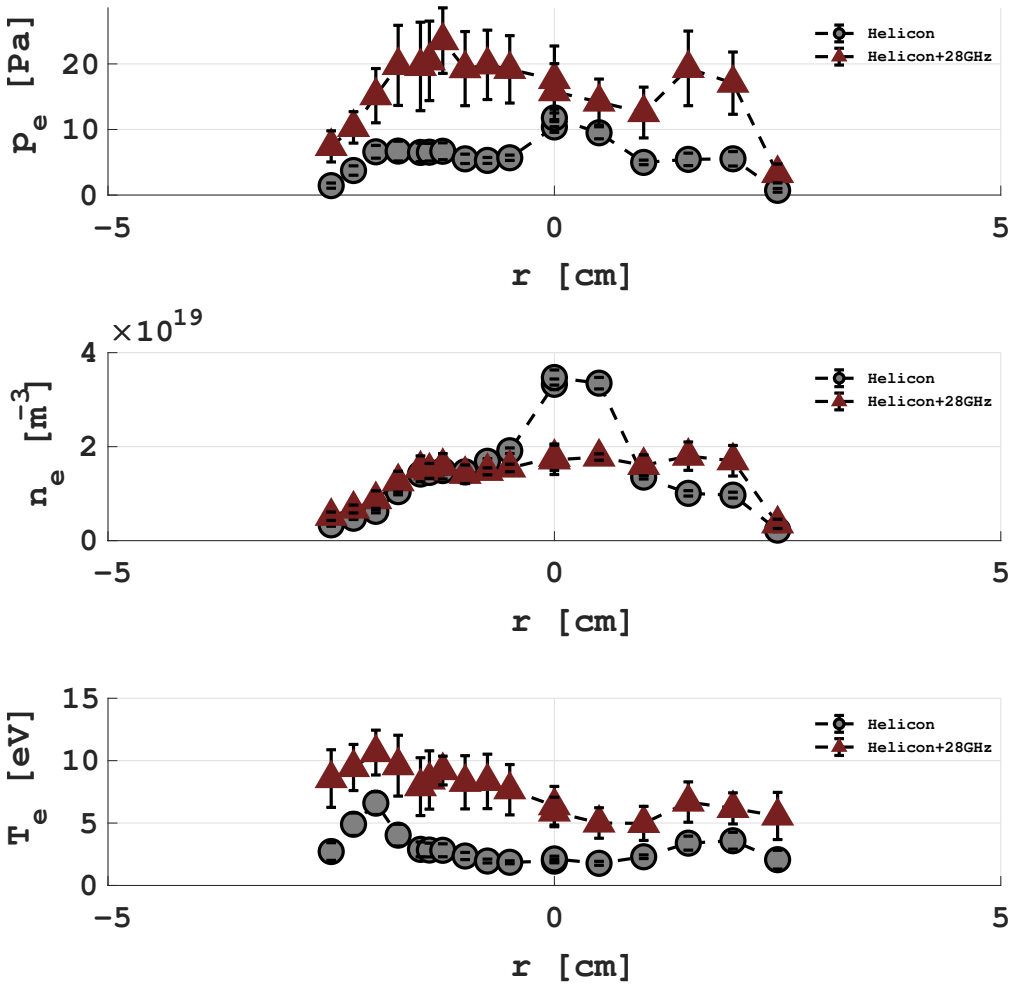

Figure D.7: p_e, n_e, and T_e at spool 12.5

Vita

Nischal Kafle was born to Neeta and Navaraj Kafle in Kathmandu, the capital city of the Himalayan nation, Nepal. While growing up, he was fond of cricket and did not missed an opportunity to play with his cousins or friends. After completing his high school in his home town, Nischal came to the United States to pursue his higher education. He completed his undergraduate degree in 2011 and masters degree in 2014 from Texas A&M University–College Station. Nischal started his graduate school to pursue his Ph.D. degree at The University of Tennessee–Knoxville in 2014. After graduation, he plans on continuing his research on experimental plasma physics. He also intends on enjoying life and acquiring experiences while traveling the world with his wife, Shikha.